



HAL
open science

Experiments and models until failure of bonded joints for crashworthiness

David Morin

► **To cite this version:**

David Morin. Experiments and models until failure of bonded joints for crashworthiness. Engineering Sciences [physics]. Université de Valenciennes et du Hainaut-Cambrésis, 2010. English. NNT : 2010VALE0026 . tel-03009020

HAL Id: tel-03009020

<https://uphf.hal.science/tel-03009020>

Submitted on 17 Nov 2020

HAL is a multi-disciplinary open access archive for the deposit and dissemination of scientific research documents, whether they are published or not. The documents may come from teaching and research institutions in France or abroad, or from public or private research centers.

L'archive ouverte pluridisciplinaire **HAL**, est destinée au dépôt et à la diffusion de documents scientifiques de niveau recherche, publiés ou non, émanant des établissements d'enseignement et de recherche français ou étrangers, des laboratoires publics ou privés.

2010 V A L E 0026



THÈSE

Pour l'obtention du grade de

Docteur de l'Université de Valenciennes et du Hainaut-Cambrésis

Ecole Doctorale régionale Sciences Pour l'ingénieur Lille Nord-de-France

DISCIPLINE: GENIE MECANIQUE

Présentée par

David MORIN

Experiments and models until failure of bonded joints for crashworthiness

Soutenance prévue le 10 Septembre 2010

Jury :

<i>Rapporteurs :</i>	Ahmed BENALLAL	Directeur de Recherche	- CNRS/LMT Cachan
	Arild Holm CLAUSEN	Professeur	- NTNU Norvège
<i>Directeur de thèse :</i>	Franck LAURO	Professeur	- Université de Valenciennes
<i>Examineurs :</i>	Bruno BENNANI	Maitre de conférences	- Université de Valenciennes
	Gregory HAUGOU	Maitre de conférences	- Université de Valenciennes
	Moussa NAÏT ABDELAZIZ	Professeur	- Université de Lille
	Nadia BAHLOULI	Maitre de conférences	- Université de Strasbourg
	Othman RAMZI	Maitre de conférences	- École Centrale de Nantes
<i>Invités :</i>	Benjamin BOUREL	Ingénieur Recherche	- Université de Valenciennes
	Joelle RICHARD	Ingénieur	- ARCELORMITTAL
	Laurent COTINAUT	Ingénieur	- ARCELORMITTAL
	Colmar WOCKE	Ingénieur	- DOW AUTOMOTIVE

ck LAURO and Mr Bruno BENNANI for their support and supervision during my master and thesis works. Thank you for your listening and pertinent judgement about my questions and ideas.

I would like also to acknowledge ARCELORMITTAL through the persons of Ms Joëlle RICHARD, Mr Laurent COTINAUT and Mr Nicolas BAILLY. Thank you again for the knowledge of you have brought to me during these works. The technical team of ARCELORMITTAL Montataire through the people of Jean-Michel, Michel and Christine are also acknowledge for the help and time they have spend with me during my short visits.

Another acknowledgment goes to DOW AUTOMOTIVE and especially Mr Colmar WOCKE which have given the adhesive of this thesis and some useful informations on the modeling of adhesive.

A special acknowledgment is dedicated to Mr Gregory HAUGOU and Mr Benjamin BOUREL for their help in the experimental and numerical parts of my thesis. I hope that we will able to achieve a lot of tests together Gregory and for you Benjamin a lot of finite elements models.

I am grateful for the members of the jury who have accepted to examine and review my works.

I would like to acknowledge all the LAMIH laboratory members, Denis LESUEUR, Rémi DELILLE, Fahmi CHAARI, and many others that I can't give the names here, for their help and happiness during these years in Valenciennes. Thank you also for the other PhD students who have greatly helped me through our scientific or not scientific discussions, Cédric , Romain, Fabrice, Julien H, Julien B, Damien and all the others.

Of course I acknowledge my parents for their support and the possibility they have given to me to realize these long studies. I will never acknowledge you enough.

I would to say thank you and many others things that I can't write here to my wife Marie and my daughter Léonie, I hope that our future will be also exciting that these 7 years together.....

To conclude these acknowledgements I can't forget the society with which everything is possible The Coca-Cola Company thank you for the sugar and the caffen you have brought to me through these years.....

The Coca-Cola logo, featuring the brand name in its signature red script font with a white outline.

Contents

1	Introduction	1
2	Experimentation and characterization of bulk adhesive	9
2.1	Literature study and proposed approach	10
2.2	Experimental campaigns description	13
2.2.1	Bulk adhesive specimen preparation	13
2.2.2	Presentation of loading devices	15
2.2.3	Presentation of specimen geometries	17
2.2.4	Presentation of measurement techniques	19
2.2.5	Description of behaviour law computations	20
2.2.6	Description of failure strain computation	23
2.3	Experimental results	26
2.3.1	Elasticity	26
2.3.2	Plasticity	29
2.3.3	Failure	36
2.4	Behaviour and failure models identifications	39
2.4.1	Visco-elasticity model	39
2.4.2	Visco-plasticity model	40
2.4.3	Volume variation and damage model	41
2.4.4	Failure model	44
2.5	Conclusions	49
2.6	Models parameters summary	50
3	Mesoscopic material behaviour model	51
3.1	Literature study and proposed models	52
3.2	General description of the material behaviour model	56
3.3	Description of elastic prediction	57
3.3.1	Strain rate computation	57
3.3.2	Total strains and volumic strain computation	58
3.3.3	Damaged-viscous elastic prediction	58
3.3.4	Time step consideration	59
3.4	Yield criterion	59
3.4.1	Definition of the yield criterion formulation	60
3.4.2	Selection of yield criterion	60
3.5	Yield return algorithm	60
3.5.1	General overview of associative and non-associative plasticity	61
3.5.2	Description of the plastic potential and the yield return vectors used for the tensile loadings	61
3.5.3	Description of the yield return for the shear and compressive loadings	63
3.5.4	Description of Newton-Raphson algorithm	64
3.6	Results update	66

3.7	Summary of the mesoscopic behaviour model implementation	67
3.8	Conclusions	68
4	Macroscopic finite element model	71
4.1	Literature study and proposed models	72
4.2	User-element implementation	77
4.2.1	General description of finite element implementation	77
4.2.2	Mass matrix computation	78
4.2.3	Local covariant basis computation	78
4.2.4	Opening and sliding displacements description	79
4.2.5	Strains and strain rates computations	80
4.2.6	Stresses computations	80
4.2.7	Nodal forces update	81
4.2.8	Element elimination	82
4.3	Crack propagation through a mesh	86
4.4	Properties identification	87
4.4.1	Work guidelines	87
4.4.2	Behaviour properties	88
4.4.3	Failure properties	90
4.5	Conclusions	100
4.6	Models parameters summary	101
5	Modeling of bonded structures	103
5.1	Presentation of the different structures	104
5.2	Prerequisite to the finite element modeling of bonded structures	105
5.2.1	Mesh size and link between steel and adhesive	105
5.2.2	Steel material properties	106
5.2.3	Failure criterion of adhesive in mesoscopic model	107
5.3	High strain rate double U test	108
5.3.1	Description of experiments	108
5.3.2	Description of numerical simulations	108
5.3.3	Correlation between numerical and experimental results	109
5.4	Dynamic flexure test	111
5.4.1	Description of experiments	111
5.4.2	Description of numerical simulations	112
5.4.3	Correlation between numerical and experimental results	113
5.5	Dynamic axial crushing test	117
5.5.1	Description of experiments	117
5.5.2	Description of numerical simulations	118
5.5.3	Correlation between numerical and experimental results	119
5.6	Proposition of modeling strategy	125
6	Conclusions & perspectives	129
	Bibliography	135

CHAPTER 1

Introduction

Bonding and precisely structural bonding is an assembling technique used by Man since the rise of time. Structural has been used in various sectors during this time with for example the used of natural adhesives for the weapon of prehistoric men. With the emergence of transportation industries in the XXth century, structural bonding has known a growing interest from both industrial and research actors. Indeed with the current goals of safe and lightweight vehicles of the politics and the transportation industry, structural bonding is in fact at the rise of its use.

In the particular context of automotive industry, the use of structural bonding increases each year as shown in Figure 1.1. Between each current and old or comparison models presented in Figure 1.1 the lengths of bonded joints are always increased of more 100%. In addition to these car models, structural bonding is also present with more than 100 meters in some luxurious models like Mercedes class S, BMW 7, Lotus ellipse and so on.

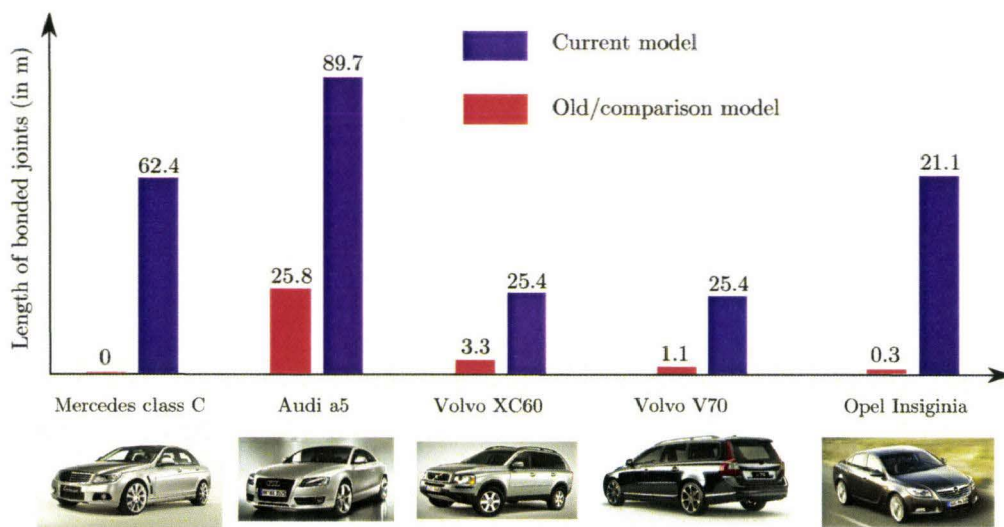


Figure 1.1: evolution of structural bonding use in some car models

The question we can ask now is:

" Why structural bonding is so interesting for automotive industry ? "

Of course the classical advantages of bonding are of interest like the possibility to join dissimilar materials (like polymer on metals...) and the stress concentration reduction in classical assemblies like spot-welding, riveting or climbing but new advantages have appeared with the new generation adhesive.

Now structural bonding is used to improve the durability by overcoming fatigue problems and improving long term durability. The acoustic of car structures is also improved by increasing the stiffness of car body with for example (Table 1.1) between the old and current model of Audi A6 in which an increase of $\approx 240\%$ of the length of the bonded joints is present.

	Increase (in %)
Bending stiffness	34
Torsionnal stiffness	20

Table 1.1: increase of acoustic between the old and new Audi A6

The last domains in which structural bonding is used is the safety and the cost reduction of car structures production. Indeed the safety is improved by enabling the use of Advanced High Strength Steel (AHSS) and increasing the energy management capabilities of car body. The cost reduction is enabled by giving the possibility to reduce the number of spotwelds of a car body for an equivalent safety level.

Therefore this thesis is focused on the following aspects:

- the safety with the increase of energy management capabilities of car structures,
- the cost reduction with the reduction of number of spotwelds,

they have been validated on dynamic axial crushing tests of crashboxes (16 m.s^{-1}) although these arguments are widely used by adhesive producers.

These tests have been performed at ARCELORMITTAL Maizières-les-Metz, the full description of the experimental set up will be given in Chapter 5. Three kinds of crashbox configurations have been analysed (Figure 1.2) to study the effect of structural bonding on the safety and cost reduction. The steel grades and thicknesses are summarized in Figure 1.2.

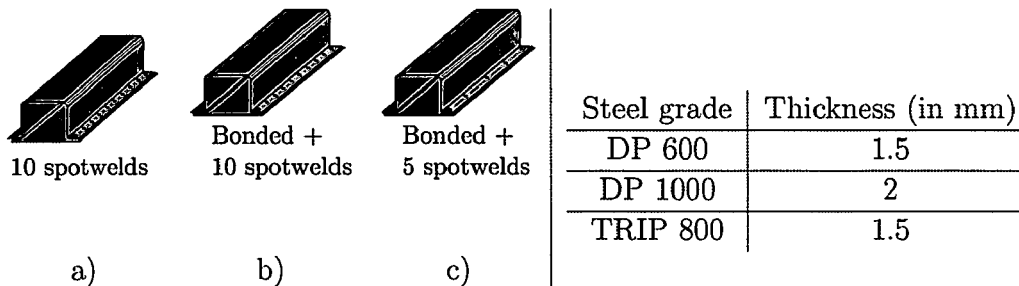


Figure 1.2: crashbox configurations a) 10 spotwelds, b) 10 spotweld + bonding and c) 5 spotwelds + bonding and thicknesses for the corresponding steel grade.

As shown in Figure 1.3, for all the steel grades an increase in the dissipated energy is observed between the 10 spotwelds and the 10 spotwelds + bonding specimens (at least 7% for the DP1000 and a maxima of 14 % for the DP600). It could be notice too that the same dissipated energy is observed between the 10 spotwelds and 5 spotwelds + bonding specimens for all the steel grades. These observations confirm the commercial arguments of the adhesive producers and justify the interest of this thesis.

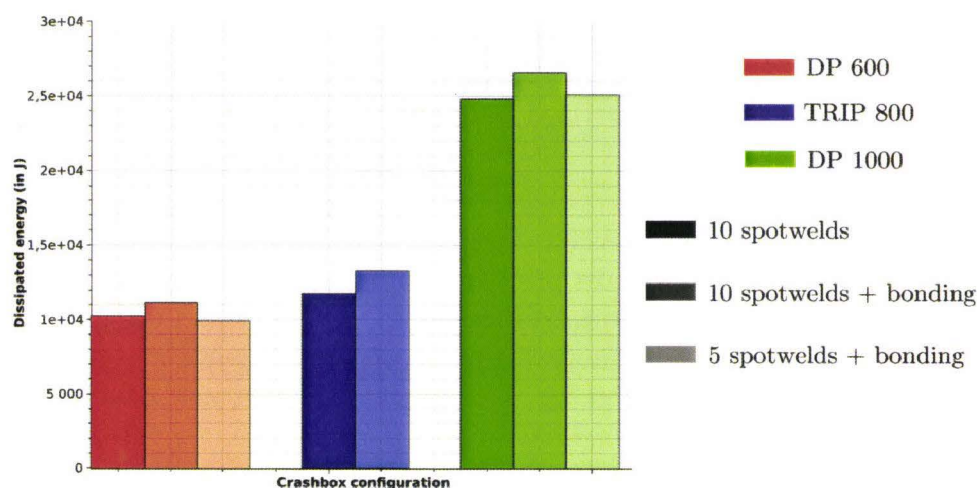


Figure 1.3: evolution of dissipated energy in function of the crashbox configuration.

For all these applications of structural bonding in automotive structures (Figure 1.4) different adhesive are produced by chemical industries:

- anaerobics,
- epoxies,
- reactive acrylics,
- polyurethanes,
- special formulation of cyanoacrylates.

Even if structural bonding has appeared in automotive design a few years ago, its use is only limited to luxurious models (more than 100 m in a Mercedes class S in face of less than 10 m in a Renault Laguna). This limit is mainly due to the the misknowledge of the behaviour of the adhesive in details. Then the bonded joints are not taken into account in the finite element simulations of the automotive structures. The result of this limitation is that the bonded joints are used for the moment only to increase the classical security factor used in mechanical design. Even if the cost of bonding is lower than the cost of the spotwelding technique, its use is limited to luxurious cars. So the next step to obtain an optimal use of structural bonding and its implementation in all kinds of cars is to realize finite element simulations and optimization.

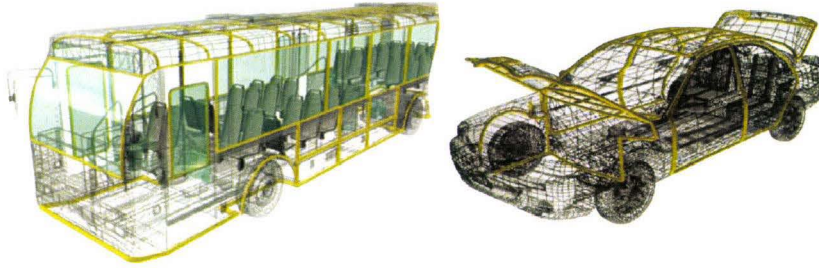


Figure 1.4: possible places of structural bonding in transportation structures (yellow lines).

So as to present the current scientific lockings due to the finite element modeling of bonded structures we have to take place in the particular context of this thesis, the crashworthiness properties of structural adhesives.

The first limit in the modeling of crashworthiness of bonded joints is due to the special purpose adhesive developed for this kinds of applications. A new generation adhesive has been developed by chemical industries and is defined as a crash-stable adhesive. This adhesive is based on an epoxy matrix (Figure 1.5) which toughened by addition of polymer nodules (Figure 1.6 a). In this epoxy matrix some minerals compounds are also added (Figure 1.6 b) so as to optimize the reticulation process of this kind of adhesive.

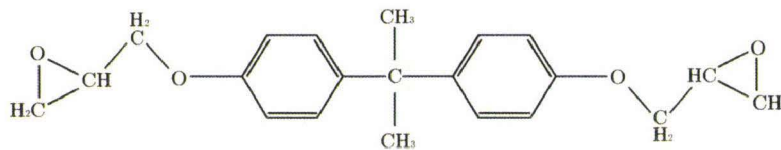


Figure 1.5: formulation of DGEBA epoxyde used in crash-stable adhesives.

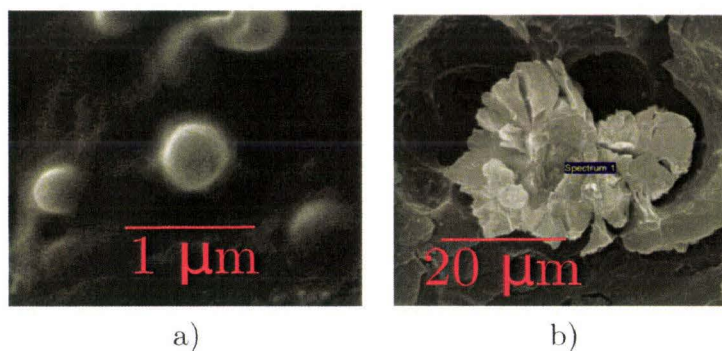


Figure 1.6: a) polymer nodules and b) mineral compounds.

The addition of polymer nodules confers to the classical epoxy matrix which has a brittle behaviour, mechanical properties which are near those of polymer materials:

- visco-elasticity,

- yield difference in tension and compression,
- damage evolution during plasticity,
- visco-plasticity.

These properties are very difficult to identify on classical tests which are widely used in the literature [1] [2] [3] [4] [5]. These tests suffer of a high stress heterogeneity inside the bonded joint but it is also difficult to determine the failure initiation and the combination of stresses and strains which are leading to. All these aspects of experimental characterization will be developed in Chapter 2. From a numerical point of view these mechanical properties suffer of a lack of models in the literature. The most advance has been realized in the works of Dean et al [6] in which a damaged approach is used. More details on these theoretical works will be given in Chapter 3.

The other limit to the modeling of bonded joints is due to the calculation time of finite element simulations. Indeed the finite element softwares used for crashworthiness computations are based on explicit integration scheme. In this scheme, the time step used for the computation is based on the time needed by an elastic wave to cross the smallest element. This time can be computed with the Friedrichs and Levy criterion:

$$\Delta t = l \cdot \sqrt{\frac{\rho}{E}} \quad (1.1)$$

where l is the shortest length of the considered element, ρ its volumic mass and E its elasticity modulus. An illustration of the time step computation for a defined mesh is illustrated in Figure 1.7 and in Table 1.2. The time step of the adhesive volumic elements is always lower than the time step of steel shells, the only possibility to obtain the same time step in both elements is to use a mesh of 1 mm for the steel and only one element through the thickness of the bonded joints (typically 0.3 mm). This solution is unusable due to two reasons, firstly a shell mesh of 1 mm for crashworthiness is non-realistic with current computers and a description of the bonded joint with only one element through the thickness will not give accurate results.

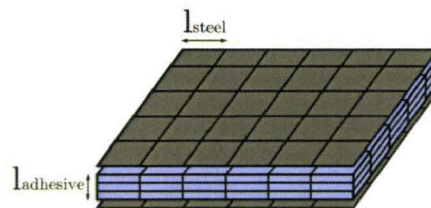


Figure 1.7: illustration of element sizes.

ρ_{steel}	=	$7800Kg/m^3$	l Steel (in mm)	5	3	1
E_{steel}	=	$2.1e^{11}Pa$	time step	$1 \mu s$	$0.6 \mu s$	$0.2 \mu s$
$\rho_{adhesive}$	=	$1180Kg/m^3$	l Adhesive (in mm)	0.3	0.1	0.03
$E_{adhesive}$	=	$2e^9 Pa$	time step	$0.2 \mu s$	$0.07 \mu s$	$0.02 \mu s$

Table 1.2: illustration of time step problem between steel shell and adhesive volume.

Some techniques are already used in industry and litterature to solve the problem of the computation time. From an industrial point of view, mass scaling technique can be used to artificially increase the volumic mass and the resulting time step but this approach underestimate stress and could lead to false prediction of damage and failure of the bonded joints. The other point of view would lead to use interface elements to skip the problem of the time step, this approach is widely used in literature for various problems and will be extended in Chapter 4.

Unfortunately a fine description of the behaviour and failure of the bonded joints and a small computation time can not be solved with the same model. So in this thesis, instead of a unique model, a modeling strategy of bonded joints is then developped. This strategy is based on two models as summarized in Table 1.3. The first one which is called *mesoscopic model* is based on fine behaviour and failure models which are able to represent all the specificities of the adhesive mechanical behaviour. This model is used with many elements in the thickness of the bonded joints but need a small time step and the resulting huge computation time. The second approach is called *macroscopic model* and is based on an interface element which has no effect on the time step computation. Unless this model is not time consuming its representation of the behaviour and failure of the adhesive is simplified.

Model	Mesoscopic	Macroscopic
Advantages	fine description of properties	no effect on the time step
Disadvantages	small time step	simplified description of properties

Table 1.3: summarize of the different models.

Then the proposed modeling strategy is illustrated in Figure 1.8. In the particular context of crashbox design, the different available shapes can be firstly analysed with the macroscopic approach so as to selected the best one and secondly a fine analysis is needed with the mesoscopic approach before finally validate the selected shape with experiments.

Then these thesis works are divided into five main parts. The first one (called here Chapter 2) deals with the experimental campaign on bulk adhesive specimens which have been chosen for the homogenous stress fields and easy analysis. The second part (called here Chapter 3) deals with the implementation of the mesoscopic approach into ABAQUS explicit through a user-material subroutine. The third part (called here Chapter 4) is devoted to the development of the macroscopic approach and its implementation in to ABAQUS explicit through a user-element subroutine. Finally the fourth part (called here

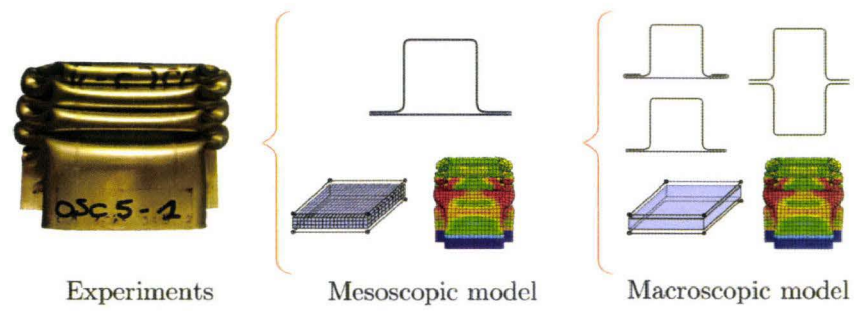


Figure 1.8: representation of the proposed modeling strategy.

Chapter 5) of this thesis is devoted to the validation of the two approaches on different complex load tests.

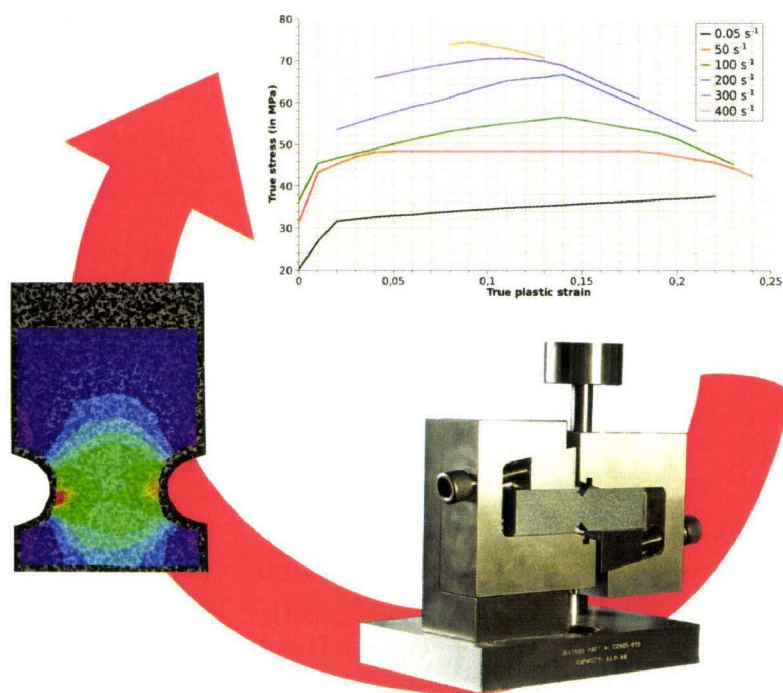
Experimentation and characterization of bulk adhesive

Contents

2.1	Literature study and proposed approach	10
2.2	Experimental campaigns description	13
2.3	Experimental results	26
2.4	Behaviour and failure models identifications	39
2.5	Conclusions	49
2.6	Models parameters summary	50

Resume

The aim of this chapter is to present the experimental protocole used for the bulk adhesive testing. It also provides the results of these experimental tests and the identified models needed for the finite element modelling of bonded joints.



2.1 Literature study and proposed approach

Experimental characterization of behaviour and failure of bonded joints are tackled with different points of view in the literature :

- testing on assemblies,
- testing on bulk materials.

The mainly used technique is realized by achieving test directly on assemblies. Different kinds of loadings can be applied on bonded joints with this experimental method. Tensile/compressive, shear and mixed loadings are obtained with butt, single or double lap and scarf joints respectively (Figure 2.1) [1] [2] [3] [4] [5] . The benefit of these tests is to allow the characterization of bonded joints in conditions near those used in industry. In the particular context of automotive industry, the same metal sheets used for an automotive structure can be used and the chemical composition of adherent surface are the same. Unfortunately these tests suffer of two main problems [7] [8]:

- high stress heterogeneities in the bonded joint,
- global response is highly influenced by the adherent properties,

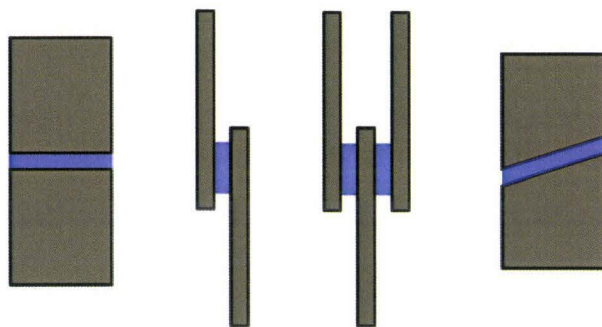


Figure 2.1: Classical bonded joints geometries.

Some special tests devoted to failure characterization of bonded joints are also present in the literature [9] [10] [11] [12]. In these tests, peeling and cleavage loadings are applied on bonded joints so as to identify the adhesion of an adhesive. Although these tests provide a good estimation of failure resistance of an adhesive, the obtained data are not suitable for finite element modeling. Another impact strength tests are also proposed by Goglio et al [13], these tests are based on Charpy's pendulum and provide different stress combinations. All these impact tests suffer of the same problems than the classical assemblies tests (2.1).

These problems and geometical configuration of assembly specimen lead to high difficulty to identify strain and stress inside the bonded joints. To avoid these problems, some analytical models are used like shear lag model [14] but their deployments are always hard and plasticity of adherents is rarely take into account.

Some solutions are proposed in literature to solve the above problems like in the works of

Cognard et al [15] [16] in which a new specimen geometry derived from the Arcan test [17] is designed. This new geometry allows to obtain a more homogenous stress distribution inside the bonded joint. The difficulty of this test is that so as to obtain a good stress field a complex beak is needed near the bonded joint. This beak is only achievable on massive steel specimen and chemical surface composition and industrial conditions are not respected anymore. This new test is also difficult to realize at high strain rates due to important mass of the clamping system.

The other point of view used in the literature to characterize the behaviour and failure of adhesive is to achieve tests on bulk adhesive specimens [18]. This kinds of tests which are used by the chemical industries to identify classical elastic properties, are not very used in the literature in face of the assemblies tests. These bulk tests allow to obtain a very homogeneous stress state inside the specimens and to use classical stress and strain calculations formula. These tests are only limited by two problems:

- industrial conditions are not respected due to huge thickness needed and the absence of adherent,
- it is difficult to obtain pore free sample due to original packaging of industrial adhesive.

In this work, the bulk adhesive specimen testing is chosen so as to characterize the behaviour and failure of a toughened epoxy adhesive. In order to obtain a fine behaviour and failure model various kinds of loadings and a wide strain rate range are needed. This is achieved by realizing tensile, compressive and shear tests using different loading devices. New measurement techniques like 2D and 3D Digital Image Correlation (DIC) [19] [20] are used to identify mechanical properties of the adhesive.

These experimental results lead to the identification of mathematical models which will describe the material behaviour and failure properties. In the literature some visco-elasticity models are already defined on various materials but not on toughened epoxy adhesive [21] [22]. These models are classically identified by complex tests like relaxation and/or creep tests. An alternative method to identify these kinds of models would lead to realize Dynamic Modal Analysis (D.M.A) tests [23] [24]. Although these tests are easy to realize the identification of models'parameters are very complicated due to the complex formulation of the results. In the works of Richeton et al [25], a similar study is realized on a polymer materials and the visco-elasticity is taken into account by a viscous elastic modulus which is formulated by a logarithmic function (equation 2.1).

$$E(\dot{\epsilon}) = a + b \cdot \ln\left(\frac{\dot{\epsilon}}{\dot{\epsilon}_0}\right) \quad (2.1)$$

where a and b are the visco-elasticity parameters and $\dot{\epsilon}_0$ a parameter needed to obtain an adimensional logarithm.

Literature suffers of a lack of visco-plastic models for toughened epoxy adhesives. This part of behaviour is generally done by tabulated behaviour law in finite element codes [26]. For polymer materials the G'Sell model [27] [28] describes the evolution of stress in function of strain and strain rate by means of exponential products as shown in equation 2.2 and 2.3.

$$\sigma = K \cdot \left(1 - e^{-\frac{\epsilon}{\epsilon_V}}\right) \cdot e^{h \cdot \epsilon^2} \cdot \dot{\epsilon}^m \quad (2.2)$$

$$\sigma = K. (1 - e^{-w.\varepsilon}). (1 + a.e^{-b.\varepsilon}). e^{h.\varepsilon^n}. \dot{\varepsilon}^m \quad (2.3)$$

where K is the rigidity parameter, w the visco-elasticity parameter, (h, a, b, n) the structural hardening parameters and m the strain rate sensitivity parameter.

This model is modified in the literature so as to match their specific contexts [29]

$$\sigma = K. (1 - e^{-w.\varepsilon}). (1 + h_1.\varepsilon + h_2.\varepsilon^2). \dot{\varepsilon}^m \quad (2.4)$$

where K is the rigidity parameter, w the visco-elasticity parameter, (h_1, h_2) the structural hardening parameters and m the strain rate sensitivity.

Following this principle, the most advance is realized by EPEE [30]. He proposes to exclude the visco-elasticity phase from the behaviour law by using an additive formulation

$$\sigma = \sigma_y + K. (1 - e^{-w.\varepsilon_p}). (h_1.\varepsilon_p + h_2.\varepsilon_p^n). \dot{\varepsilon}^m \quad (2.5)$$

where σ_y is the yied stress, K the rigidity parameter, w the hook parameter, h_1, h_2, n the structural hardening parameters and m the strain rate sensitivity parameter.

In the literature, volume variation is generally tackled with a plastic Poisson's ratio which is not equal to 0.5 or by a damage model. Damage evolution is generally tackled for the toughened epoxy adhesive with a Gurson damage model [6]. This model describes the evolution of voids. Although this model gives good results for metallic and some polymer-like materials, its parameters are not identified directly on experimental results but often by finite element inverse method [31]. Moreover some parameters (q_1, q_2, q_3) are generally extracted from the literature ($q_1 = 1.5, q_2 = 1, q_3 = 2.25$) and can not fit perfectly damage evolution in both metallic and polymer like materials.

Failure of adhesive in assemblies are often predicted by a critical stress criterion (equation 2.7). Even if this kind of criterion is simple, its identification is not so easy due to the problem linked to the classical assemblies geometries (paragraph 2.1). In finite element software the main failure criterion are based on a critical strain which is also difficult to identify on assemblies tests but are very simple to quantify on bulk specimen testing with new measurement techniques like D.I.C. A failure criterion based on a fixed failure strain is inaccurate if the dependency to the triaxiality stress ratio and the strain rate is not taken into account. For instance the failure criterion proposed by Johnson et al [32] allows the failure strain to evolve with the strain rate but also with the triaxiality stress ratio:

$$\bar{\varepsilon}_f = (D_1 + D_2.e^{-D_3.\eta}). (1 + D_4.ln(\frac{\dot{\varepsilon}}{\dot{\varepsilon}_0})) \quad (2.6)$$

where D_1, D_2, D_3 are parameters which depend on the triaxiality stress ratio η and D_4 is the sensitivity parameter of the equivalent strain rate $\dot{\varepsilon}$. The parameter $\dot{\varepsilon}_0$ is only used to obtain a non-dimensional parameter in the logarithm. Although this criterion gives a good description of dependency on the strain rate, the dependency on the triaxiality stress ratio is only monotonic and does not represent the dependency identified on experimental tests.

Another model (2.7) comes from Wierzbicki et al works [33]. This criterion gives a fine description of the dependance on the triaxiality stress ratio of the failure strain but does not include strain rate effects.

$$\bar{\varepsilon}_f = C_1.e^{-C_2.\eta} - (C_1.e^{-C_2.\eta} - C_3.e^{-C_4.\eta}). (1 - \xi^{\frac{1}{n}})^n \quad (2.7)$$

where η represent the triaxiality stress ratio and ξ the third invariant of the stress tensor, C_1, C_2, C_3, C_4 are the triaxiality stress ratio parameters of the considered material. Here in these works, the visco-elasticity phase is described by a logarithmic model [25] due to its simplicity and the available experimental data. The visco-plasticity is tackled by a new modified G'Sell law following the works of EPEE [30]. Due to the different shapes between the tensile, shear and compressive behaviour laws different mathematical models are then proposed. Due to the complexity of the identification protocol of classical damage model like Gurson one, in this thesis a new model used. This model is identified with the plastic Poisson's ratio evolution captured by D.I.C. techniques. The failure criterion is identified using the workguidelines provided by Wierzbicki et al [33] and Johnson et al [32]. These models are identified to be used in the mesoscopic finite element model (Chapter 3).

2.2 Experimental campaigns description

2.2.1 Bulk adhesive specimen preparation

In order to perform tests on bulk specimens, an original forming process is developed to obtain plates of pure adhesive on the bulk form. An aluminum mould is designed to perform adhesive plates (Figure 2.2a). This mould is initially covered with a teflon film so as to limit adhesion problems. The adhesive is previously stored in a cartridge, and then placed in the mould with an electrical gas gun. Mechanical properties of adhesive are dependent on the temperature, time of curing and pressure level applied during curing phases [34], [35], [36]. In order to reduce these dependancy, the process parameters are controlled using a heating press (Figure 2.2b).

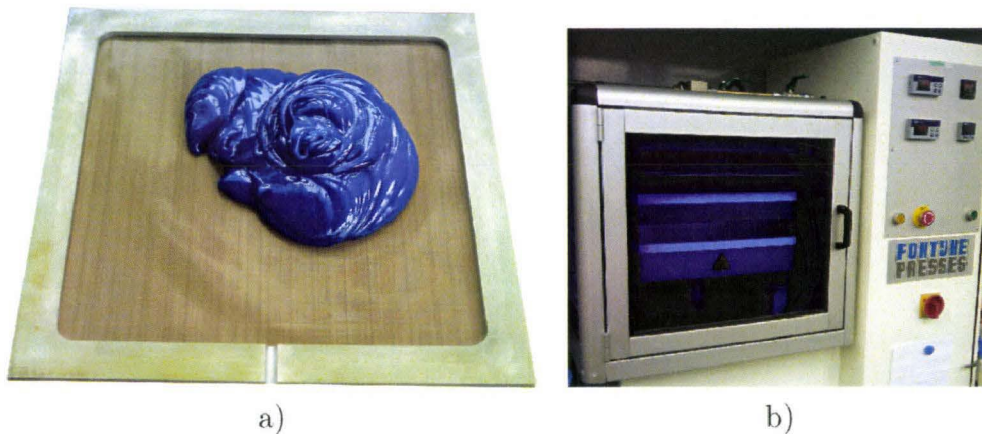


Figure 2.2: description of a) aluminum mould and b) heating press.

With the proposed forming process, pore-free sample remains difficult to obtain [34]. This difficulty has to be seriously threatened due to high strain localization on pore specimen as illustrated in Figure 2.3. The measured strains are also highly influenced by pore as shown in Figure 2.4. In consequence, a control of the porosity is carried out with lightening on

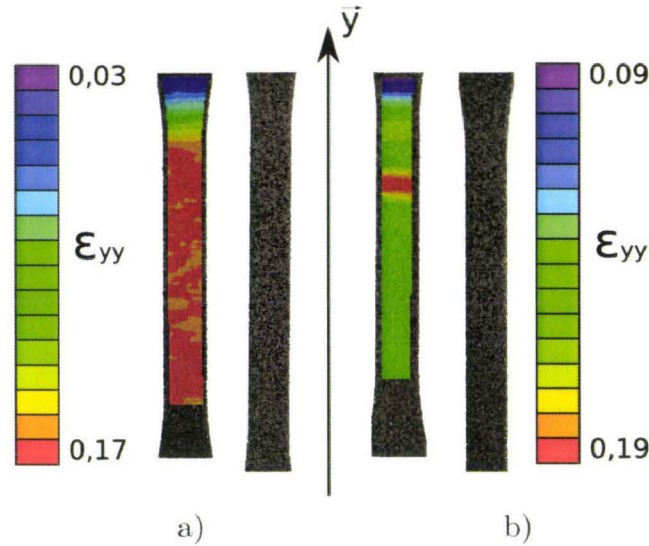


Figure 2.3: difference on strain fields between a) a pore and b) a pore-free specimen.

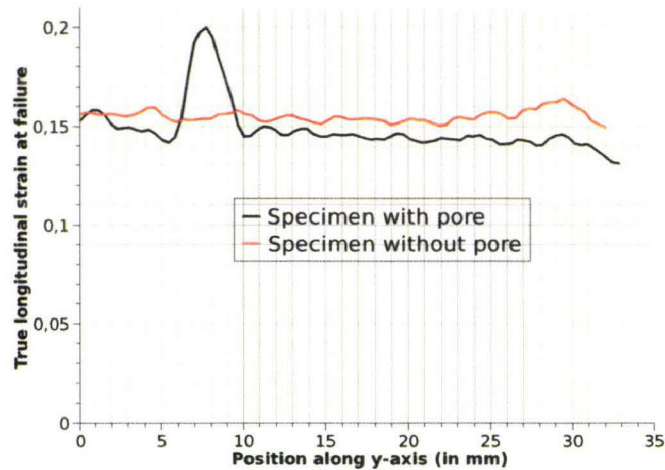


Figure 2.4: distribution of true longitudinal strain at failure on a pore and pore-free specimen.

each plate (Figure 2.5a). The next step consists in the localization of porosity which could not be detected due to their very small size. For that, the micro-tomography technique is used on small samples extracted from the plates (2*3*3mm). The size of the pore are estimated close to 80 μm . These porosities will be taken into account as initial void in further behaviour model developments (Figure 2.5b).

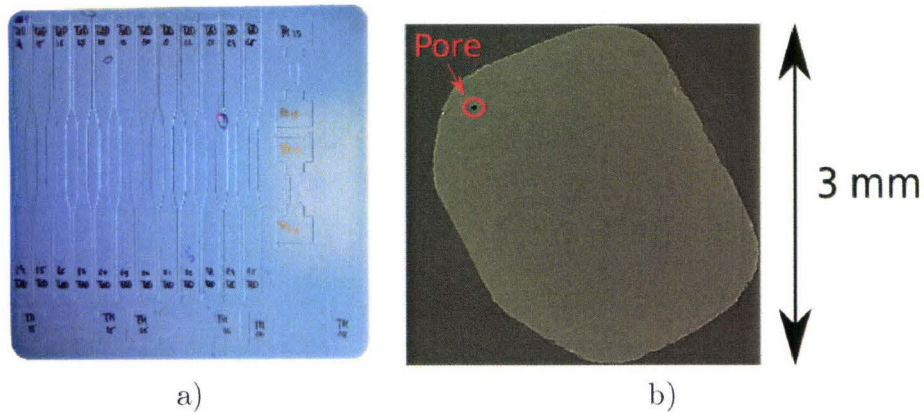


Figure 2.5: a) localization of pores by lighting technique on a plate and b) μ CT scan of adhesive plate.

After this control process, specimens are machined by water-cutting in the adhesive plates. This technique is used so as to reduce the heating of specimens where dramatical issues could be observed by classical machining operations; moreover the risk of crack initiation is reduced.

2.2.2 Presentation of loading devices

In order to cover a wide range of strain rates, different loading devices are needed:

- a classical electro-mechanical machine for the low strain rates range $[0.01;0.1] \text{ s}^{-1}$,
- a high speed hydraulic machine for the intermediate strain rates range $[0.1;100] \text{ s}^{-1}$ (Figure 2.6 a) b)),
- Hopkinson bars for the high strain rates range over 100 s^{-1} (Figure 2.7 a) b)).

The classical tensile tests are performed on the $[0.01 ; 400] \text{ s}^{-1}$ range using the three loading devices described above while the notched tensile tests are only achieved on the electro-mechanical and highspeed hydraulic machines but lead to the same strain rate range as the classical tensile tests due to the presence of the notch. Compressive tests are achieved on the $[0.53 ; 5000] \text{ s}^{-1}$ range using the high speed hydraulic machine and a set of visco-elastic Hopkinson bars made of PA66. The shear tests performed with Iosipescu device are only limited to low strain rate (0.02 s^{-1}) due to the complexity of the clamping system (Figure 2.8).

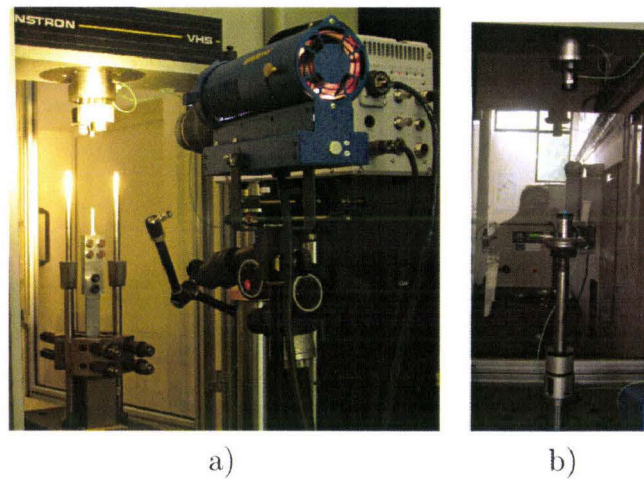


Figure 2.6: high speed hydraulic a) tensile and b) compressive configurations.



Figure 2.7: a) pre-stressed tensile and b) visco-elastic compressive Hopkinson bars.

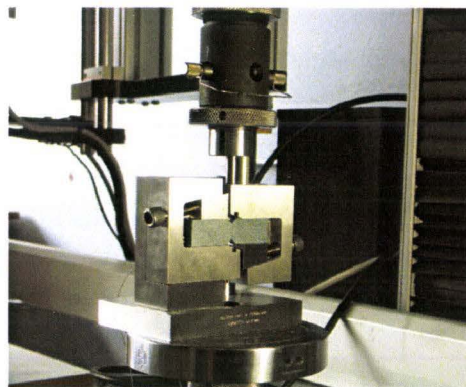


Figure 2.8: Iosipescu shear test device.

2.2.3 Presentation of specimen geometries

For the classical tensile tests, a normative geometry is used (NF-EN-ISO-527-3) for the low strain rate range (Figure 2.9). This geometry is slightly modified so as to be adapted to the high speed hydraulic machine jack (Figure 2.10). For the pre-stressed Hopkinson bars an innovative geometry is used (Figure 2.11 a) and finite element simulations are made in order to quantify the geometry effect on the strain fields (Figure 2.11 b).

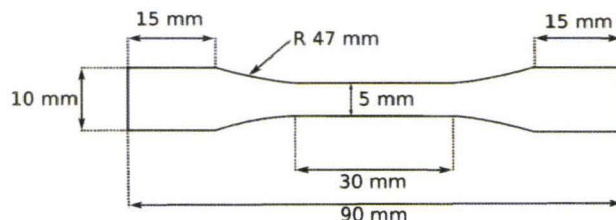


Figure 2.9: normalized geometry of specimen for low strain rate range (thickness 4mm).

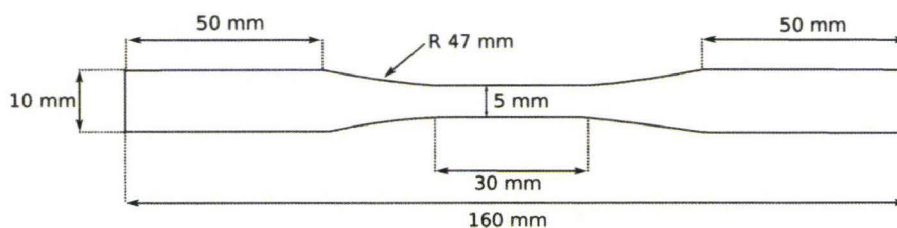


Figure 2.10: modified samples based on normalized geometry used for highspeed hydraulic machine (thickness 4mm).

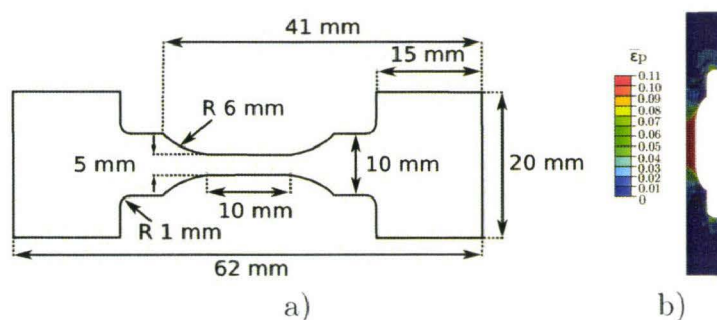


Figure 2.11: a) specimen geometry for the Hopkinson tensile testing (thickness 4mm) and b) F.E. results in terms of equivalent plastic strain.

The notched tensile specimens geometry which will be used for the failure criterion is based on the classical tensile geometries with simply a half hole on each side of the specimen (Figure 2.12). As for the classical tensile tests, the notched specimen geometry is modified for high speed hydraulic machine jack (Figure 2.13).

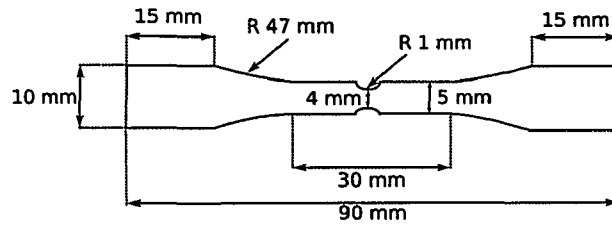


Figure 2.12: notched specimen used for low strain rate range (thickness 4mm).

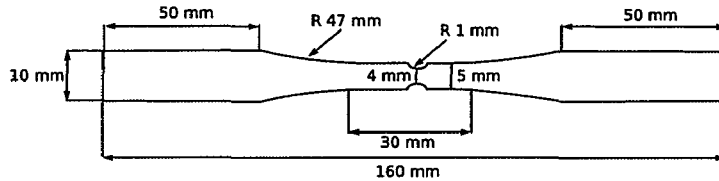


Figure 2.13: notched specimen used for highspeed hydraulic machine (thickness 4mm).

The compressive test geometries are extracted from the NF-ISO-604 norm (Figure 2.14a). A simple formula is given to determine the ratio between height and radius of the specimen according to a critical plastic strain:

$$\varepsilon_{crit} \leq 0,4 \cdot \left(\frac{x}{h}\right)^2 \quad (2.8)$$

where ε_{crit} is the critical plastic strain, x is the radius of the cylinder specimen and h is the height of the cylinder. A critical plastic strain close to 0.5 is considered here for calculations. Two different geometries are used as shown in Figure 2.14, these two specimen geometries are cured under two pressures (1 MPa and 4 MPa) so as to study the influence of curing pressure on the mechanical properties of the chosen toughened epoxy adhesive.

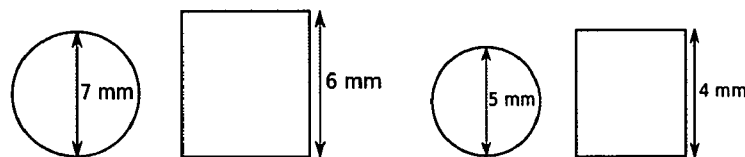


Figure 2.14: normalized geometry of the compressive specimen.

The shear loading is obtained by the flexure of a V-notched beam, this test which is originally designed for composite materials is called the Iosipescu test. The Iosipescu shear geometry is extracted from the ASTM norm D5379 (Figure 2.15).

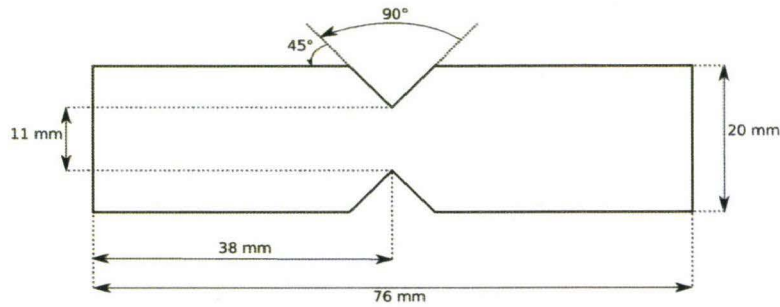


Figure 2.15: normalized geometry of the Iosipescu shear specimen.

2.2.4 Presentation of measurement techniques

To identify the behaviour and failure of the toughened epoxy adhesive, two variables are needed the force and the displacement obtained during tests. The force measurements are adapted to the loading device:

- a classical strain gaged cell force for the electromechanical machine,
- a piezo-electric cell force previously calibrated on the force range for the high speed hydraulic machine,
- a strain gage bridge for the Hopkinson bars.

The strain fields are achieved by both contact and non-contact methods. Contact method is realized by classical strain gages, typical low elongation strain for the tensile elasticity measurement while shear elasticity and plasticity measurements are realized with high elongation strain gaged. All strain gages used for tensile measurements are bonded using typical cyanoacrylate adhesive while strain gages used for shear measurements (Figure 2.16) are bonded with a special cyanoacrylate adhesive especially designed for high elongation. Adhesive of strain gage is reticulated at room temperature for 24 hours under pressure applied with a special purpose spring clamp.

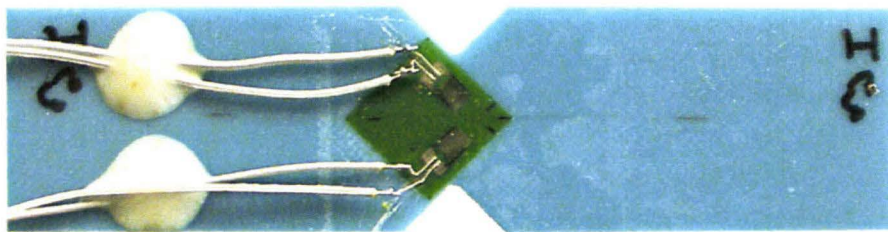


Figure 2.16: strain gages on Iosipescu specimen.

Two non-contact measurement techniques are used to obtain the displacements fields. For the compressive tests an electro-optical extensometer Zimmer with a bandwidth 250 kHz is used (Figure 2.17a). This device follows two black/white transition markers exposed



Figure 2.17: configuration of a) electro-optical extensometer and b) 3D DIC.

to a homogenous lighting. It determines in real time the current displacement and gives the possibility of calculating true total strain from quasi-static to dynamic loadings. The other non-contact methods used is the Digital Image Correlation (D.I.C.) technique under its 2D and 3D forms (Figure 2.17b). In order to estimate the out-of-plane displacements, 3D DIC is used on a static classical tensile test (0.02 s^{-1}). This test proves that out-of-plane displacements are smaller than the spatial resolution of DIC. 2D DIC is used for the rest of the classical and notched tensile tests. 3D DIC is used to analyse the quality of the compressive and shear tests but also to identify the true equivalent failure strain of shear tests. For all the DIC calculations, a strain length of $300 \mu\text{m}$ is used. For the acquisition of the pictures needed for the D.I.C. calculations two kinds of cameras are used:

- a CCD captor with a 10 f.s^{-1} acquisition rate for the low strain rate tests
- a CMOS captor with a 50, 1000, 15000, 37500 f.s^{-1} acquisition rate for the middle and high strain rate tests

2.2.5 Description of behaviour law computations

In order to establish a visco-plastic behaviour, three variables are needed, the true equivalent strain, the true equivalent strain rate and the true stress. Three kinds of computations are used for the tensile, compressive and shear tests. Due to the limitation of strain rate, the shear plastic behaviour is not establish under visco-plastic behaviour.

For the tensile test, the true equivalent strain is obtained from:

$$\bar{\varepsilon} = \sqrt{\frac{2}{3} \cdot \bar{\varepsilon} : \bar{\varepsilon}} \quad (2.9)$$

where $\bar{\varepsilon}$ is the strain tensor filled by DIC calculations.

True strain rate is obtained by backward finite difference following:

$$\dot{\bar{\varepsilon}} = \frac{\bar{\varepsilon}(t) - \bar{\varepsilon}(t - \Delta t)}{\Delta t} \quad (2.10)$$

where Δt is the time step of the CCD or CMOS captor.

This kind of derivate calculation leads to noisy results so a numerical smooth is applied as illustrated in Figure 2.18. This numerical smooth is based on a local regression using weighted linear least squares and a 2^{nd} degree polynomial model, the method assigns lower weight to outliers in the regression and zero weight to data outside six mean absolute deviations

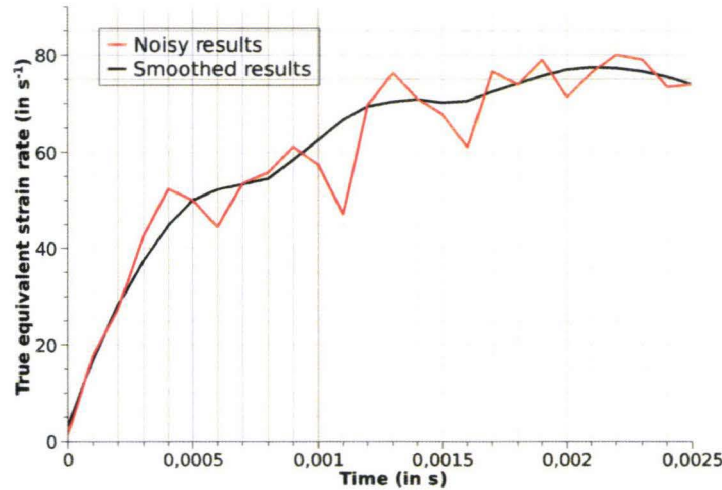


Figure 2.18: difference between noisy and smoothed data.

For the tensile tests, the true stress is computed using:

$$\sigma_t = \frac{F}{S_0} \cdot e^{-\varepsilon_{22}} \cdot e^{-\varepsilon_{33}} \quad (2.11)$$

where F is the current force in the specimen, S_0 the initial cross-section of the specimen and ε_{22} , ε_{33} the strain of the cross section. To define the tensile visco-plastic behaviour law the $SE\dot{E}$ method is used [37]. This technique, previously developed in the LAMIH laboratory, uses the heterogeneity of the strain field during a tensile test to establish a visco-plastic behaviour law (Figure 2.19a & b).

The behaviour law at constant strain rate is then extracted by a numerical cut of the 3D behaviour surface established in the true strain, true strain rate and true stress space by $SE\dot{E}$ method (Figure 2.20a & b).

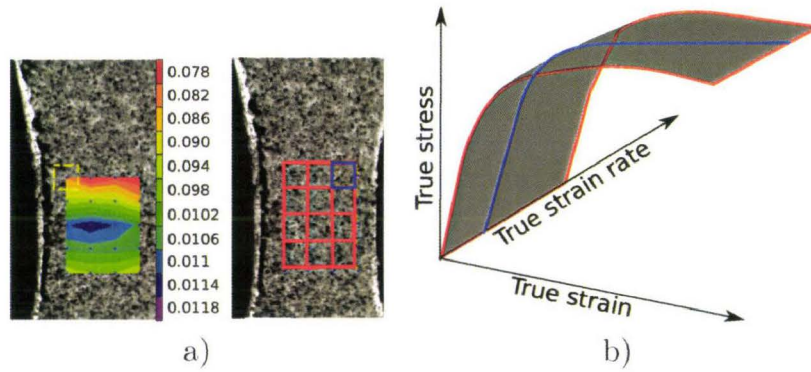


Figure 2.19: description of a) heterogeneous strain fields and b) behaviour surface.

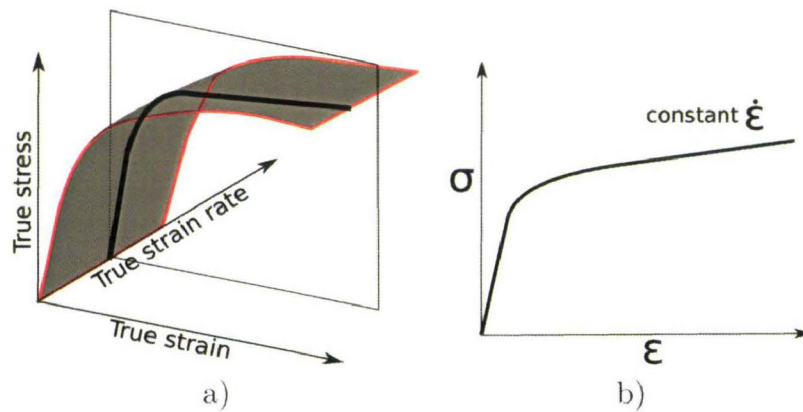


Figure 2.20: description of a) Numerical cut of surface and b) true behaviour law at constant strain rate.

For the compressive behaviour law, the same formula as tensile behaviour law is used (eq 2.11). Indeed only the longitudinal strain ϵ_c is obtained from the electro-optical extensometer. Then appropriated hypothesis has to be made to determine the cross-sections strains ϵ_{22} and ϵ_{33} .

$$\epsilon_c = \ln\left(1 + \frac{\lambda}{h_0}\right) \quad (2.12)$$

where λ is the current elongation given by the electro-optical extensometer and h_0 the initial height of the specimen. As for the establishment of a visco-plastic behaviour the strain rate is needed, for the compressive test the true strain rate for compressive tests is compute following equation 2.10.

The shear behaviour law is obtained following:

$$\sigma_{shear} = \frac{F}{S_0} \quad (2.13)$$

in which F is the total strength of the specimen and S_0 the initial cross section.

The shear strain needed for the behaviour law is determined by:

$$\gamma_{12} = |\epsilon_{-45^\circ}| + |\epsilon_{+45^\circ}| \quad (2.14)$$

where ε_{-45° and ε_{+45° are the strains measured by the gages oriented at $\pm 45^\circ$.

2.2.6 Description of failure strain computation

The failure strain computation is only limited by two questions:

- when it is computed ?
- where it is computed ?

For compressive tests, the failure detection is realized directly on the stress/strain response of the test. As illustrates in Figure 2.21, the failure initiation is located at the first stress/strain curve inflexion. The uncertainty, linked to this kind of identification technique, is totally neglected in front of the natural dispersion of failure phenomenon. For the computation location the true strain in compressive tests comes from a global elongation measurement, then the strain field is assumed to be homogeneous and there is no influence of the location.

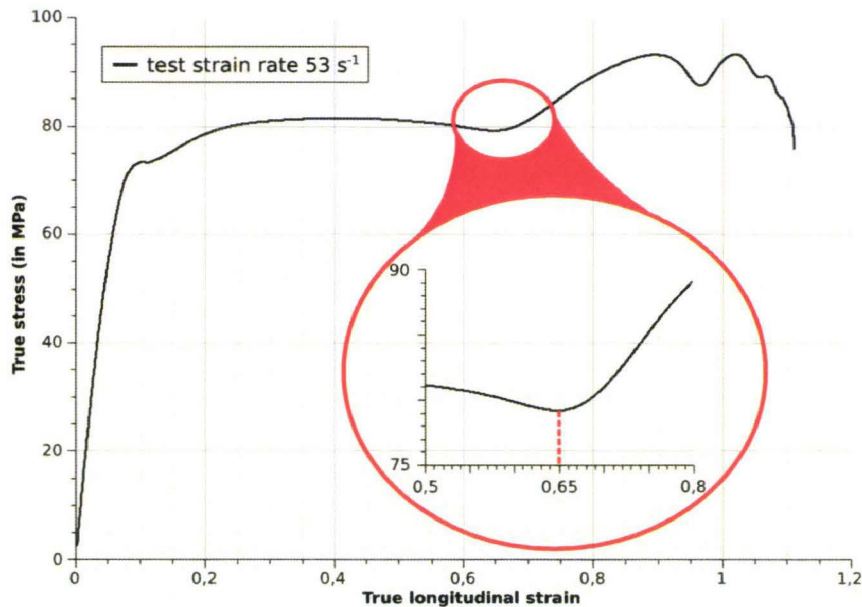


Figure 2.21: failure detection technique for compressive tests.

For the classical, notched tensile and the shear tests, the digital image correlation technique is used. With this kind of measurement method the identified failure strain depends on the last picture used for the displacements measurement. As illustrates in Figure 2.22, the last picture used is the previous of the first one on which a crack is clearly visible. This kinds of considerations lead to an uncertainty on the failure strain which is evaluated by :

$$\Delta \bar{\varepsilon}_f = \frac{\Delta t \cdot \dot{\bar{\varepsilon}}_f}{\bar{\varepsilon}_f} \cdot 100 \quad (2.15)$$

where $\Delta \bar{\varepsilon}_f$ is the failure strain uncertainty, Δt is the CCD or CMOS captor frame acquisition rate, $\dot{\bar{\varepsilon}}_f$ and $\bar{\varepsilon}_f$ are the mean failure strain and strain rate respectively observed at

the considered frame acquisition rate.

Figure 2.23 illustrates the results in term of uncertainty on the failure strain on the various frame acquisition rate used. The maximum uncertainty observed is equal to 8.2 percent, this uncertainty has to be correlate to the natural dispersion of failure phenomenon. The failure detection technique has a small influence on the dispersion of the failure strain value.

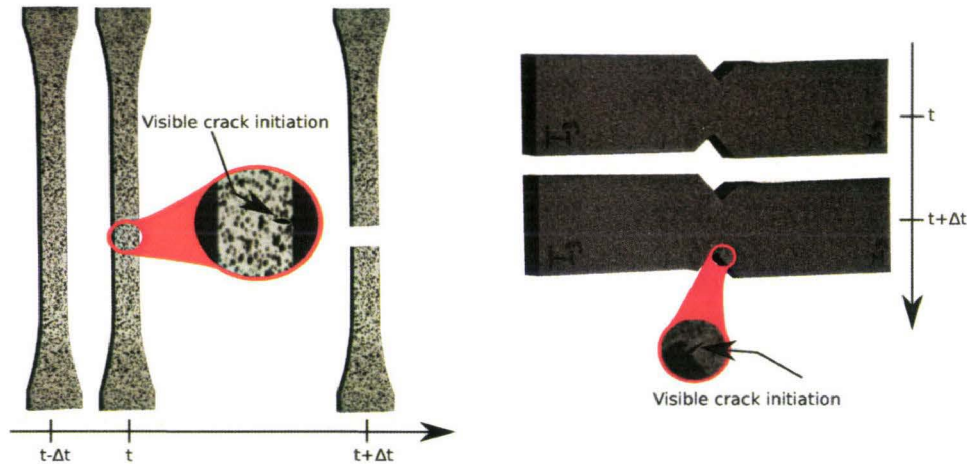


Figure 2.22: failure detection technique used for tensile, notched tensile and shear tests.

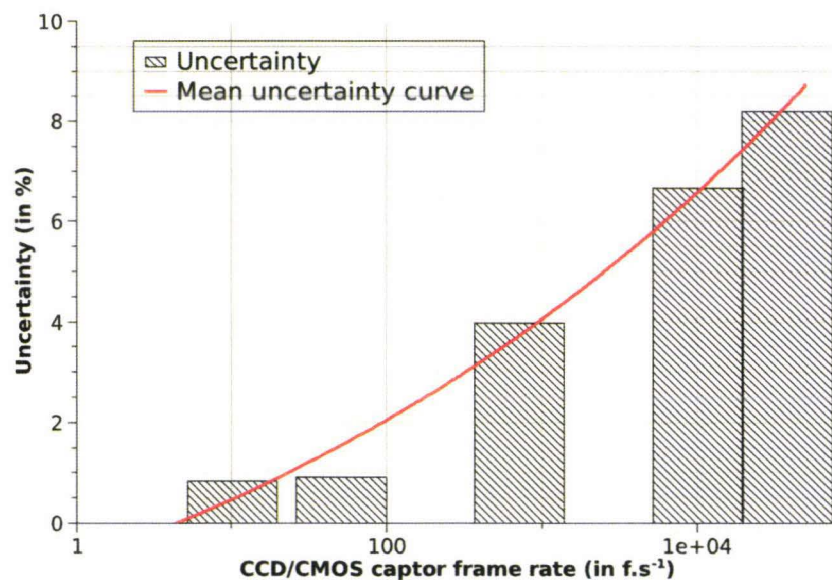


Figure 2.23: computed uncertainty for the various frame acquisition rate.

For the second question "Where is it computed ?", in the classical tensile test the true strain is computed in the center of the specimen in the zone where a crack appears. The center is chosen so as to avoid boundary effects on the DIC calculations. For the notched tensile test, the strain field is heterogenous by definition in the specimen (Figure 2.24a). This heterogeneity is neglected when the DIC strain length calculations is chosen close to $300\mu\text{m}$ (Figure 2.24b).

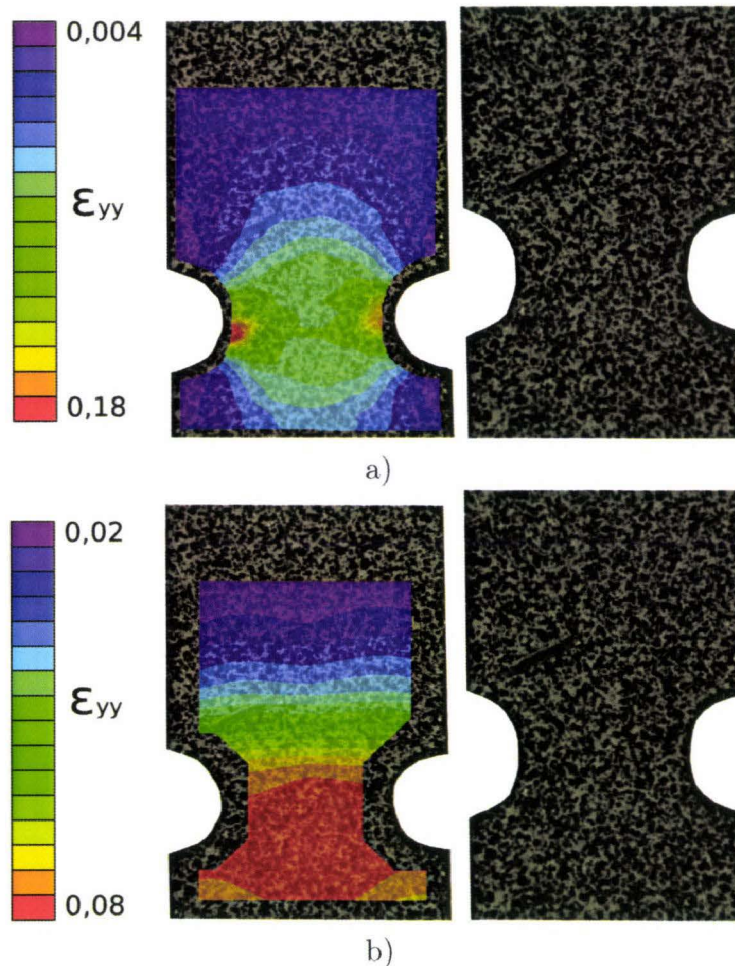


Figure 2.24: a) true longitudinal strain field with a $8\mu\text{m}$ strain length calculation and b) true longitudinal strain field with a $300\mu\text{m}$ strain length calculation.

In the shear tests the true equivalent failure strain is computed in the center of the specimen to avoid edge effects. As for the notched tensile tests, the shear tests are also submitted to heterogenous strain fields but with a DIC strain length calculations close to $300\mu\text{m}$, this heterogeneity is neglected as (Figure 2.25).

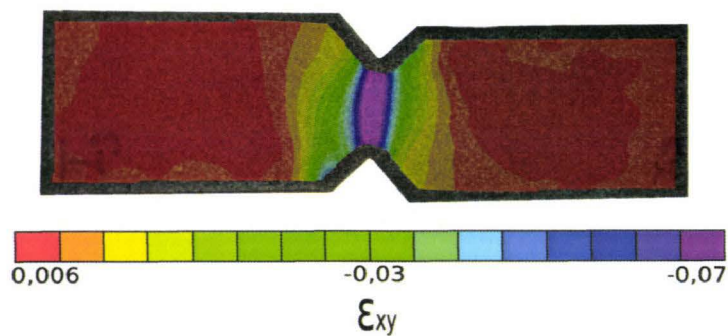


Figure 2.25: shear strain contour plot for a Iosipescu shear specimen.

2.3 Experimental results

2.3.1 Elasticity

The tensile elastic modulus is computed with the rules providing by the NF-EN-ISO-527-3 norm. This norm indicates that the elastic modulus has to be computed between two points (50 and $200 \mu\epsilon$). In order to study the visco-elasticity of the adhesive, these calculations are carried out at two different strain rates on 3 specimens at each speed. Although the range of strain rate is small ($5.3 \cdot 10^{-3}$ to 53 s^{-1}), the evolution of the tensile elastic modulus in function of the strain rate shows a significant visco-elasticity phenomenon (Figure 2.26).

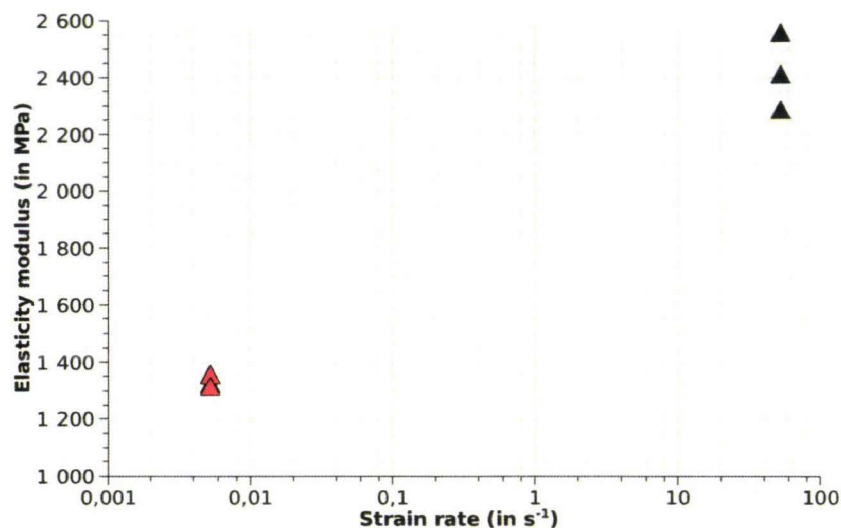


Figure 2.26: evolution of the tensile elastic modulus in function of the strain rate.

These tensile tests show also an influence of the strain gage location on the strain field. This phenomenon is highlighted in Figure 2.27 with the repartition of longitudinal strain along the height of the specimen. The strain gage specimen shows a low failure strain (0.17) compared to the non-strain gage one (0.32). This influence is only restricted

to the plasticity (Figure 2.28) and not affect the elastic modulus measurement.

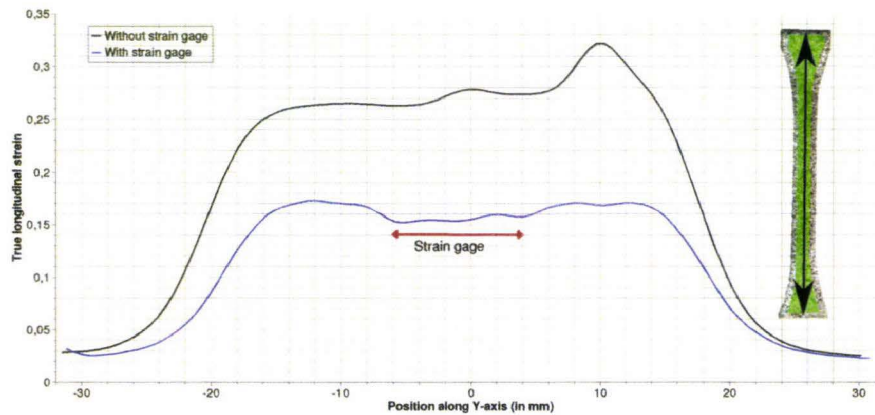


Figure 2.27: repartition of longitudinal strain along the height of the strain gage specimen and the free one.

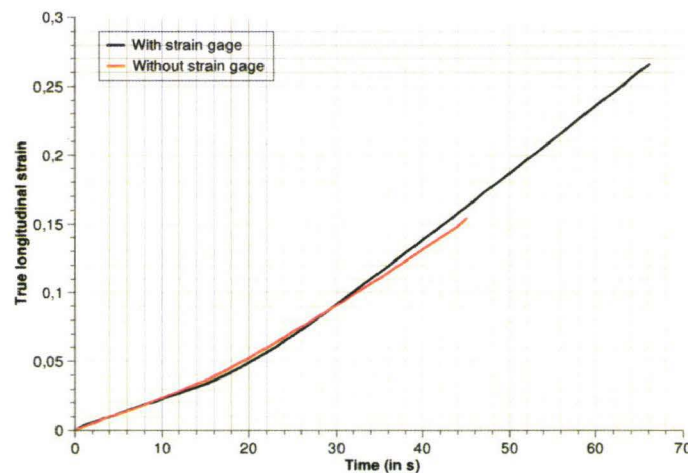


Figure 2.28: influence of strain gage on the true longitudinal strain in center of specimens.

Elastic compressive moduli are identified on the first straight slope of the true strain - true stress curves for different strain rates. Visco-elasticity in compressive is a highly non-linear phenomenon and it also shows a dependency on the pressure applied during curing (Figure 2.29). This last dependency seems to be function on the strain rate too but more tests with different pressures applied are needed to conclude on it.

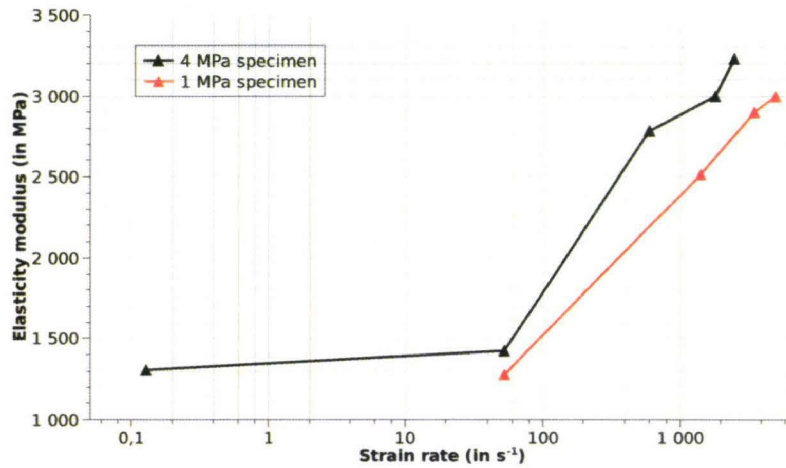


Figure 2.29: evolution of compressive elasticity modulus in function of strain rate and curing pressure.

The elastic shear modulus is computed following the ASTM D5379 norm (Figure 2.30). By linking this result with the isotropic definition of shear modulus G (2.16) and a Poisson's ratio of 0.42, the same magnitude of tensile elasticity modulus at low strain rate is obtained. This last point justifies the fact that the toughened epoxy adhesive is considered as isotropic in the normal plane where the curing pressure is applied.

$$G = \frac{E}{2 \cdot (1 + \nu)} \quad (2.16)$$

where E is the tensile elasticity modulus and ν the Poisson ratio.

As for tensile measurements, the influence of the strain gages is studied with 3D digital

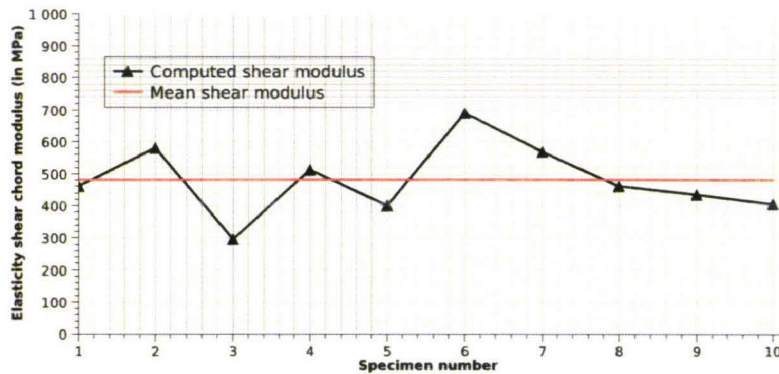


Figure 2.30: computed elasticity shear chord modulus.

image correlation. As shown in Figure 2.31, strain gages have no influence on the results, contrary to tensile tests (Figure 2.27 and 2.28).

To conclude the elasticity investigation, it is shown in Figure 2.32 that visco-elasticity is

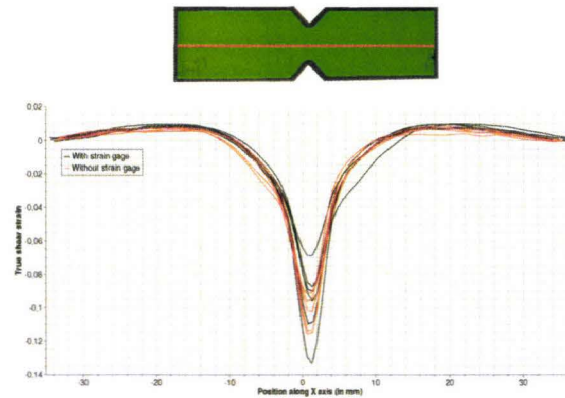


Figure 2.31: influence of strain gage on the true shear strain.

a non negligible phenomenon, that tensile and compressive elastic moduli are different and that pressure applied during curing has a strong influence on the magnitude of the elastic modulus.

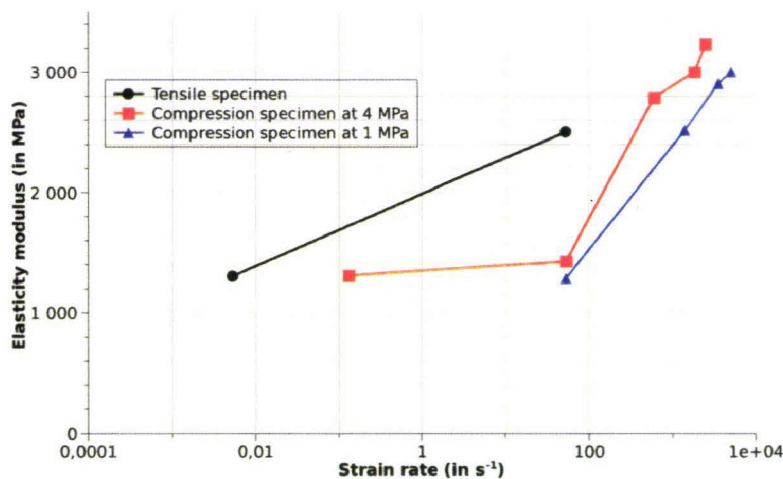


Figure 2.32: synthesis on the elastic moduli measurements.

2.3.2 Plasticity

2.3.2.1 Tensile plasticity

The tensile behaviour laws are identified by the $SE\dot{E}$ method, this method, as shown in paragraph 2.2.5, needs an hypothesis to compute the true stress following equation 2.11. For the behaviour law shown in Figure 2.34 the transversal isotropy hypothesis is used. The transversal isotropy hypothesis postulates that in the cross section of a specimen, ε_2 and ε_3 are equal. This hypothesis is validated by 3D image correlation technique by measuring the strain fields on the front and the side of the specimen at the same time. A maximum deviation of $350 \mu\varepsilon$ is observed between front and side strains (Figure 2.33).

This difference is negligible in front of the other strain magnitudes. Transversal isotropy is validated. The true stress/true strain curves illustrate in Figure 2.34 highlight a high

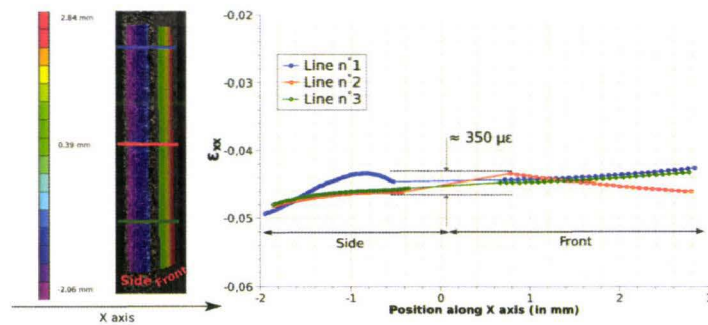


Figure 2.33: transversal strain on the cross section of the tensile specimen.

visco-plastic character. These curves show a structural softening after a certain amount of strain. This can be explained with transversal isotropy calculation which implies the volumetric strain developed during plasticity and furthermore damage. It is noticed that this softening evolves with strain rate.

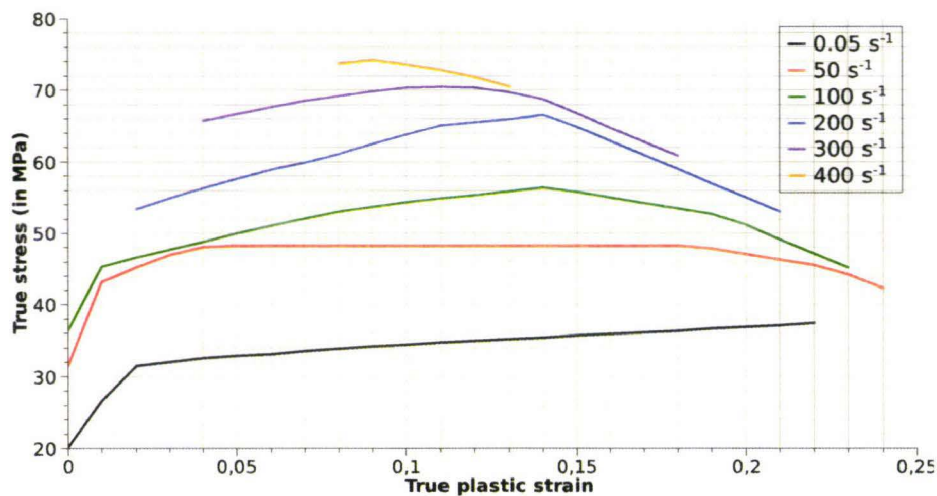


Figure 2.34: true stress / true plastic strain curves obtained with $SE\dot{E}$ method.

2.3.2.2 Compressive plasticity

The true stress responses of compressive tests are computed with equation (2.11). As for the tensile plasticity an hypothesis is needed for the cross-section strains ε_{22} and ε_{33} . With the assumption that no damage occurs in compression, the incompressibility hypothesis is then chosen. This hypothesis is formulated as follows:

$$\varepsilon_{11} + \varepsilon_{22} + \varepsilon_{33} = 0 \quad (2.17)$$

and the compressive behaviour law is then formulated as:

$$\sigma_c = \frac{F}{S_0} \cdot e^{-\varepsilon_c} \quad (2.18)$$

where F is the current load in the specimen, S_0 is the initial cross-section and ε_c is the compression strain.

Curves on Figure 2.35 and Figure 2.36 show a significant visco-plasticity and saturation phenomenon up to 1800 s^{-1} .

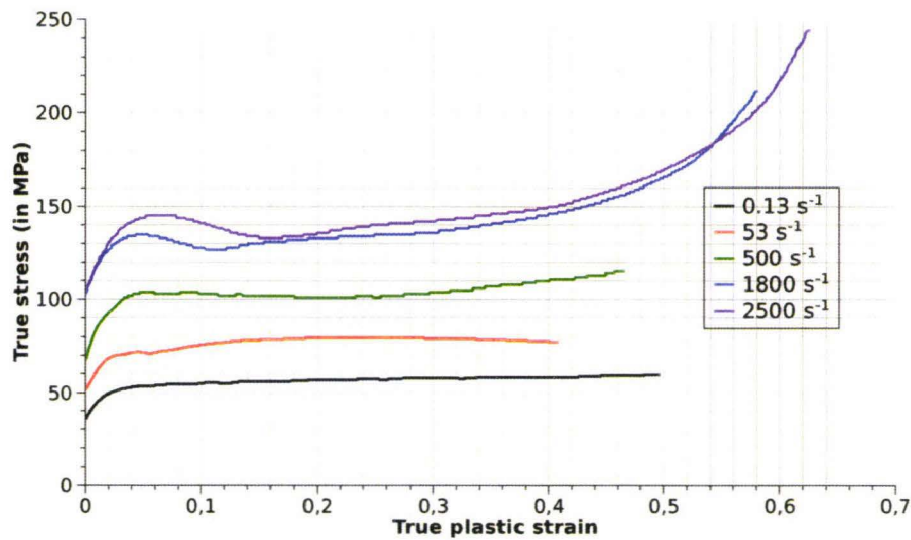


Figure 2.35: true stress versus true plastic strain for 4 MPa curing pressure specimen.

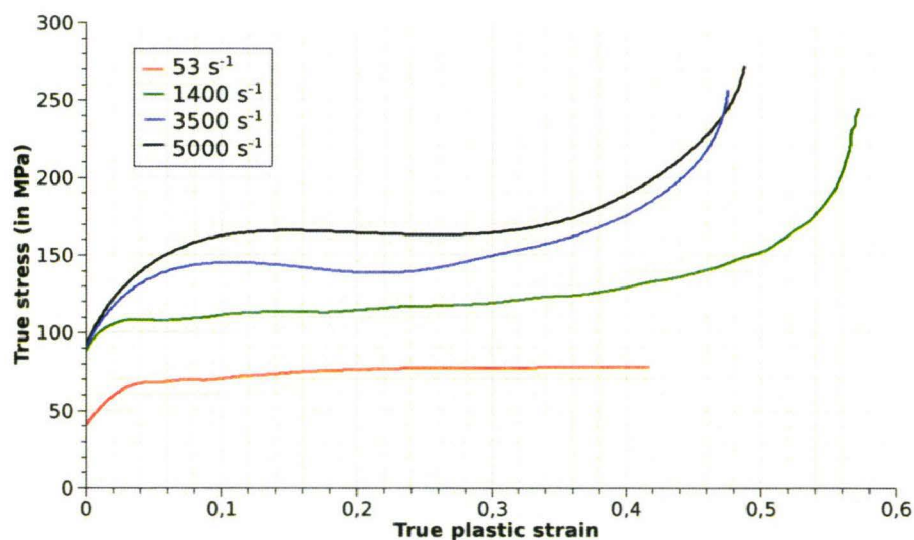


Figure 2.36: true stress versus true plastic strain for 1 MPa curing pressure specimen.

4 MPa curing specimens show a hook at the beginning of the curve (≥ 0 and ≤ 0.1 true plastic strain) for high strain rate loadings only, this hook is not clearly visible on the 1MPa specimens. These curves also show a structural hardening around 0.5 of true plastic strain. A visible difference in stress level between the two curing specimen series is observed at the same strain rate (Figure 2.37).

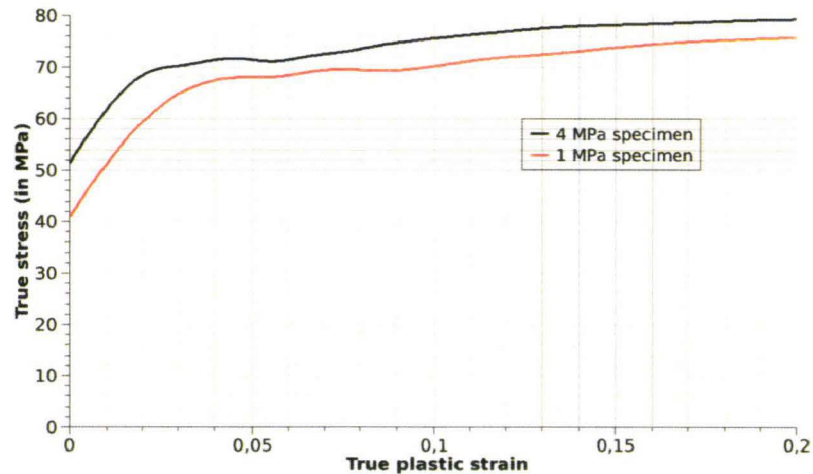


Figure 2.37: influence of curing pressure on the stress level of toughened epoxy (53 s^{-1}).

The validity of the results in terms of stress and strain is checked by controlling the shape of the specimen during the test with 3D digital image correlation (Figure 2.38). These measurements prove that no buckling phenomena occur during the tests.

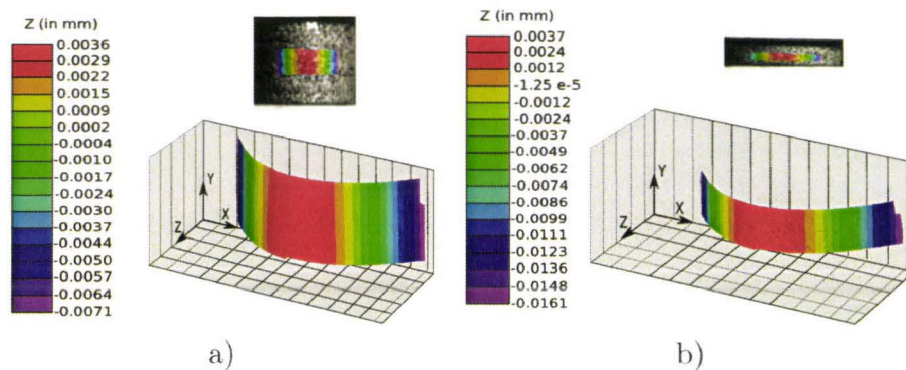


Figure 2.38: a) initial shape and b) deformed shape with a true strain of 0.5.

2.3.2.3 Shear plasticity

The shear behaviour law is computed by equations 2.13 and 2.14. Before to present the shear behaviour law, a fine study on the quality of the shear loading is needed. The principal directions of the diagonalized strain tensor are observed. This is possible with 3D digital image correlation calculations (Figure 2.39). In this figure, it can be seen that principal vectors are always oriented at $\pm 45^\circ$ of the neutral axis of the specimen but this consideration is not sufficient to confirm the pure shear stress state.

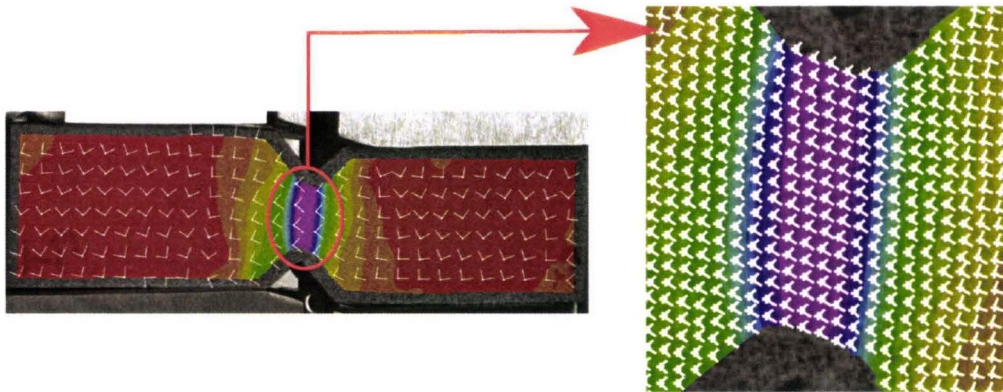


Figure 2.39: principal directions of diagonalized strain tensor.

In addition, the magnitude of the eigen values of the strain tensor have to be checked. This is illustrated in Figure 2.40 which shows the evolution of principal strains during a test on three points of the specimen (top, middle, bottom). At the middle of the test (around 15 s) difference between the principal strains is negligible (less than $300 \mu\epsilon$) but near failure this difference increases (more than $20000 \mu\epsilon$) and shear loading conditions are no longer respected.

These considerations lead to a confidence interval on the behaviour law extracted from the shear test (Figure 2.41).

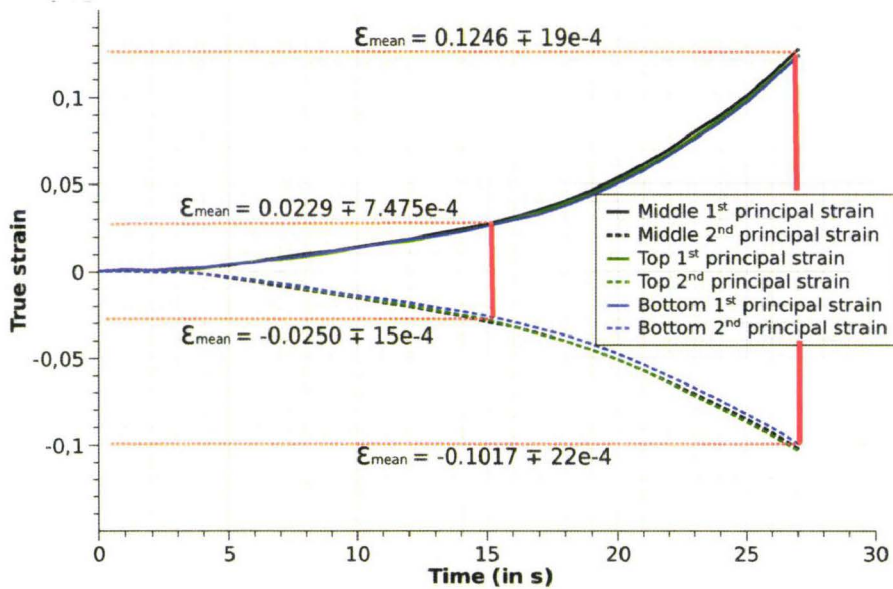
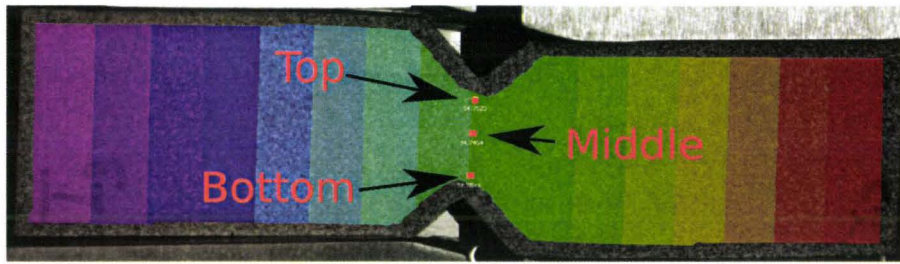


Figure 2.40: evolution of local principal strains during an shear test.

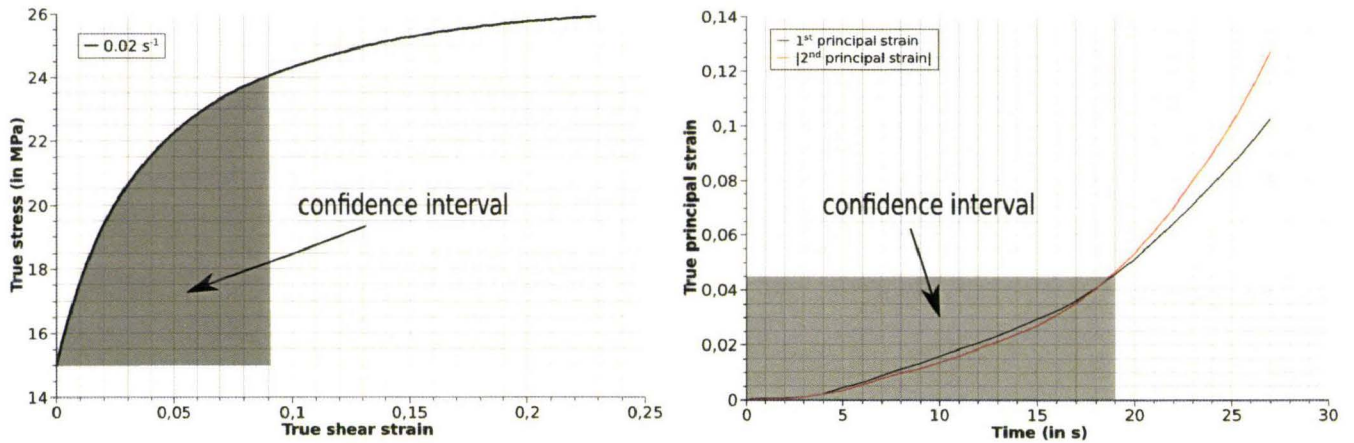


Figure 2.41: shear behaviour law and confidence interval.

2.3.2.4 Non-isochoric plasticity

The non-isochoric plasticity is studied through the evolution of plastic Poisson's ratio obtained by DIC calculations. The value of plastic Poisson ratio decrease with the increase

of plastic strain (Figure 2.42). This evolution and the value of plastic Poisson ratio (different to 0.5), proves the non-isochoric plastic behaviour and the presence of damage. The difference between the identified plastic Poisson's ratio on classical and notched tensile tests indicates that triaxiality stress ratio has a great influence on damage evolution.

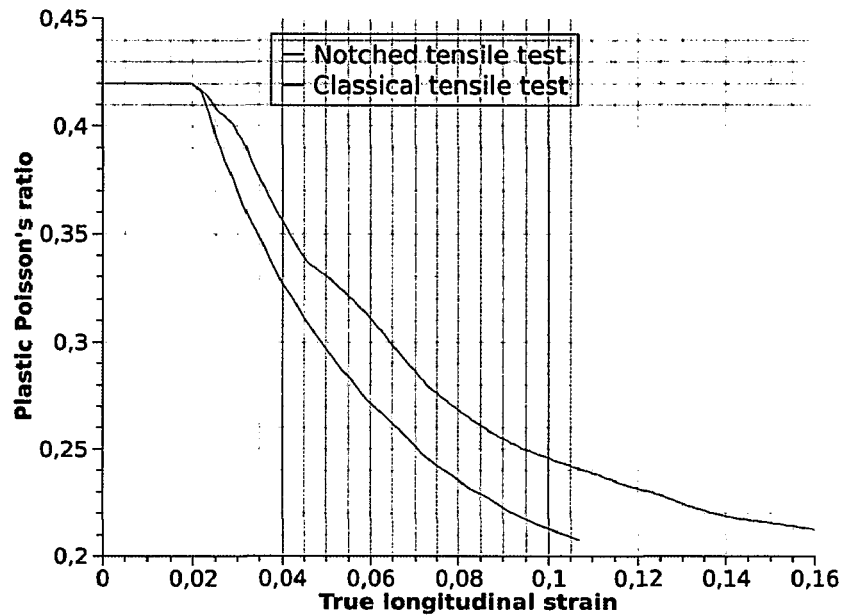


Figure 2.42: evolution of plastic Poisson's ratio.

2.3.2.5 Summary on plasticity

Figure 2.43 shows the evolution of the yield stresses in tensile, shear and compressive for two curing pressures in function of strain rate. A non negligible difference is clearly visible between tensile and compressive behaviour in opposition of shear and tensile behaviours look the same. In addition to these remarks a high visco-plasticity character is shown. In terms of plasticity, a significant difference between tension and compressive behaviours is shown (Figure 2.44).

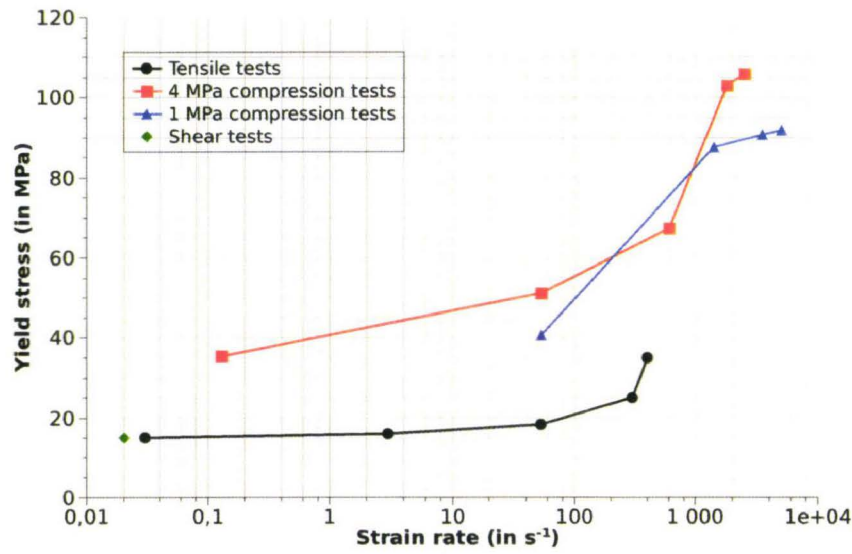


Figure 2.43: comparison between tensile, compressive and shear yield stresses.

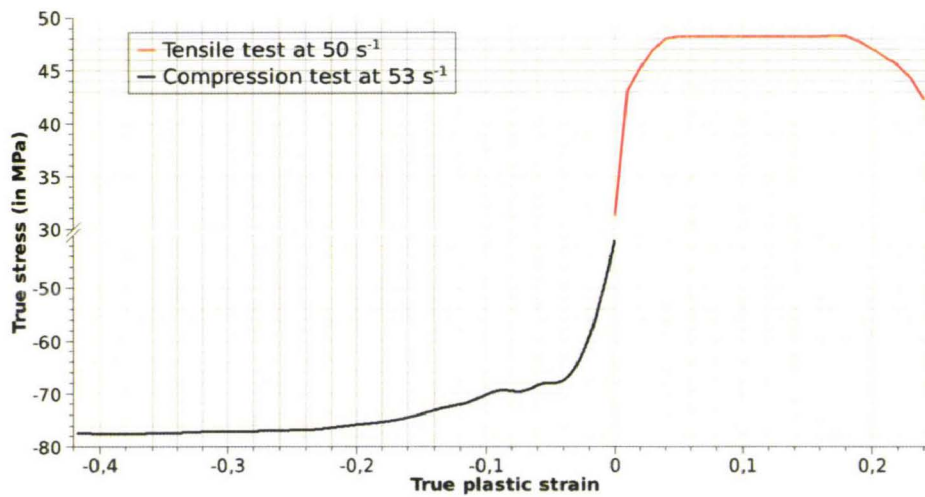


Figure 2.44: comparison between tensile and compressive plasticity behaviour.

2.3.3 Failure

For the classical and notched tensile tests, the true equivalent failure strain is computed following equation 2.9 in which $\bar{\bar{\epsilon}}$ is equal to:

$$\bar{\bar{\epsilon}} = \begin{bmatrix} \epsilon_{11} & \epsilon_{12} & 0 \\ \epsilon_{12} & \epsilon_{22} & 0 \\ 0 & 0 & \epsilon_{22} \end{bmatrix}. \quad (2.19)$$

The simplifications applied on the strain tensor $\bar{\bar{\epsilon}}$ are in total accordance with the transversal isotropy hypothesis mentioned above. Although the shear strain ϵ_{12} is negligible, the

strain value furnish by DIC computation is taken into account.

The evolution of true equivalent failure strain in function of true equivalent failure strain rate for the classical tensile test is shown in Figure 2.45. A real dependency on the strain rate is shown on the evolution of true equivalent failure strain in function of the equivalent failure strain rate (Figure 2.45).

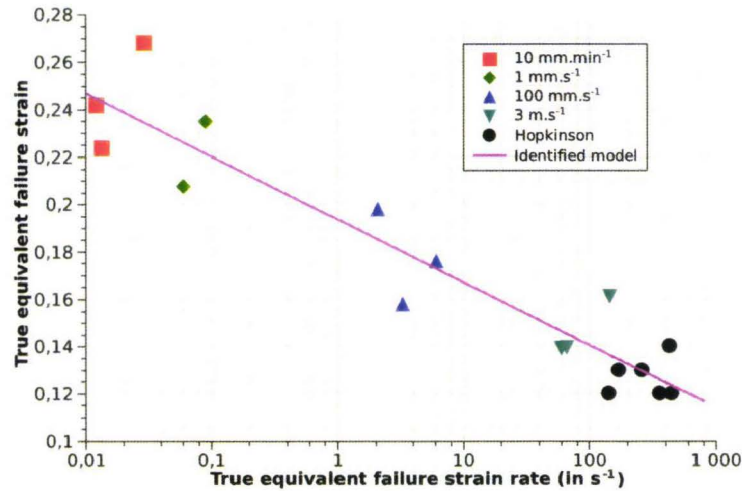


Figure 2.45: evolution of equivalent failure strain of tensile specimens in function of the equivalent strain rate.

The evolution of the true equivalent failure strain obtained during notched tensile tests in function of the true equivalent strain rates is illustrated in Figure 2.46. The dependence of the equivalent failure strain to the strain rate is confirmed.

For the shear tests, the true equivalent failure strain is computed following equation 2.9 in which $\bar{\bar{\epsilon}}$ is equal to:

$$\bar{\bar{\epsilon}} = \begin{bmatrix} \epsilon_{11} & \epsilon_{12} & 0 \\ \epsilon_{12} & \epsilon_{22} & 0 \\ 0 & 0 & 0 \end{bmatrix}. \quad (2.20)$$

The simplifications applied on the strain tensor $\bar{\bar{\epsilon}}$ are in total accordance with the plane strain hypothesis which takes place in shear test. Although the volumic strains ϵ_{11} and ϵ_{22} are negligible, the strain value furnish by DIC computation are taken into account. Due to important dispersion, a mean value for the equivalent failure strain is chosen as illustrated in Figure 2.47. As the Iosipescu is only performed at one loading speed, the strain rate dependency is arbitrary fixed to be the same as the tensile tests one.

For the compression with electro-optical extensometer only the longitudinal strain is obtained, so two hypothesis have to be made. Firstly, the ϵ_{22} component has to be deduced from the longitudinal strain ϵ_{11} . This is achieved by considering damage phenomenon totally negligible in compression and ϵ_{22} is computed following the incompressibility hypothesis (eq 2.17):

$$\epsilon_{22} = -\frac{1}{2} \cdot \epsilon_{11} \quad (2.21)$$

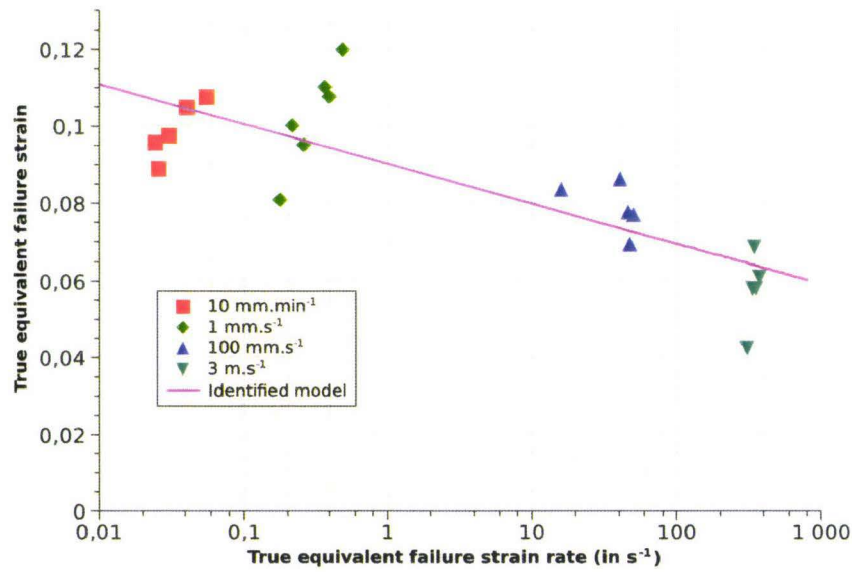


Figure 2.46: evolution of equivalent failure strain of notched tensile specimens in function of the equivalent strain rate.

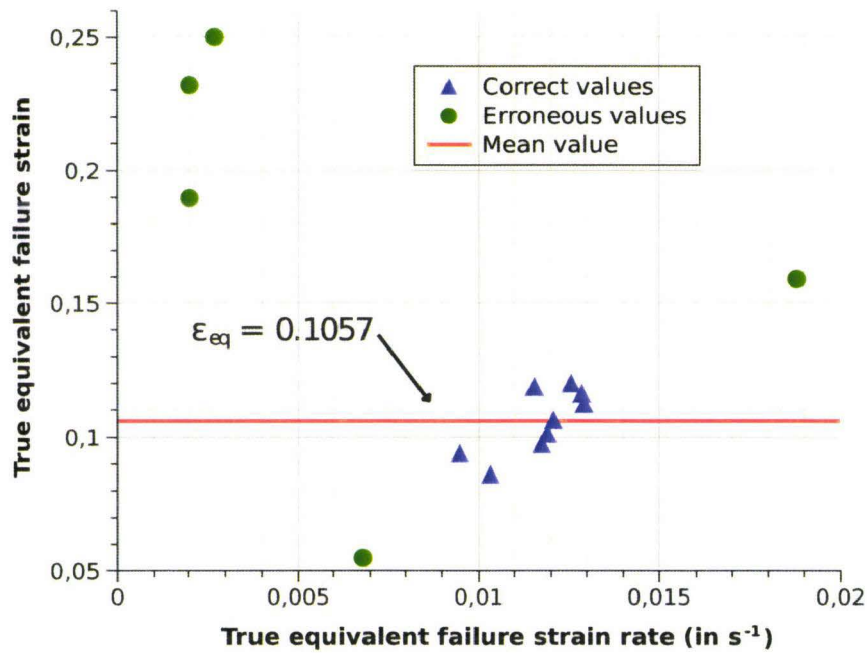


Figure 2.47: true equivalent failure strain on Iosipescu shear tests.

Secondly, an hypothesis is also made for the thickness behaviour, here again the incompressibility isotropy is used to compute ε_{33} . The true equivalent failure strain is obtained

by equation (2.9) and equation (2.21)

$$\bar{\bar{\varepsilon}} = \begin{bmatrix} \varepsilon_{11} & 0 & 0 \\ 0 & -\frac{1}{2} \cdot \varepsilon_{11} & 0 \\ 0 & 0 & -\left(\varepsilon_{11} - \frac{1}{2} \cdot \varepsilon_{11}\right) \end{bmatrix} \quad (2.22)$$

As for the classical and notched tensile tests, a real dependency to the strain rate is highlighted for the compressive tests (Figure 2.48).

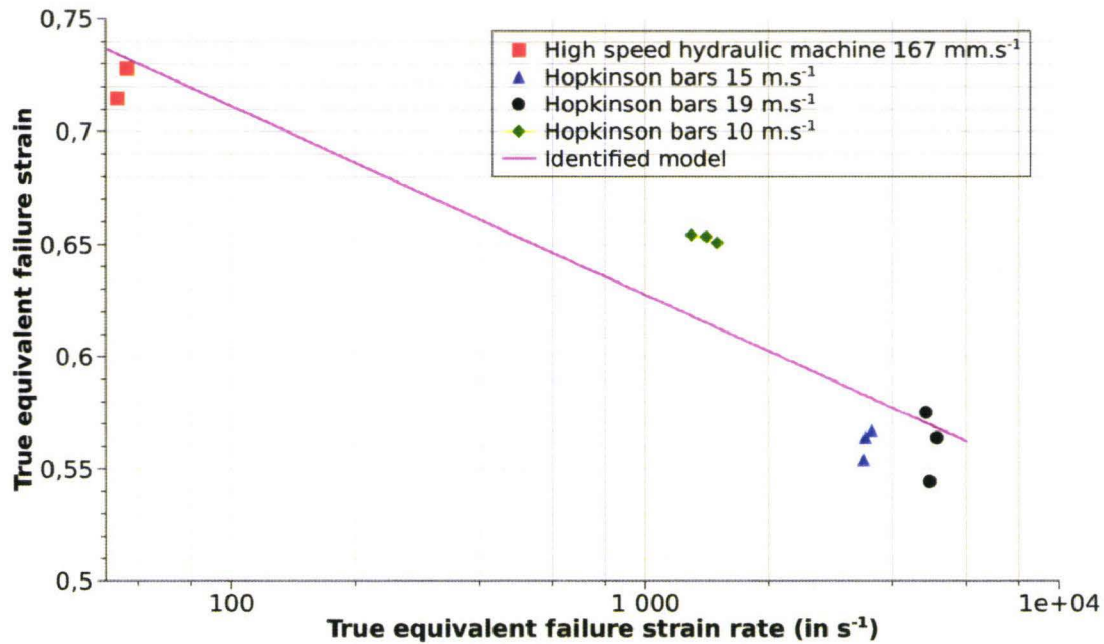


Figure 2.48: evolution of equivalent failure strain of compressive specimens in function of the equivalent strain rate.

As a conclusion of the experimental characterization of the failure of toughened epoxy adhesive, it is highlighted that a high dependency of the failure strain on the failure strain rate is present. It is also shown that the failure strain depends on the kinds of loadings and specimens (i.e. tensile, notched tensile, shear and compressive). This last dependency is in fact a dependency on the triaxiality stress ratio and its description will be given in the paragraph 2.4.3.

2.4 Behaviour and failure models identifications

2.4.1 Visco-elasticity model

By applying the works of Richeton et al [25] to the experimental results (Figure 2.31 (Figure 2.49)). Bi-logarithmic models have to be used to describe the compressive visco-elasticity. The tensile visco-elasticity with only two measurement points lead to a loga-

rithmic model (equation 2.23).

$$E(\dot{\varepsilon}) = a + b \cdot \ln\left(\frac{\dot{\varepsilon}}{\dot{\varepsilon}_0}\right) \quad (2.23)$$

where a and b are the visco-elasticity parameters and $\dot{\varepsilon}_0$ a parameter needed to obtain an adimensional logarithm.

As the tensile tests are performed with a 1 MPa curing pressure, the low strain rate model for 1 MPa compressive tests is extended from the 4 MPa one in order to obtain a complete description in terms of strain rate.

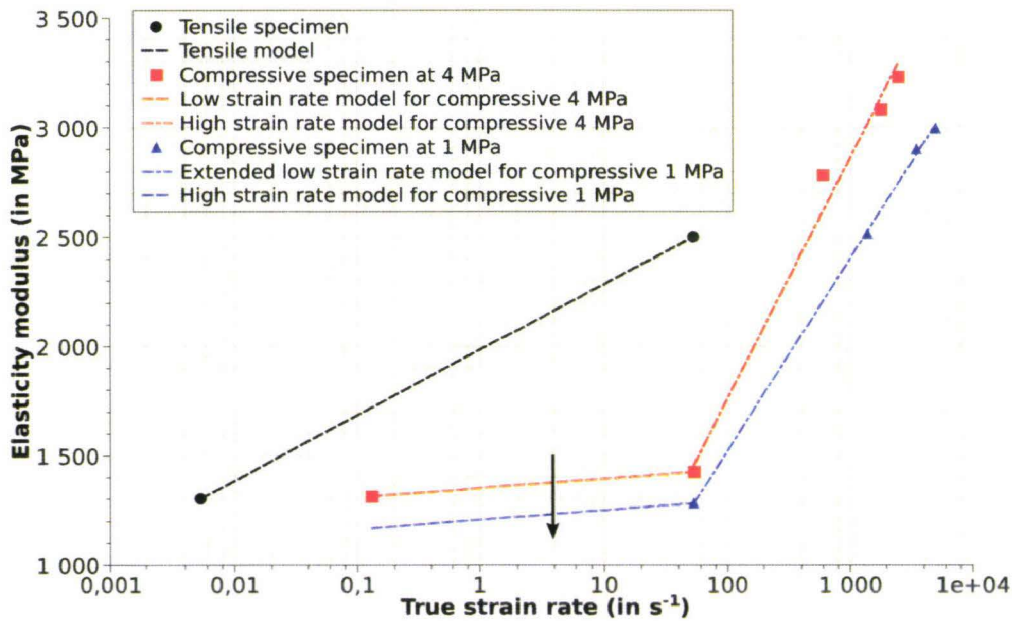


Figure 2.49: evolution of elasticity modulus in function of true strain rate.

2.4.2 Visco-plasticity model

For both tensile and shear tests, a modified G'Sell laws is identified following equation 3.6. The results of this identification is shown in Figure 2.50 and 2.51.

$$\sigma_{t/s} = \sigma_y + K \cdot (1 - e^{-w \cdot \varepsilon_p}) \cdot (1 + h_1 \cdot \varepsilon_p) \quad (2.24)$$

By computing the true behaviour laws from the $SE\dot{E}$ method with the transversal isotropy hypothesis, the damage is included into the behaviour law. If it could not be a problem to represent a pure tensile loading it will not be the same for a notched tensile for instance. To avoid this problem, the true behaviour laws are computed following the incompressibility hypothesis which lead to

$$\varepsilon_{11} + \varepsilon_{22} + \varepsilon_{33} = 0 \quad (2.25)$$

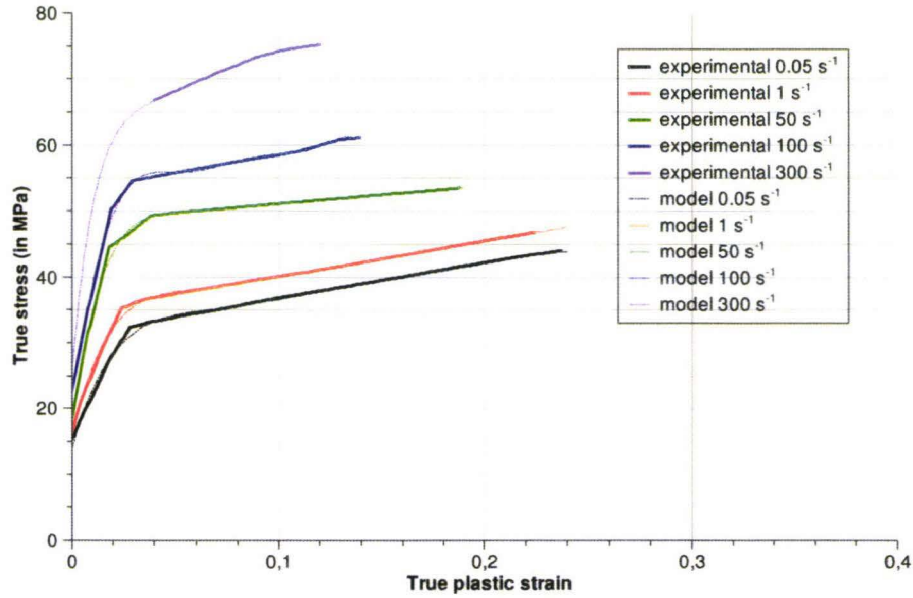


Figure 2.50: identification of tensile behaviour law.

In order to take the visco-plasticity into account classical multiplicative visco-plastic models can not be used [38] [39]. These classical models only realize an homothetic transformation of the behaviour than in experimental the shape of these laws also evolves. So as to describe this phenomenon, a behaviour law in which each parameter depends on the strain rate has to be used (equation 2.26). This kind of behaviour laws give a perfect description of behaviour law.

$$\sigma_{t/s} = \sigma_y(\dot{\varepsilon}) + K(\dot{\varepsilon}) \cdot (1 - e^{-w(\dot{\varepsilon}) \cdot \varepsilon_p}) \cdot (1 + h_1(\dot{\varepsilon}) \cdot \varepsilon_p) \quad (2.26)$$

where σ_y is the yield stress, K the global rigidity, w the hook parameter and h_1 the structural hardening parameter.

For the compressive behaviour laws another modified model is used to describe the experimental data. This behaviour model is based on a modification of the previous model (equation 2.26) and leads to:

$$\sigma_c = \sigma_y(\dot{\varepsilon}) + K(\dot{\varepsilon}) \cdot (1 - e^{-w(\dot{\varepsilon}) \cdot \varepsilon_p}) \cdot (1 + h_1(\dot{\varepsilon}) \cdot \varepsilon_p + h_2(\dot{\varepsilon}) \cdot \varepsilon_p^2 + h_3(\dot{\varepsilon}) \cdot \varepsilon_p^3) \quad (2.27)$$

where σ_y is the yield stress, K the global rigidity, w the hook parameter and h_1, h_2, h_3 the structural hardening parameters. Here again, the visco-plasticity is described by taking the strain rate dependance into account in order to give the best description of the behaviour laws as shown in Figure 2.52.

2.4.3 Volume variation and damage model

By linking the observation of plastic Poisson's ratio evolution (Figure 2.42) to a damage evolution by:

$$\nu_{pm} = (1 - d) \cdot \nu_p \quad (2.28)$$

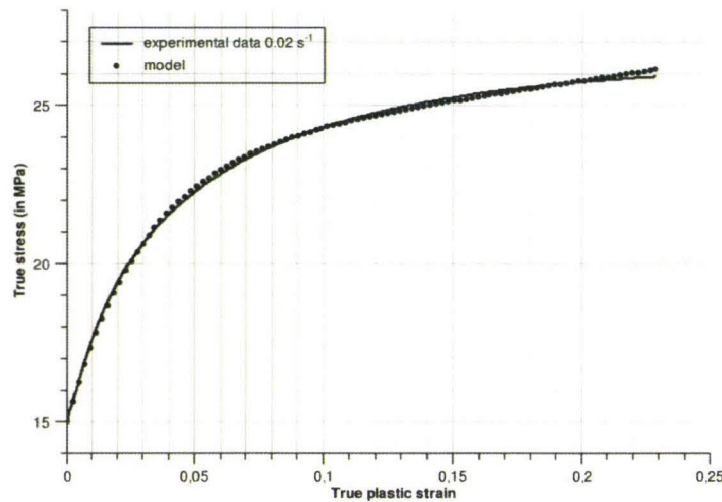


Figure 2.51: identification of shear behaviour law.

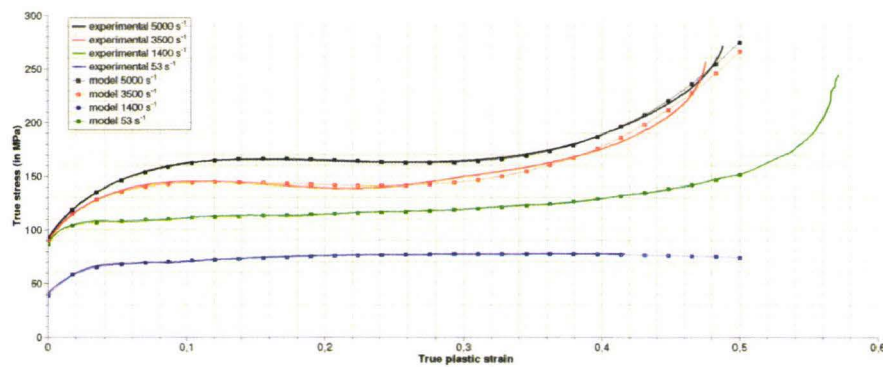


Figure 2.52: identification of compressive behaviour law.

where ν_{pm} is the measured plastic Poisson's ratio and ν_p the undamaged plastic Poisson's ratio, a damage variable d can be identified. By using curves illustrated in Figure 2.53 an original mathematical expression for the damage evolution is proposed

$$d = d_0 + K_d \cdot (1 - e^{-w_d \cdot \epsilon_p}). \quad (2.29)$$

By identifying the previous model (equation 2.29) on the different damage's evolution curves of Figure 2.53 a dependency on the triaxiality stress ratio is included into the model. So as to obtain a better description of the dependency on the triaxiality stress ratio, the hypothesis that in pure shear (i.e. $\eta = 0$) no damage evolution can occur is made. Following the identification shown in Figure 2.54, 2.55 and 2.56 a detailed damage is formulated following:

$$d = \eta \cdot (d_1 + d_2 \cdot \eta) + K_0 \cdot \eta \cdot (1 - e^{-\eta \cdot (w_1 + w_2 \cdot \eta) \cdot \epsilon_p}) \quad (2.30)$$

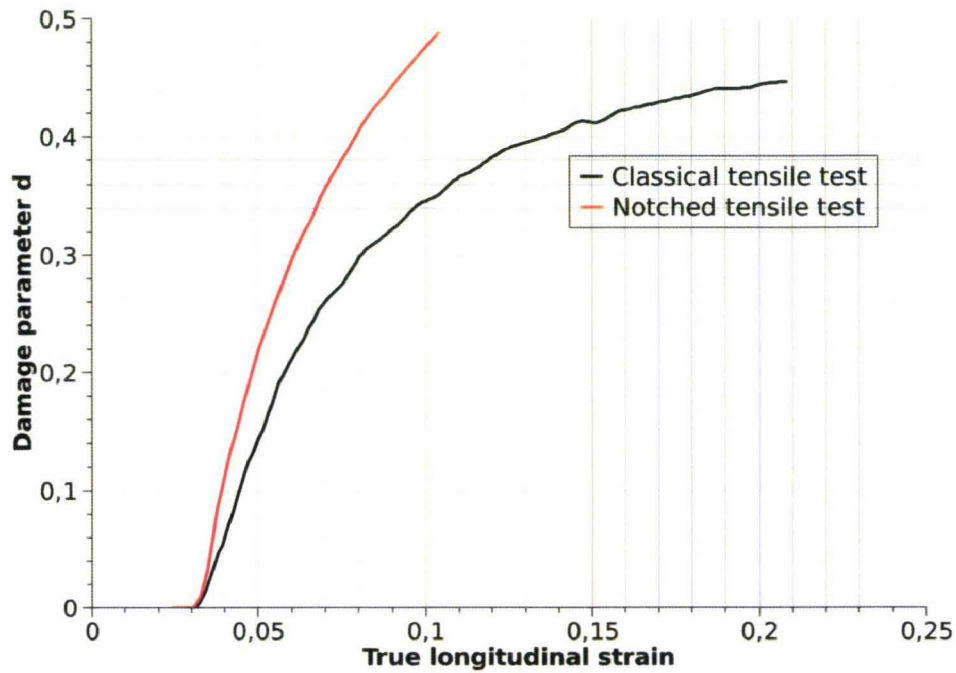


Figure 2.53: evolution of damage for two different triaxiality stress ratio.

where d_1 , d_2 , K_0 , w_1 and w_2 are parameters depending on the triaxiality stress ratio.

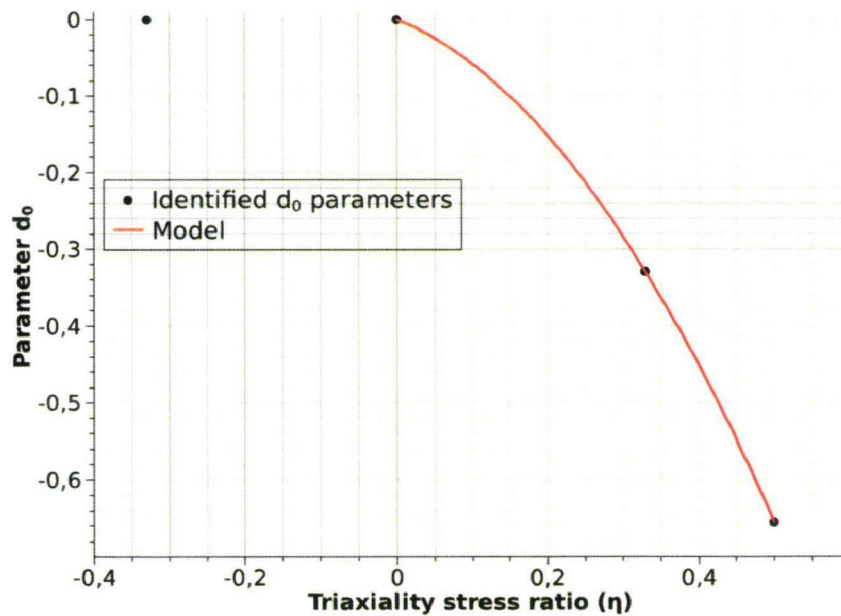


Figure 2.54: identification of d_0 damage evolution law parameter.

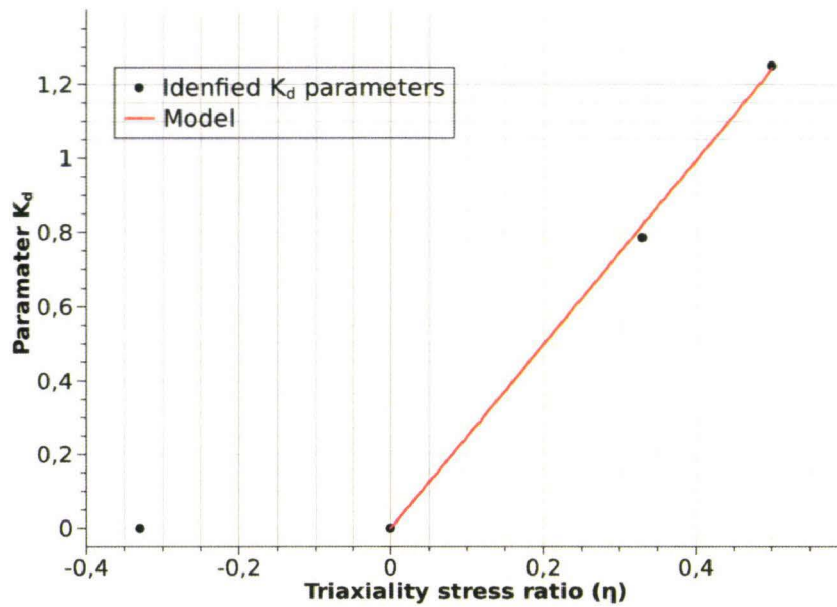


Figure 2.55: identification of K_d damage evolution law parameter.

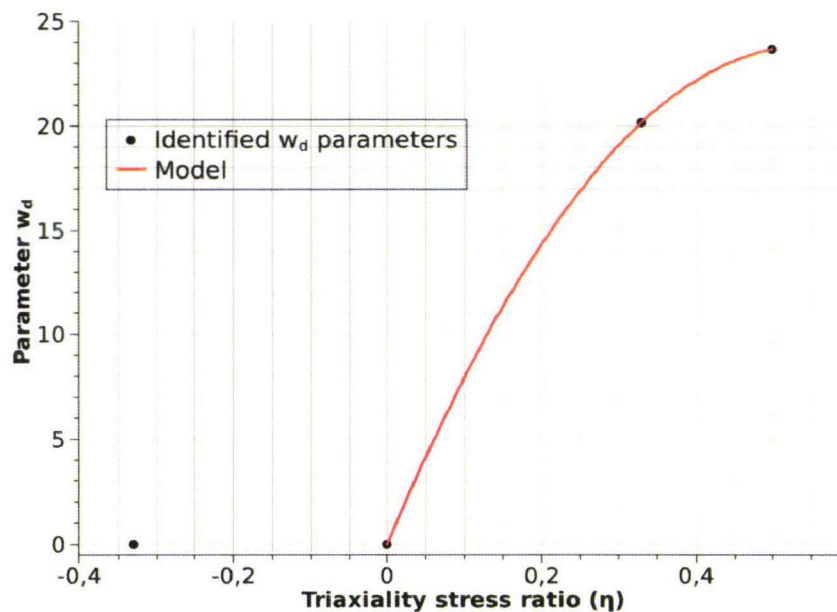


Figure 2.56: identification of w_d damage evolution law parameter.

2.4.4 Failure model

By linking the works of Johnson et al and Wierbizcki et al and following the strategy illustrates in Figure 2.57 a triaxiality stress ratio and strain rate dependent failure criterion is identified.

As shown in Figure 2.45, 2.46, 2.48, a logarithmic model can be used to describe the

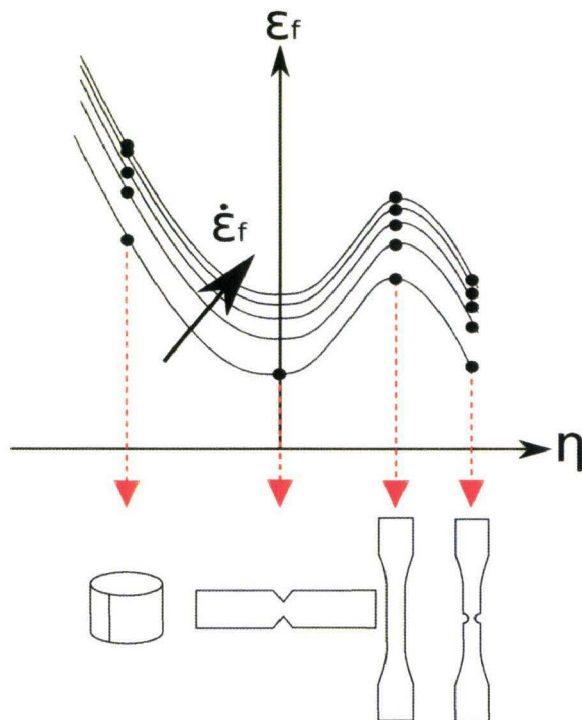


Figure 2.57: identification strategy for the failure criterion.

failure strain dependency on the strain rate:

$$\bar{\varepsilon}_f(\eta, \dot{\varepsilon}) = a_f(\eta) + b_f(\eta) \cdot \ln\left(\frac{\dot{\varepsilon}}{\dot{\varepsilon}_0}\right) \quad (2.31)$$

where a_f , b_f are functions which depend on the triaxiality stress ratio η and $\dot{\varepsilon}_0$ is used to obtain a non-dimensional parameter in the logarithm.

This procedure leads to the identification of the function a_f and b_f in function of the triaxiality stress ratio η . For the formulation of the a_f function, a simple polynomial approximation is made as Figure 2.58 illustrates. The strain rate dependency represented by the function b_f is identified following the data in Figure 2.59. The description of the viscous part of the criterion is not described by a monotonic function but by three functions as shown in Figure 2.59.

The final criterion model leads to

$$\bar{\varepsilon}_f(\eta, \dot{\varepsilon}) = (a_{\eta 0} + a_{\eta 1} \cdot \eta + a_{\eta 2} \cdot \eta^2 + a_{\eta 3} \cdot \eta^3) + (b_{\eta 1} + b_{\eta 2} \cdot \eta) \cdot \ln\left(\frac{\dot{\varepsilon}}{\dot{\varepsilon}_0}\right) \quad (2.32)$$

for $\eta \leq 0$

$$\bar{\varepsilon}_f(\eta, \dot{\varepsilon}) = (a_{\eta 0} + a_{\eta 1} \cdot \eta + a_{\eta 2} \cdot \eta^2 + a_{\eta 3} \cdot \eta^3) + b_{\eta 1} \cdot \ln\left(\frac{\dot{\varepsilon}}{\dot{\varepsilon}_0}\right) \quad (2.33)$$

for $0 \leq \eta \leq 0.33$

$$\bar{\varepsilon}_f(\eta, \dot{\varepsilon}) = (a_{\eta 0} + a_{\eta 1} \cdot \eta + a_{\eta 2} \cdot \eta^2 + a_{\eta 3} \cdot \eta^3) + (b_{\eta 3} + b_{\eta 4} \cdot \eta) \cdot \ln\left(\frac{\dot{\varepsilon}}{\dot{\varepsilon}_0}\right) \quad (2.34)$$

for $\eta \geq 0.33$

A 3D representation of the criterion is shown in Figure 2.60.

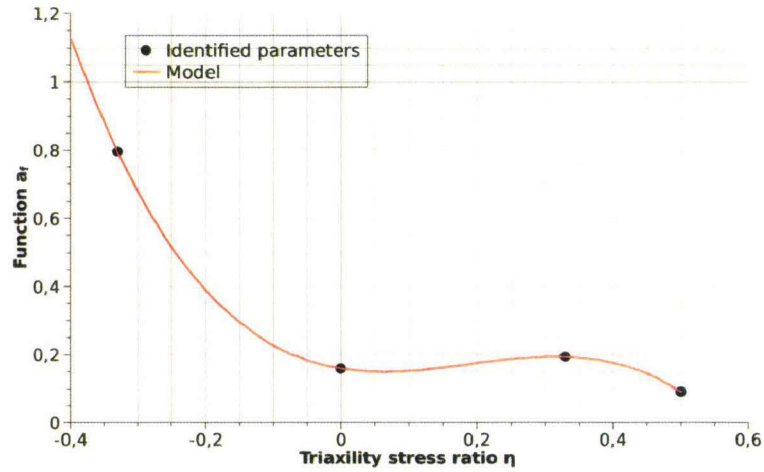


Figure 2.58: identification of the a_f function formulation.

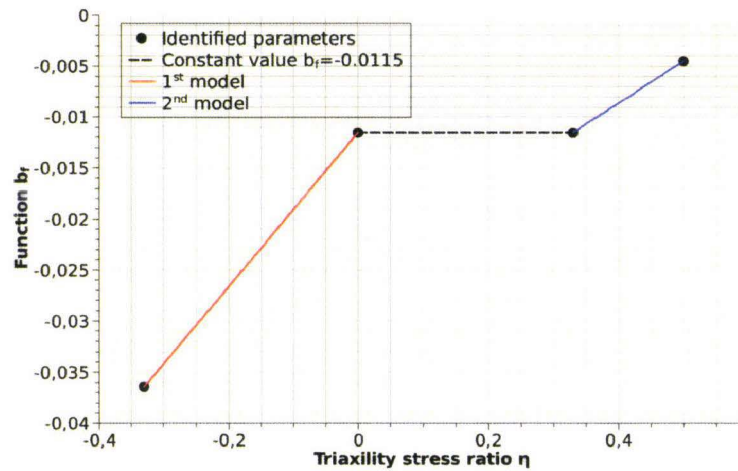


Figure 2.59: identification of the b_f function formulation.

As the failure model is identified on restricted range of triaxiality stress ratios and strain

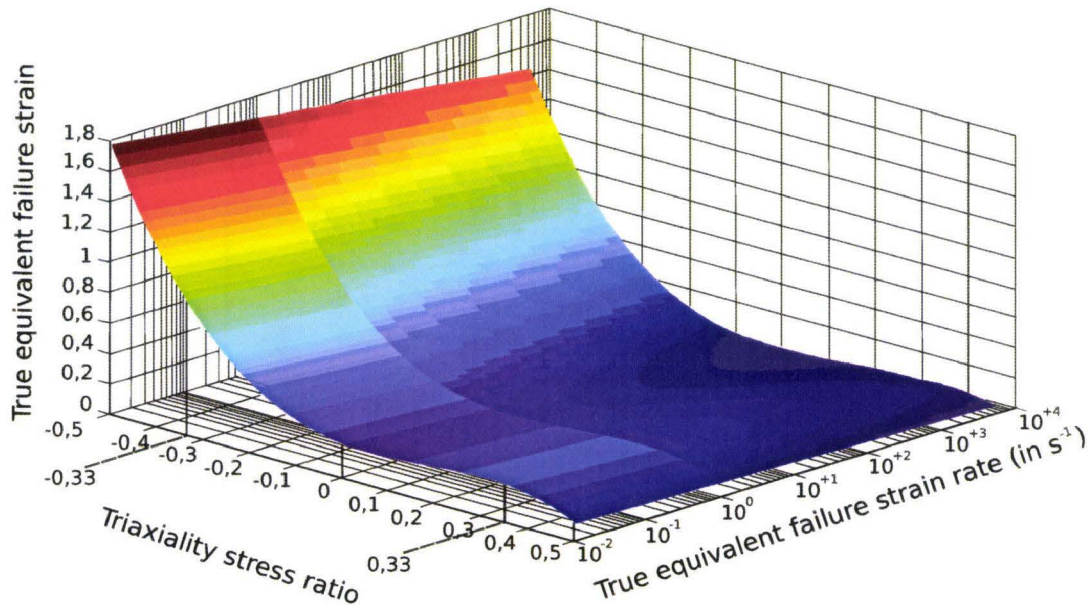


Figure 2.60: 3D representation of the new failure criterion.

rates, it is necessary to check the validity of this mathematical model for higher values of strain rates and triaxiality stress ratios. As shown in Figure 2.61, the previously identified criterion is not suitable for triaxiality stress ratios which are higher than 0.5 and lower than -0.5. For the extrapolation in terms of strain rates as Figure 2.62 shown, the predicted failure strain for tensile, notched tensile and shear are correct over 400 s^{-1} .

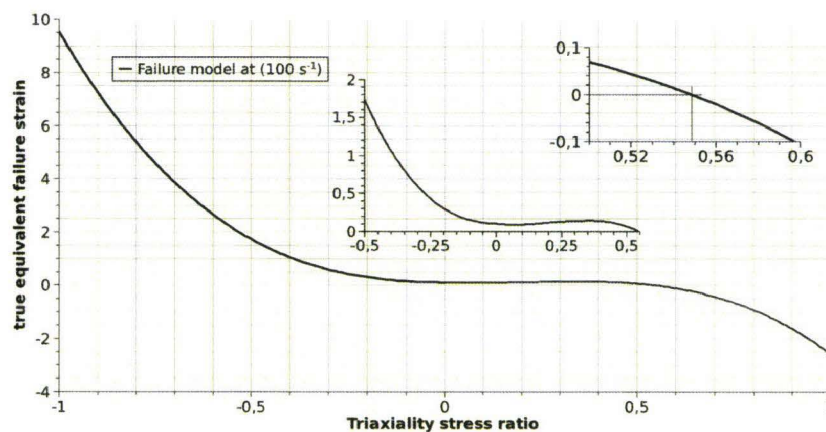


Figure 2.61: study of the failure criterion at constant strain rate on a wide range of triaxiality stress ratios.

In order to solve these problems, the failure criterion is locked in term of strain rates and triaxiality stress ratios as illustrated in Figures 2.63 and 2.65.

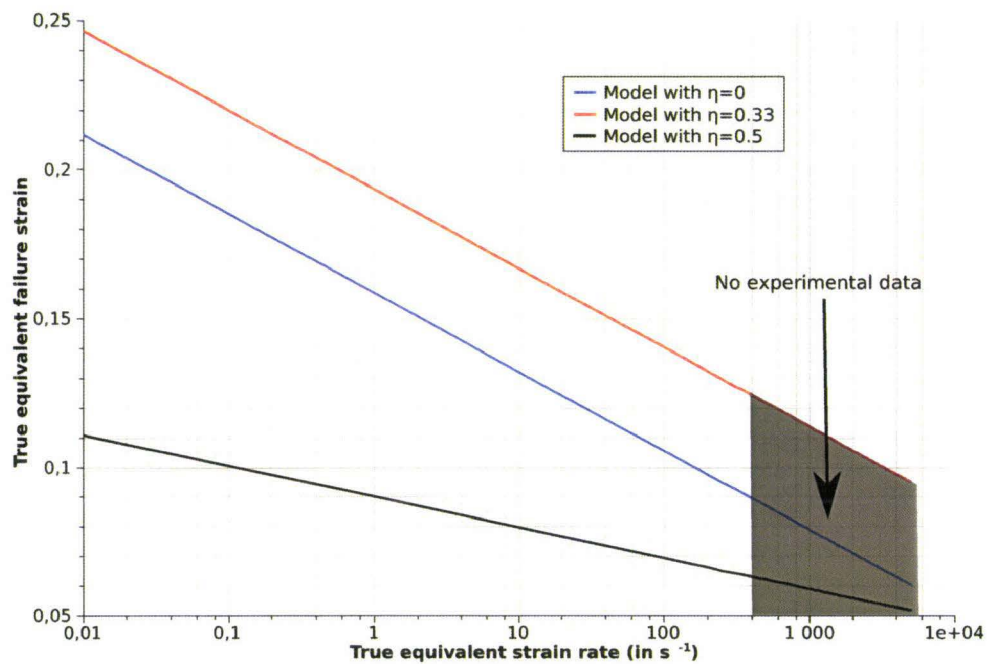


Figure 2.62: study of the failure criterion at constant triaxiality stress ratio on a wide range of strain rates.

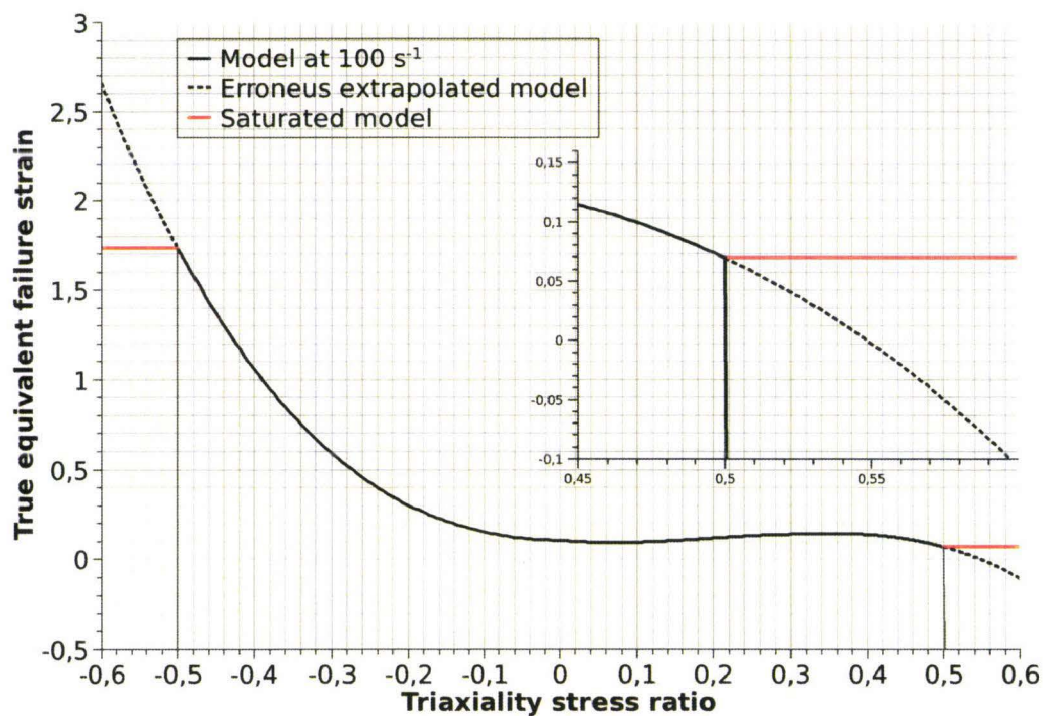


Figure 2.63: failure criterion saturation in term of triaxiality stress ratio.

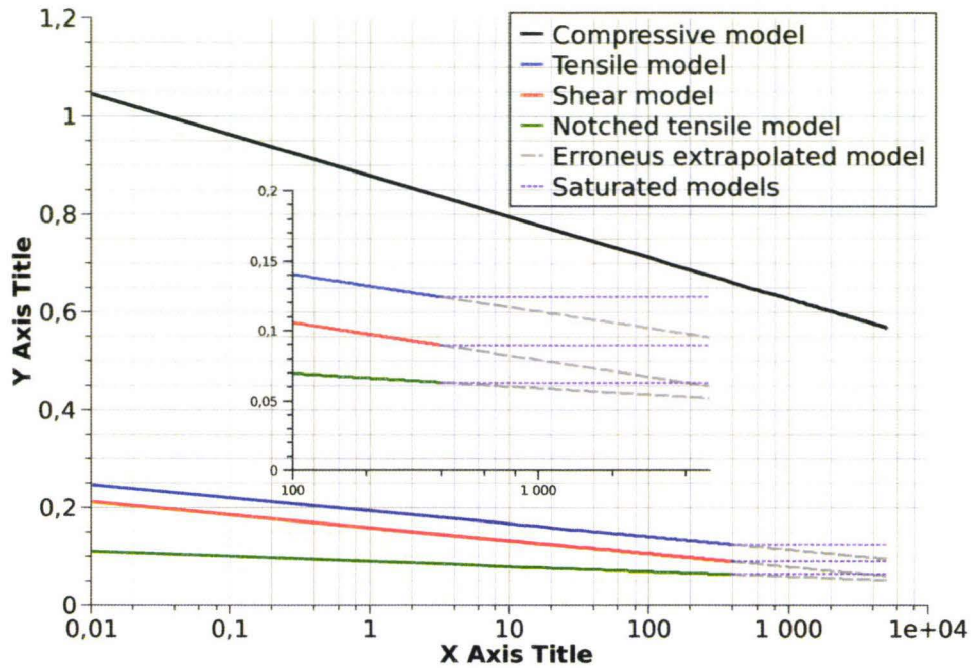


Figure 2.64: failure criterion saturation in term of strain rates.

2.5 Conclusions

This chapter brings a complete experimental description and models for a toughened epoxy adhesive from visco-elasticity to failure. This is achieved by using new measurement techniques like digital image correlation technique and different loading devices. Elasticity results proves that visco-elasticity phenomena can not be neglected. A difference between tensile and compressive elastic moduli is found and the influence of process parameters like curing pressure is shown. In terms of plasticity results, difference between tensile and compressive behaviour is clearly visible. Here again, the influence of curing pressure is highlighted. An original damage measurement is used and influence of the triaxiality stress ratio is proven. As for the elasticity and plasticity, the failure is found as strain rate dependent and the influence of triaxiality stress ratio is also studied.

These results leads to identification of mathematical models which will cover materials specificities. The visco-elasticity properties are tackled with a mono and bi logarithmic model which allow the elastic modulus to evolve with the strain rate. A new formulation of G'Sell behaviour model is determined for the plasticity in tension and compression. An original model for the damage evolution is proposed, it allows to take into account the influence of triaxiality stress ratio. Finally, a failure model is identified in function of the strain rate and the triaxiality stress ratio. These models have an impact on finite element modeling and a new implementation is presented in chapter 3.

2.6 Models parameters summary

	Model	$E = a + b \cdot \ln\left(\frac{\dot{\epsilon}}{\dot{\epsilon}_0}\right)$					$\dot{\epsilon}$ (in s^{-1})
Elasticity	Tension	a (in MPa)	1982	b (in MPa)	130		
	Compression		1204		19	< 53	
			-234		381	> 53	
Visco-plasticity	Model	$\sigma_t = \sigma_y + K \cdot (1 - e^{-w \cdot \epsilon_p}) \cdot (1 + h_1 \cdot \epsilon_p)$					
	Tension	σ_y (in MPa)	K (in MPa)	w	h_1		
		15	17	66	2.9	0.05	
		16	19	80	2.6	1	
		18	31	81	0.6	50	
		22	32	79	1.2	100	
	35	30	64	2.8	300		
	Model	$\sigma_c = \sigma_y + K \cdot (1 - e^{-w \cdot \epsilon_p}) \cdot (1 + h_1 \cdot \epsilon_p + h_2 \cdot \epsilon_p^2 + h_3 \cdot \epsilon_p^3)$					
	Compression	σ_y (in MPa)	K (in MPa)	w	h_1	h_2	h_3
		36	26	71	2.6	-2.8	-1.9
86		17	137	5.8	-23	43	
89		38	52	10.4	-64	118	
92	26	67	28.4	-140	213		
Damage	Model	$d = \eta \cdot (d_1 + d_2 \cdot \eta) + K_0 \cdot \eta \cdot (1 - e^{-\eta \cdot (w_1 + w_2 \cdot \eta) \cdot \epsilon_p})$					
		d_1	d_2	K_0	w_1	w_2	
		0.4	1.8	2.5	87	81	
Failure	Model	$\bar{\epsilon}_f(\eta, \dot{\epsilon}) = (a_{\eta 0} + a_{\eta 1} \cdot \eta + a_{\eta 2} \cdot \eta^2 + a_{\eta 3} \cdot \eta^3) + (b_{\eta 1} + b_{\eta 2} \cdot \eta) \cdot \ln\left(\frac{\dot{\epsilon}}{\dot{\epsilon}_0}\right)$					η
		$a_{\eta 0}$	$a_{\eta 1}$	$a_{\eta 2}$	$a_{\eta 3}$	$b_{\eta 1}$	$b_{\eta 2}$
		0.1	-0.2	3.9	-7.6	-0.01	0.07
						0	0.33
				-0.02	0.04		

Figure 2.65: summary of mesoscopic model parameters.

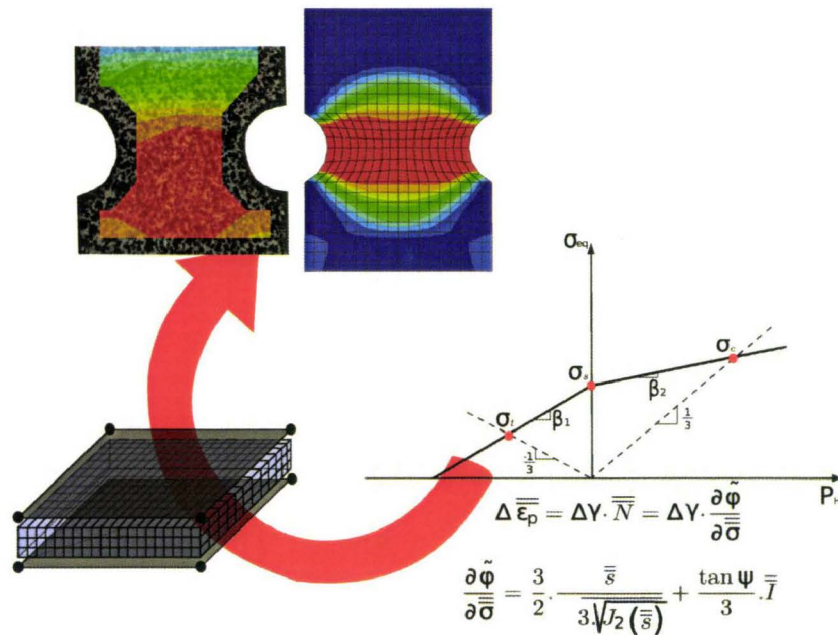
Mesoscopic material behaviour model

Contents

3.1	Literature study and proposed models	52
3.2	General description of the material behaviour model	56
3.3	Description of elastic prediction	57
3.4	Yield criterion	59
3.5	Yield return algorithm	60
3.6	Results update	66
3.7	Summary of the mesoscopic behaviour model implementation	67
3.8	Conclusions	68

Resume

The aim of this chapter is to present the finite element implementation of the mesoscopic material behaviour model. It brings the complete development of visco-elasticity, visco-plasticity equations and non-associative plasticity.



3.1 Literature study and proposed models

Different techniques are used in the literature to model the bonded joints at the mesoscopic scale in finite element simulations. 2D or 3D models are used in the literature, these models are generally used to study special geometries of bonded joints or to investigate local failure initiations. 2D models are generally tackled by plane strain elements [3] [7]. Although these models allow a fine description of stresses and strains through the thickness of bonded joints they can not take into account deformation of adherents as illustrated in Figure 3.1. These 2D models are also unsuitable for the modeling of complex structures.

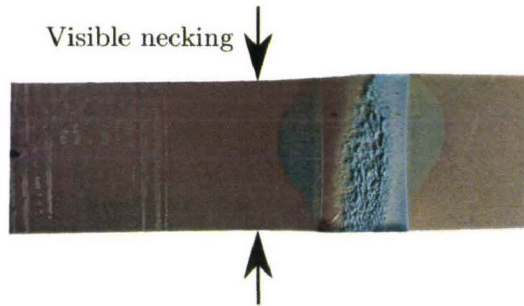


Figure 3.1: example of necking in a steel single lap joint test.

In opposite of 2D models in which link between adherents and adhesives is performed by a simple merge of coincident nodes, the link between adherents and adhesives is generally more complex in 3D models. Of course, in a fully volumic model as illustrated in Figure 3.2a same merging technique as 2D models can be used but in the particular case of automotive crashworthiness, volumic models of steel sheet are not representative. In the case of shell modeling of steel sheets, two different point of view are used to numerically bond the adhesive to the steel sheets as illustrated in Figure 3.2b and c. The first one illustrates in Figure 3.2b would lead to realize a merge between steel shell and adhesive volumic nodes [26], this approach is only realistic if an offset is applied on the neutral surface of the shell elements. In complex modeling these offsets are not realizable and this kind of modelling brings high problems in terms of physical representation. In the second shell model illustrates in Figure 3.2c, an offset equal to half of the shell thickness is applied between shell neutral plane and volumic adhesive element. This kind of modeling respects the physical aspect of bonded joints but need advanced numerical techniques to keep the offset during all the finite element simulation.

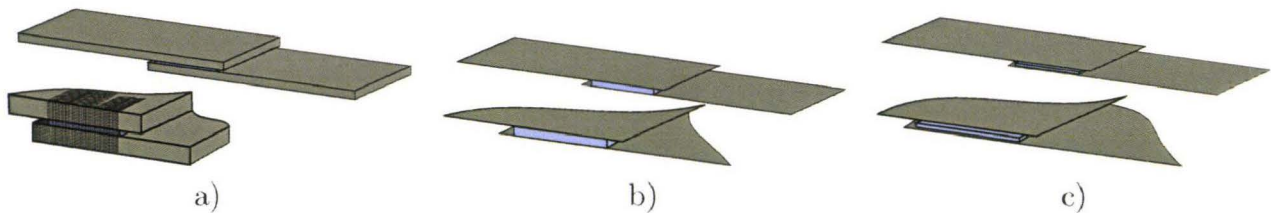


Figure 3.2: example of necking in a steel single lap joint test.

Many techniques are available to solve this problem:

- a tie constraint which force a slave and master surface to be at given distance from each other,
- a multi point constraint which couples the freedom degree of a slave node to them of a master one,
- a rigid beam which link two neighbour nodes.

In this thesis the tie constraint is chosen to combine the real physical aspect of bonded joints to the need of shell modeling of steel sheets. In all these models, the different kinds of failure mode of adhesive (Figure 3.3) can not be predicted. Only the cohesive and the superficial cohesive failure can be take into account in these models. The adhesive failure is discarded in this thesis according to the adhesive producers which considers that this failure is the results of a wrong bonding.

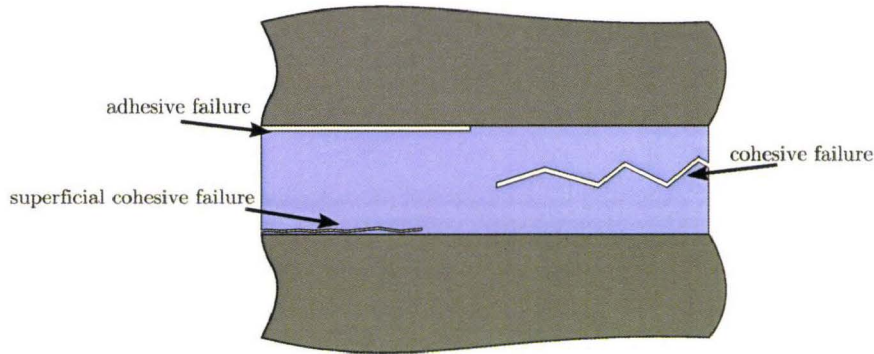


Figure 3.3: different failure modes in a bonded joint.

In addition to these geometrical considerations, the literature offers a various material models to simulate the behaviour and failure of bonded joints. Due to the lack of visco-elastic models, the visco-elasticity highlighted in Chapter 2 is not handle in the literature. Some visco-elastic models are implemented into FE code [40] but can not be combined with plasticity models. In terms of yield criterion, it is shown in Figure 3.4 that classical yield criterion like von Mises (3.1) or Drucker Prager model (3.2) [6] can not described perfectly the hydrostatic pressure dependency as follows.

$$\phi = \sigma_{eq} - \sigma_y \quad (3.1)$$

where σ_{eq} is the von Mises equivalent stress and σ_y is the yield stress and

$$\phi = \sigma_{eq} + \eta \cdot P_H - \sigma_y \quad (3.2)$$

where σ_{eq} is the von Mises equivalent stress, P_H the hydrostatic pressure, η the sensitivity parameter to the hydrostatic pressure and σ_y is the yield stress.

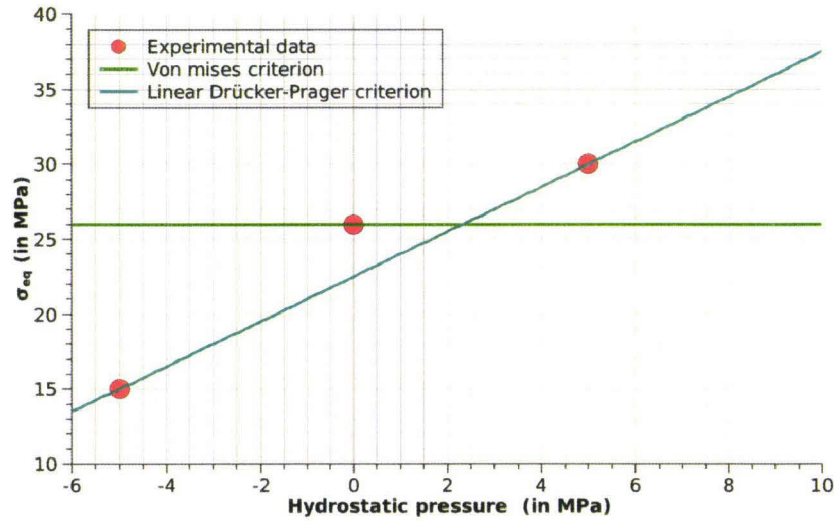


Figure 3.4: evaluation of classical yield criterion.

In the literature, some advanced yield criterion are also present. The Ragavanah model named exponent Drucker Prager [6] [40](eq 3.3) (in Abaqus) and SAMP model (implemented in LS-Dyna) [41] (eq 3.4) provide a non-linear description of the yield criterion in terms of hydrostatic pressure. The yield criterion is described by:

$$\phi = a \cdot \sigma_{eq}^2 - P - P_T \quad (3.3)$$

where a and P_T are material parameters in the case of the Ragavanah model and by:

$$\phi = \sigma_{eq}^2 - A_0 - A_1 \cdot P - A_2 \cdot P^2 \quad (3.4)$$

where A_0 , A_1 and A_2 are computed as following:

$$A_0 = 3 \cdot \sigma_s^2 \quad A_1 = 9 \cdot \sigma_s^2 \cdot \left(\frac{\sigma_c - \sigma_t}{\sigma_c \cdot \sigma_t} \right) \quad A_2 = 9 \cdot \left(\frac{\sigma_c \cdot \sigma_t}{\sigma_c \cdot \sigma_t - 3 \cdot \sigma_s^2} \right) \quad (3.5)$$

where σ_s , σ_c and σ_t are the yield stress in shear, compression and tension respectively in the case of the SAMP model.

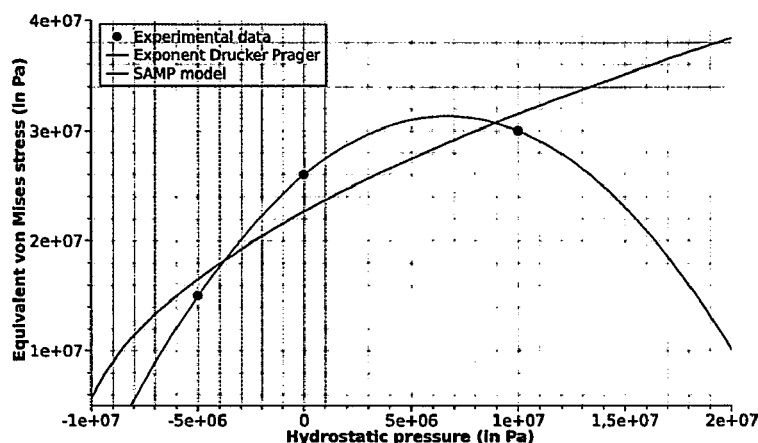


Figure 3.5: difference between exponent Drucker Prager and SAMP model.

The main difference between exponent Drucker Prager and SAMP model is focused on the bi-axial tension and compression yield stress (Figure 3.5). But without informations on the bi-axial tension and compression yield stresses of the investigated toughened epoxy adhesive it is not possible to conclude on the best criterion.

In the literature, the plastic behaviour is generally tackled with tabulated behaviour law to simulate a visco-plastic (Figure 3.6).

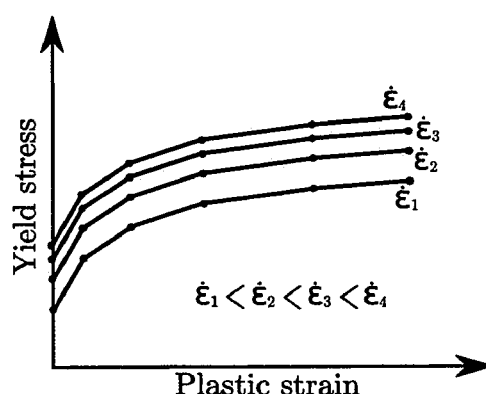


Figure 3.6: illustration of tabulated visco-plastic behaviour law.

Non-isochoric plasticity is commonly modeled with non-associative plasticity [6]. The theoretical aspects of this approach are detailed in paragraph 3.5.1. Failure in bonded joints are generally not taken into account in literature. In terms of failure criterion, the most common failure models present in FE codes are exposed in Chapter 2.

In this work, the visco-elasticity is tackled using model previously identified (eq 2.23). The yield criterion is modeled by a bi-linear Drucker Prager model due to the lack of data in bi-axial tension and compression. The visco-plasticity is described by the following models :

$$\sigma_t = \sigma_y(\dot{\epsilon}) + K(\dot{\epsilon}) \cdot (1 - e^{-w(\dot{\epsilon}) \cdot \epsilon_p}) \cdot (1 + h_1(\dot{\epsilon}) \cdot \epsilon_p) \quad (3.6)$$

for the tension behaviour and:

$$\sigma_c = \sigma_y(\dot{\epsilon}) + K(\dot{\epsilon}) \cdot (1 - e^{-w(\dot{\epsilon}) \cdot \epsilon_p}) \cdot (1 + h_1(\dot{\epsilon}) \cdot \epsilon_p + h_2(\dot{\epsilon}) \cdot \epsilon_p^2 + h_3(\dot{\epsilon}) \cdot \epsilon_p^3) \quad (3.7)$$

for the compressive behaviour.

Volume variation is tackled with a non-associative approach and damage evolution by :

$$d = \eta \cdot (d_1 + d_2 \cdot \eta) + K_0 \cdot \eta \cdot (1 - e^{-\eta \cdot (w_1 + w_2 \cdot \eta) \cdot \epsilon_p}) \quad (3.8)$$

Finally the failure is predicted by :

$$\bar{\epsilon}_f(\eta, \dot{\epsilon}) = (a_{\eta 0} + a_{\eta 1} \cdot \eta + a_{\eta 2} \cdot \eta^2 + a_{\eta 3} \cdot \eta^3) + (b_{\eta 1} + b_{\eta 2} \cdot \eta) \cdot \ln\left(\frac{\dot{\bar{\epsilon}}}{\bar{\epsilon}_0}\right) \quad (3.9)$$

for $\eta \leq 0$

$$\bar{\epsilon}_f(\eta, \dot{\epsilon}) = (a_{\eta 0} + a_{\eta 1} \cdot \eta + a_{\eta 2} \cdot \eta^2 + a_{\eta 3} \cdot \eta^3) + b_{\eta 1} \cdot \ln\left(\frac{\dot{\bar{\epsilon}}}{\bar{\epsilon}_0}\right) \quad (3.10)$$

for $0 \leq \eta \leq 0.33$

$$\bar{\epsilon}_f(\eta, \dot{\epsilon}) = (a_{\eta 0} + a_{\eta 1} \cdot \eta + a_{\eta 2} \cdot \eta^2 + a_{\eta 3} \cdot \eta^3) + (b_{\eta 3} + b_{\eta 4} \cdot \eta) \cdot \ln\left(\frac{\dot{\bar{\epsilon}}}{\bar{\epsilon}_0}\right) \quad (3.11)$$

for $\eta \geq 0.33$

3.2 General description of the material behaviour model

The implementation of the mesoscopic finite element model follows the classical steps of a material subroutine. The mesoscopic model is implemented through a VUMAT subroutine into Abaqus explicit. This kind of subroutine gives a strain increment tensor in the local basis of the element and requires the export of the stress tensor also in the local basis.

Firstly an elastic prediction is realized using the strain increment tensor following by a yield criterion check. Until the yield criterion is not satisfied the material is assumed to be fully elastic. If the yield criterion is satisfied then a yield return algorithm is applied and the stress tensor is updated [42] (Figure 3.7 a).

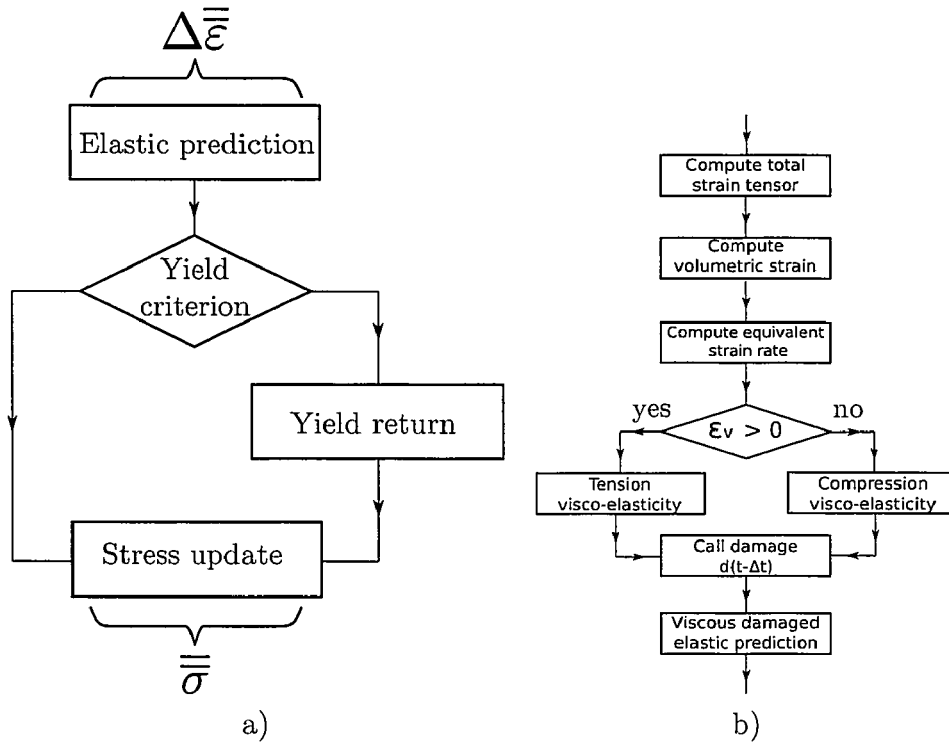


Figure 3.7: a) general overview of the algorithm and b) description of elasticity algorithm

3.3 Description of elastic prediction

The elastic prediction is realized like a viscous-damaged elastic prediction following the algorithm illustrated in Figure 3.7 b. As the visco-elasticity is taken into account an equivalent strain rate is needed (Paragraph 3.3.1), moreover the visco-elasticity models are different in tension and compression so a numerical test has to be done. This test is based on the sign of the volumetric strain here called ε_V defined by 3.17. The equivalent strain rate is computed and the tension/compression test is done then the damage variable from the previous step is called and the viscous-damaged elastic prediction is performed (paragraph 3.3.3).

3.3.1 Strain rate computation

The equivalent strain rate needed for the visco-elastic prediction is computed following:

$$\dot{\bar{\varepsilon}} = \sqrt{\frac{2}{3} \dot{\bar{\varepsilon}} : \dot{\bar{\varepsilon}}} \quad (3.12)$$

where $\dot{\bar{\varepsilon}}$ is the strain rate tensor.

As the strain rate tensor is not computed by the FE software to the VUMAT subroutine,

the strain rate tensor is computed from the strain increment tensor $\Delta\bar{\varepsilon}$ following

$$\dot{\bar{\varepsilon}} = \frac{\partial\bar{\varepsilon}}{\partial t} \approx \begin{bmatrix} \frac{\Delta\varepsilon_{11}}{\Delta t} & \frac{\Delta\varepsilon_{12}}{\Delta t} & \frac{\Delta\varepsilon_{13}}{\Delta t} \\ \frac{\Delta\varepsilon_{12}}{\Delta t} & \frac{\Delta\varepsilon_{22}}{\Delta t} & \frac{\Delta\varepsilon_{23}}{\Delta t} \\ \frac{\Delta\varepsilon_{13}}{\Delta t} & \frac{\Delta\varepsilon_{23}}{\Delta t} & \frac{\Delta\varepsilon_{33}}{\Delta t} \end{bmatrix} = \frac{\Delta\bar{\varepsilon}}{\Delta t} \quad (3.13)$$

The equivalent strain rate is then computed following

$$\dot{\bar{\varepsilon}} = \sqrt{\frac{2}{3} \cdot \frac{\Delta\bar{\varepsilon}}{\Delta t} : \frac{\Delta\bar{\varepsilon}}{\Delta t}} = \frac{\sqrt{\frac{2}{3} \cdot \Delta\bar{\varepsilon} : \Delta\bar{\varepsilon}}}{\Delta t} = \frac{\Delta\bar{\varepsilon}}{\Delta t}. \quad (3.14)$$

As this kind of computation leads to noisy results, a numerical filter is used (3.15). This filter is extracted from PAMCRASH finite element software [43] and level of filtering is adapted by changing the value of parameter α (typically chosen equal to 0.3).

$$\dot{\bar{\varepsilon}}_{filtered} = \alpha \cdot \dot{\bar{\varepsilon}}(t) + (1 - \alpha) \cdot \dot{\bar{\varepsilon}}(t - \Delta t) \quad (3.15)$$

3.3.2 Total strains and volumic strain computation

In order to realize a damaged-viscous elastic prediction, the total strain tensor and the volumic strain have to be computed. For that, the strain increment tensor given by the FE software is added to the converged elastic strain from the previous time step

$$\bar{\varepsilon} = \bar{\varepsilon}_{e(t-\Delta t)} + \Delta\bar{\varepsilon} \quad (3.16)$$

where $\bar{\varepsilon}_{e(t-\Delta t)}$ is the converged elastic strain tensor from the previous time step. Then the volumic strain is computed for the previous tensor

$$\varepsilon_V = \sum_{i=1}^3 \varepsilon_{ii} \quad (3.17)$$

3.3.3 Damaged-viscous elastic prediction

In order to realize a damaged-viscous elastic prediction, the viscous-modulus has to be computed following equation 2.23. The choice of the compressive or tensile model is realized by testing the sign of the volumic strain (equation 3.17). For the special case of pure shear loading the visco-elastic behaviour is assumed to be the same as tensile due experimental observations. Following the previous prescriptions, the damaged viscous elastic prediction is realized with

$$s_{ii}^{TRIAL} = \frac{E \cdot (1 - d)}{1 + \nu} \cdot (\varepsilon_{ii} - \frac{\varepsilon_V}{3}) \quad s_{ij}^{TRIAL} = \frac{E \cdot (1 - d)}{2 \cdot (1 + \nu)} \cdot \varepsilon_{ij} \quad (3.18)$$

$$P_H^{TRIAL} = -\frac{E \cdot (1 - d)}{3 \cdot (1 - 2 \cdot \nu)} \cdot \varepsilon_V \quad (3.19)$$

where d is the damage variable of the previous time step, E the viscous elastic modulus and ν the Poisson's ratio. In addition the equivalent stress is computed following the von Mises theory:

$$\sigma_{eq}^{TRIAL} = \sqrt{3 \cdot J_2 \left(\frac{\bar{\varepsilon}}{3}^{TRIAL} \right)} \quad (3.20)$$

where J_2 is the second invariant of the deviatoric stress tensor defined by

$$J_2 \left(\overline{\underline{s}}^{TRIAL} \right) = \frac{1}{2} \overline{\underline{s}}^{TRIAL} : \overline{\underline{s}}^{TRIAL} \quad (3.21)$$

3.3.4 Time step consideration

A special consideration is devoted to the time step needed for the finite element simulation. In Abaqus explicit, the time step of the FE simulation is computed from a fictitious time step. According to 1.1 the time step calculation depends on the elastic modulus so for a visco-elastic model in which the elastic modulus evolves with the strain rate, the highest elastic modulus has to be given for this calculation. This special consideration is done to ensure the stability of the FE simulation.

3.4 Yield criterion

A yield criterion is used to determine if the plasticity has to take place. To model the yield difference in tension, shear and compression a bi-linear Drucker-Prager criterion is used. As this criterion is composed of two linear Drucker-Prager, a tension/compression test has to be carried out using the volumetric strain (Figure 3.8).

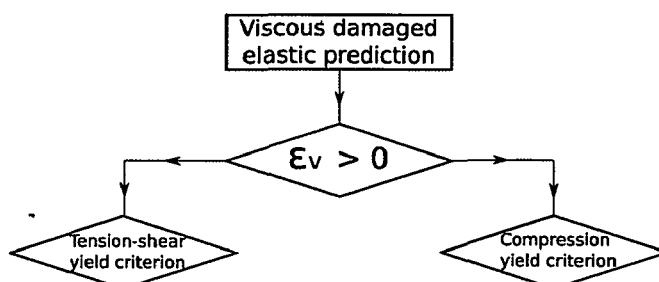


Figure 3.8: yield criterion algorithm.

3.4.1 Definition of the yield criterion formulation

The bi-linear Drucker Prager is formulated following equations (3.22) and (3.23). This yield criterion is illustrated in Figure 3.9.

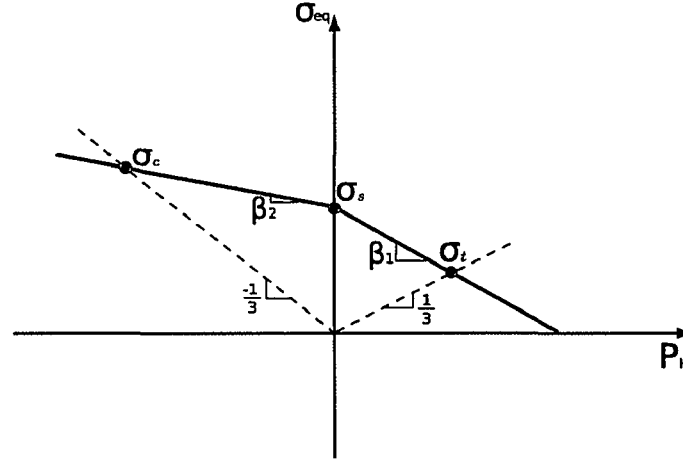


Figure 3.9: illustration of the double Drucker Prager yield criterion.

where σ_t , σ_c and σ_s are yield stresses in tension, compression and shear respectively, β_1 and β_2 are the friction angles related to yield stress difference in tension, shear and compression.

The mathematical formulation of the criterion is explained as below:

$$\phi = \sigma_{eq} + \tan(\beta_1) \cdot P_H - \left(1 + \frac{\tan(\beta_1)}{3}\right) \cdot (1-d) \cdot \sigma_t \quad (3.22)$$

$$\phi = \sigma_{eq} + \tan(\beta_2) \cdot P_H - \left(1 - \frac{\tan(\beta_2)}{3}\right) \cdot (1-d) \cdot \sigma_c \quad (3.23)$$

3.4.2 Selection of yield criterion

The selection of yield criterion is realized following the same technique as for the visco-elastic model selection. The yield criterion is then selected with the sign of the volumic strain. As for the visco-elastic prediction in case of pure shear the yield criterion defined by β_1 (3.22) is chosen.

3.5 Yield return algorithm

If the yield criterion is not satisfied then a yield return is needed to determine the plastic strains which occur in the time step. For the case of tensile loading, the non-associative approach is chosen (paragraph 3.5.2), a short description of the foundations of this approach is given in paragraph 3.5.1. In the particular case of the shear and compressive loadings, the classical von Mises plasticity is used due to the hypothesis that no damage phenomena can occur (paragraph 3.5.3).

3.5.1 General overview of associative and non-associative plasticity

The non-associative plasticity is used to model non-isochoric plasticity. The volume variation during plasticity is represented by a plastic strain rate tensor which has a dependency to the hydrostatic pressure. The plastic strain rate tensor is obtained by

$$\Delta \overline{\overline{\varepsilon}}_p = \Delta \gamma \cdot \overline{\overline{N}} \quad (3.24)$$

where $\Delta \gamma$ is the plastic multiplier and $\overline{\overline{N}}$ the return vector.

For the particular case of a von Mises plasticity, an example of an associative and non-associative plasticity is shown in Figure 3.10. In associative plasticity, the return vector $\overline{\overline{N}}$ is obtained by differentiation of the yield criterion as equation 3.25 shows. In non-associative plasticity, the return vector is obtained by differentiation of a plastic potential $\tilde{\phi}$ as equation 3.25 shows. For the particular case of the von Mises plasticity, the plastic potential has to be chosen with a hydrostatic pressure dependency so as to obtain a non normal return vector.

$$\overline{\overline{N}}_{\text{associative}} = \frac{\partial \phi}{\partial \overline{\overline{\sigma}}} \quad \overline{\overline{N}}_{\text{nonassociative}} = \frac{\partial \tilde{\phi}}{\partial \overline{\overline{\sigma}}} \quad (3.25)$$

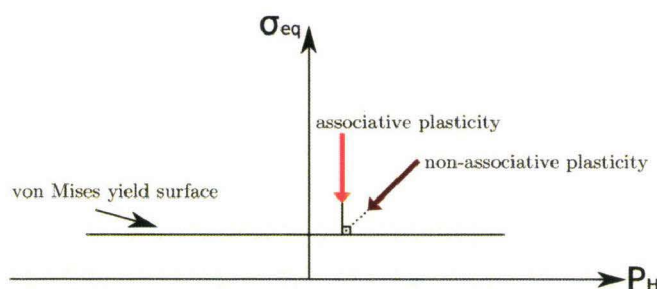


Figure 3.10: illustration of the difference between a non-associative and associative plasticity in the von Mises case.

3.5.2 Description of the plastic potential and the yield return vectors used for the tensile loadings

In order to model the non-isochoric behaviour of the investigated toughened epoxy adhesive, the following plastic potential is chosen

$$\tilde{\phi} = \sigma_{eq}^{TRIAL} + \tan \psi \cdot P_H \quad (3.26)$$

where σ_{eq}^{TRIAL} is defined by 3.20 and ψ is the dilatation angle defined by:

$$\tan \psi = \frac{3 \cdot (1 - 2 \cdot (1 - d) \cdot \nu_p)}{2 \cdot (1 + (1 - d) \cdot \nu_p)} \quad (3.27)$$

where ν_p is plastic Poisson's ratio and d the damage variable of the previous step.

Here the damage variable is included in the dilatation angle so as to translate the variation of plastic Poisson's ratio observed during the experiments.

A 3D representation of the plastic potential is given in Figure 3.11.

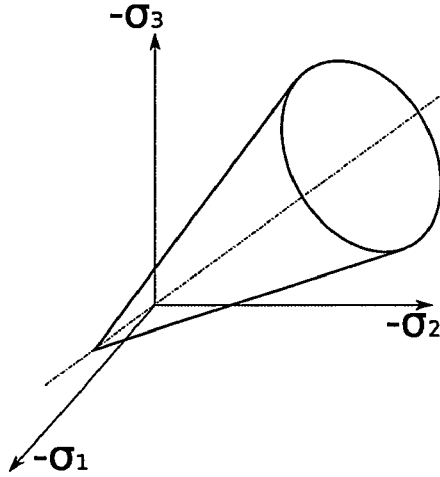


Figure 3.11: 3D representation of the plastic potential.

As the return vector is obtained by differentiation of the plastic potential a special attention has to be made between smooth and apex cone return. The smooth return vector is obtained by

$$\bar{\bar{N}}_d = \frac{3}{2} \cdot \frac{\bar{\bar{s}}}{\sqrt{3 \cdot J_2(\bar{\bar{s}})}} \quad (3.28)$$

$$\bar{\bar{N}}_v = \frac{\tan \psi}{3} \cdot \bar{\bar{I}} \quad (3.29)$$

where $\bar{\bar{N}}_d$ and $\bar{\bar{N}}_v$ are the counterpart of deviatoric stress and hydrostatic pressure to the return vector respectively.

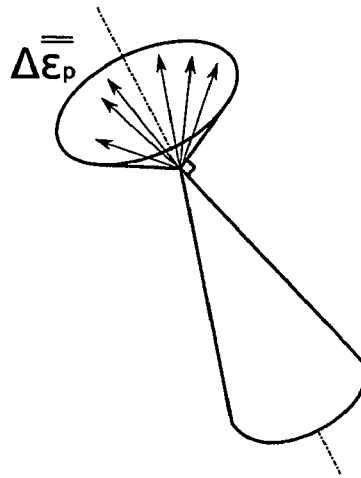


Figure 3.12: schematic representation of the apex derivation problem.

The apex return vector is more complicated than the smooth one due to the discontinuity at the apex of the cone [42]. It has been theoretically proven that the solution of this derivation problem is contained in a complementary cone as illustrated in Figure 3.12. Applying workguidelines provide from [42] the return vector to the apex is determined by:

$$\overline{\overline{N}}_d = 0 \quad (3.30)$$

$$\overline{\overline{N}}_v = \tan \psi \cdot \overline{\overline{I}} \quad (3.31)$$

where $\overline{\overline{N}}_d$ and $\overline{\overline{N}}_v$ are the counterpart of deviatoric stress and hydrostatic pressure to the return vector respectively.

As illustrated in Figure 3.13a the choice of the appropriate return vector is realized by determining the sign of the following relation:

$$\sigma_{eq} - G \cdot \Delta\gamma \quad (3.32)$$

Then the two kinds of return vectors are shown in Figure 3.13 b.

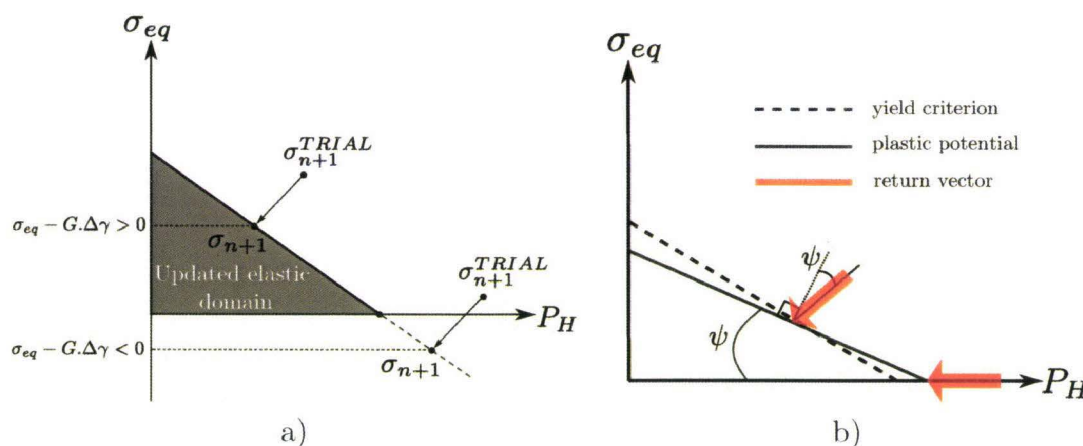


Figure 3.13: a) selection of the appropriate return vector and b) resulting return vectors.

3.5.3 Description of the yield return for the shear and compressive loadings

For the shear and compressive loadings, the assumption of no damage evolution is made, so classical plasticity theory is used. The effect of the classical plasticity theory is focused on the formulation of the return vectors. As explained in Figure 3.10 the return vector as to be fully deviatoric to model an isochoric plasticity. From the previous formulation explained in paragraph 3.5.2 in which the return vector is expressed

$$\overline{\overline{N}} = \overline{\overline{N}}_d + \overline{\overline{N}}_v. \quad (3.33)$$

The deviatoric part of the return vector \bar{N}_d is equal to:

$$\bar{N}_d = \frac{3}{2} \cdot \frac{\bar{s}}{\sqrt{3 \cdot J_2(\bar{s})}} \quad (3.34)$$

and the volumetric part \bar{N}_v is equal to 0. A summary of the return vectors for tensile, shear and compressive loadings is given in Figure 3.14.

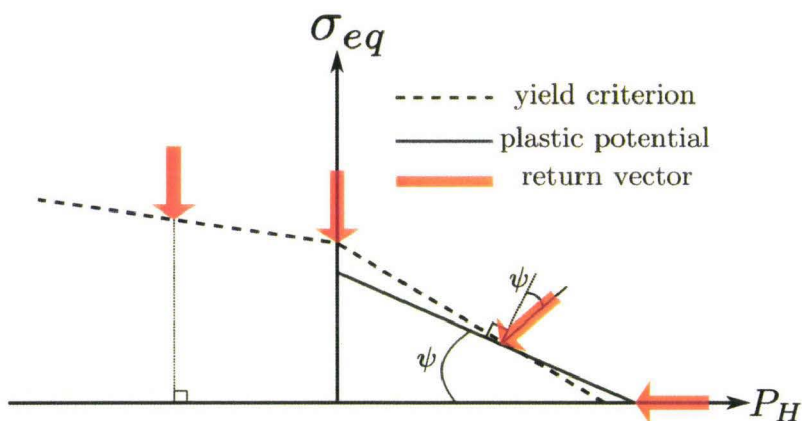


Figure 3.14: return vectors for the tensile, shear and compressive cases.

3.5.4 Description of Newton-Raphson algorithm

The return to the yield surface is performed by using the implicit closed point method [42] [44] (Figure 3.15).

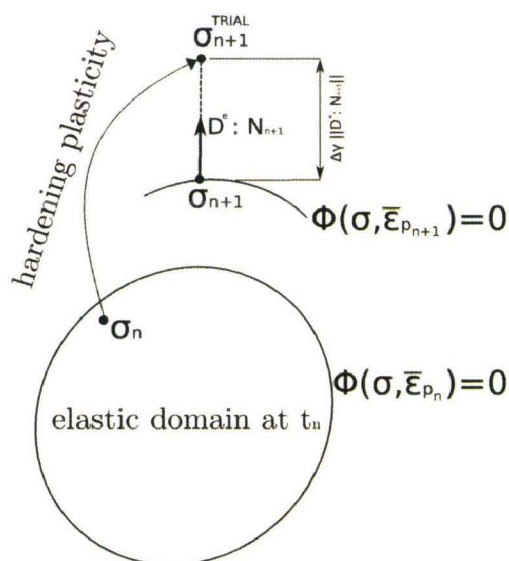


Figure 3.15: illustration of closed point method.

The computation of the plastic multiplier needed to determine the equivalent plastic strain is carried out with a Newton Raphson algorithm. Here the description of this algorithm is only realized for the smooth return vector of the plastic potential and for the tensile-shear of yield criterion.

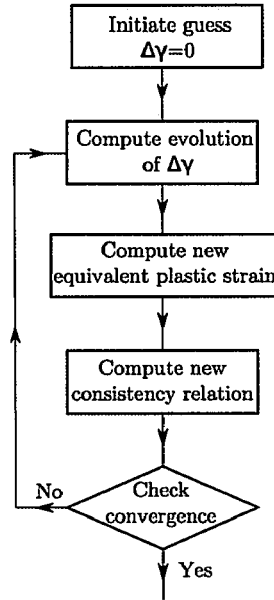


Figure 3.16: Newton Raphson algorithm schema.

At the beginning of the Newton Raphson algorithm, the plastic multiplier $\Delta\gamma$ is set to 0. Then the evolution of $\Delta\gamma$ is computed following

$$\Delta\gamma^{(k)} = \Delta\gamma^{(k-1)} - \Delta\dot{\gamma} \quad (3.35)$$

where k is the current iteration of the Newton Raphson algorithm and $\Delta\dot{\gamma}$ is computed by

$$\Delta\dot{\gamma} = \frac{\phi_{cons}}{\frac{\partial\phi_{cons}}{\partial\Delta\gamma}} \quad (3.36)$$

where ϕ_{cons} is the consistency relation defined by

$$\phi_{cons} = \sigma_{eq} - 3.G.\Delta\gamma + \tan\beta_1 \cdot (P_H^{TRIAL} - K.\tan\psi) - \left(1 + \frac{\tan(\beta_1)}{3}\right) \cdot (1-d) \cdot \sigma_{t(n+1)} \quad (3.37)$$

where G is the shear modulus defined by

$$G = \frac{E \cdot (1-d)}{1+\nu} \quad (3.38)$$

and K is the bulk modulus defined by

$$K = \frac{E \cdot (1-d)}{3 \cdot (1-2\nu)} \quad (3.39)$$

The derivative of the consistency relation by the plastic multiplier is formulated as follows

$$\frac{\partial \phi_{cons}}{\partial \Delta \gamma} = -3.G - \tan \beta_1 . K . \tan \psi - \left(1 + \frac{\tan (\beta_1)}{3} \right) . (1 - d) . \frac{\partial \sigma_{t(n+1)}}{\partial \Delta \gamma} \quad (3.40)$$

The derivative of the plastic behaviour law by the plastic multiplier is not realized analytically but numerically (Figure 3.17).

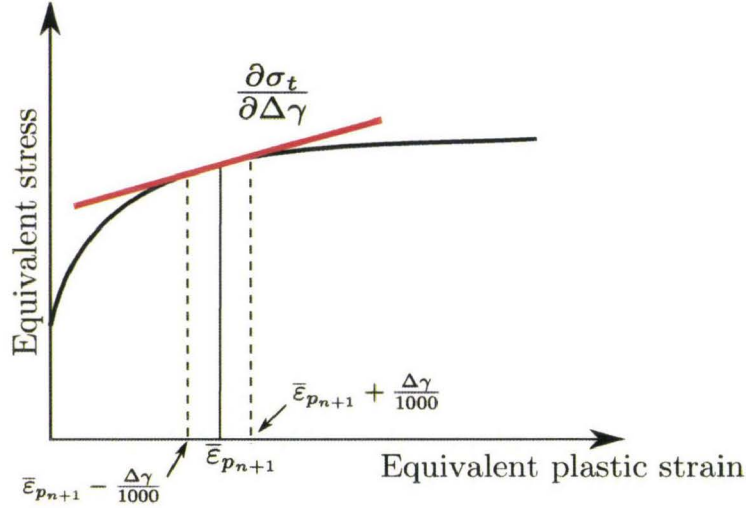


Figure 3.17: illustration of numerical derivation of tensile plastic behaviour law.

The equivalent plastic strain is then updated using

$$\bar{\epsilon}_P(t) = \bar{\epsilon}_P(t - \Delta t) + \Delta \gamma . \|\bar{N}\|. \quad (3.41)$$

The plastic behaviour law is then updated and consistency relation too. Until the convergence criterion (equation 3.39) is not reached, the iterative Newton Raphson algorithm is used.

$$\frac{\phi_{cons}}{\sigma_t} < 1e^{-6}. \quad (3.42)$$

3.6 Results update

If the material is considered purely elastic. Stresses are updated with the elastic prediction as follows

$$\bar{\bar{\sigma}}_{n+1} = \bar{\bar{s}}^{TRIAL} + P_H^{TRIAL} . \bar{\bar{I}}. \quad (3.43)$$

If plasticity is developed then the stresses are updated by using the following expression

$$\bar{\bar{\sigma}}_{n+1} = \left(1 - 3 . \frac{E . (1 - d)}{2 . (1 + \nu)} . \frac{\Delta \gamma}{\sigma_{eq}^{TRIAL}} \right) . \bar{\bar{\sigma}}^{TRIAL} + \left(P_H^{TRIAL} - \frac{E . (1 - d)}{3 . (1 - 2 . \nu)} . \tan \psi . \Delta \gamma \right). \quad (3.44)$$

The elastic strains are also updated by using a ratio of the previous relation

$$\bar{\bar{\epsilon}}_{en+1} = \left(\frac{(1+\nu)}{E \cdot (1-d)} - \frac{3}{2} \frac{\Delta\gamma}{\sigma_{eq}^{TRIAL}} \right) \cdot \bar{\sigma}^{TRIAL} + \left(\frac{(1-2\nu)}{E \cdot (1-d)} \cdot P_H^{TRIAL} - \frac{1}{3} \cdot \tan \psi \cdot \Delta\gamma \right) \cdot \bar{I}. \quad (3.45)$$

The damage parameter is updated using

$$d_{n+1} = d_n + \Delta d \quad (3.46)$$

where the damage increment Δd is computed as follows

$$\Delta d = d(\eta_t, \bar{\epsilon}_P(t)) - d(\eta_t, \bar{\epsilon}_P(t - \Delta t)). \quad (3.47)$$

As shown in Figure 3.18, this kind of damage update avoid a jump in damage evolution and ensure the stability of the calculation.

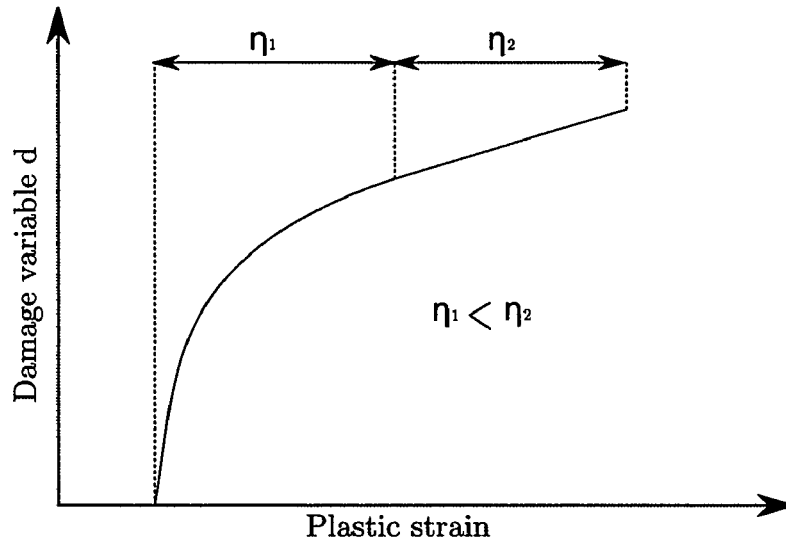


Figure 3.18: illustration of damage update technique.

3.7 Summary of the mesoscopic behaviour model implementation

The algorithm implemented into the subroutine VUMAT is represented in Figure 3.19.

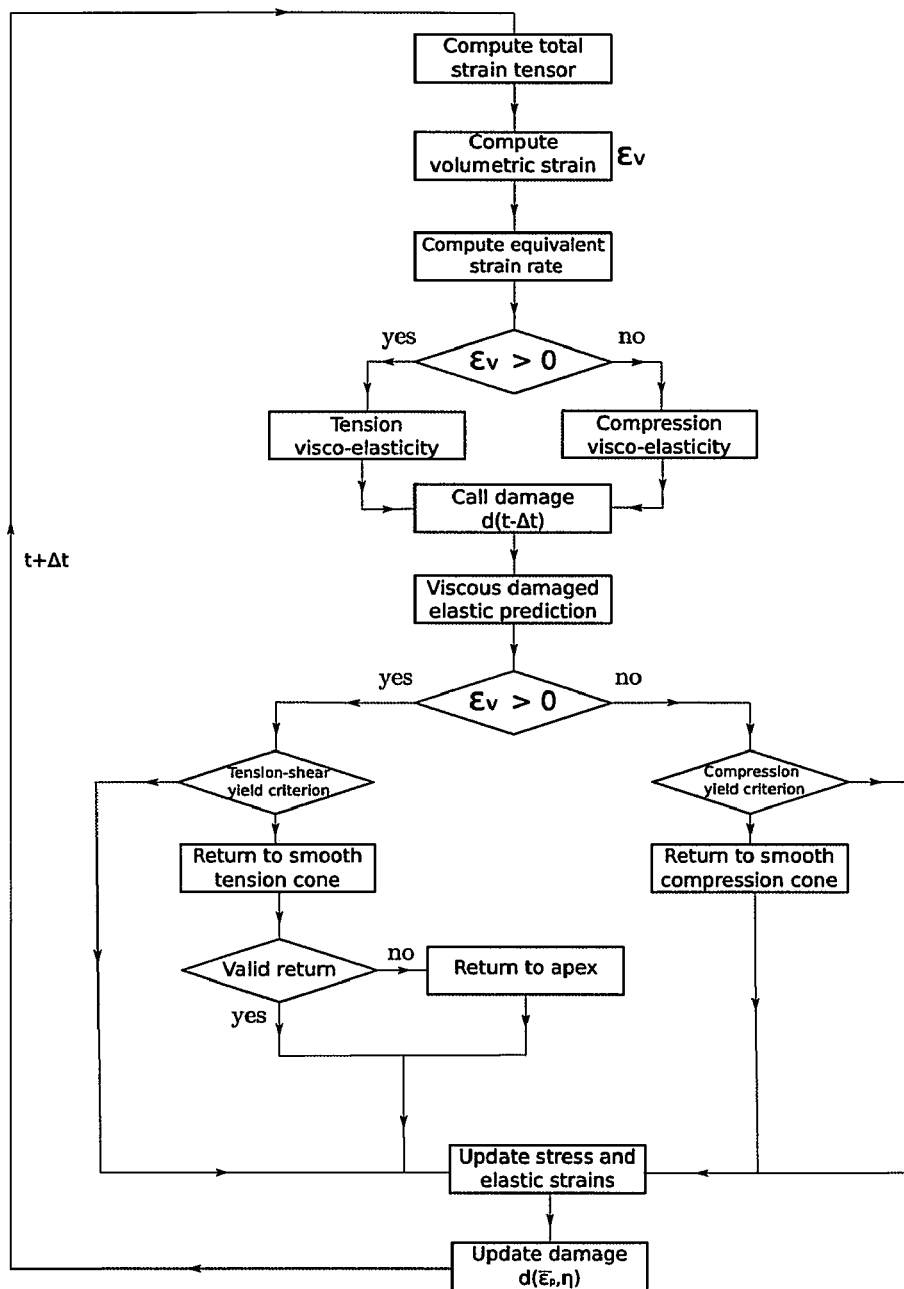


Figure 3.19: algorithm of the implemented behaviour model.

3.8 Conclusions

This chapter brings the complete description of the material model used in the mesoscopic FE analysis. This model is able to capture all the mechanical behaviour specificities of the considered toughened epoxy adhesive identified in Chapter 2. This is possible by combining a visco-elastic model followed by a hydrostatic pressure dependent yield criterion. The non-isochoric plasticity is tackled by a non-associative plasticity and a

triaxiality stress ratio dependent damage model. The full model is implemented into ABAQUS explicit code through a user-material subroutine and is available for volumic elements.

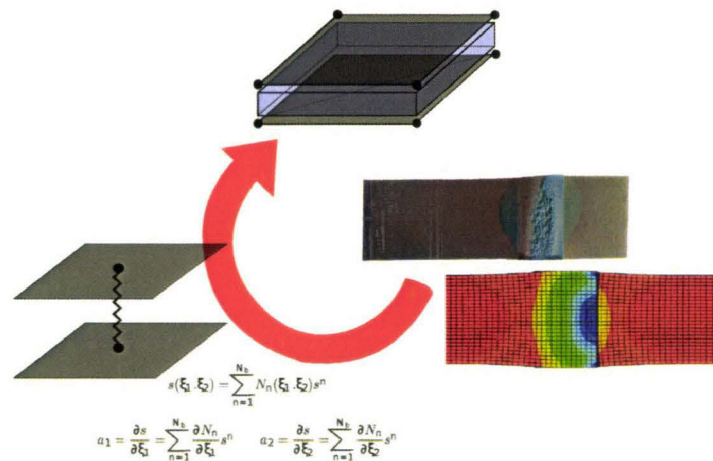
Macroscopic finite element model

Contents

4.1	Literature study and proposed models	72
4.2	User-element implementation	77
4.3	Crack propagation through a mesh	86
4.4	Properties identification	87
4.5	Conclusions	100
4.6	Models parameters summary	101

Resume

The aim of this chapter is to present the finite element implementation of the macroscopic finite element model. Here are described the simplification needed for the macroscopic representation of bonded joint in finite element. Moreover the numerical implementation is also described with the elasto-visco plastic behaviour and the failure initiation and propagation.



4.1 Literature study and proposed models

The main limitation of modeling bonded joints in finite element simulations in industrial context is focused on the time step used in explicit calculations. This time step is evaluated with the classical criterion of Friedrichs and Levy [45]:

$$\Delta t = l \cdot \sqrt{\frac{\rho}{E}} \quad (4.1)$$

where l is the shortest length of the considered element, ρ its volumic mass and E its elastic modulus.

In the particular case of a typical crashbox in steel (Figure 4.1), a typical industrial approach could lead to use the mass scaling to artificially increase the volumic mass to reach the time step of steel shells. A such approach leads to an increase of $\approx 200\%$ of adhesive volumic mass and results into a non-physical representation of bonded joints.

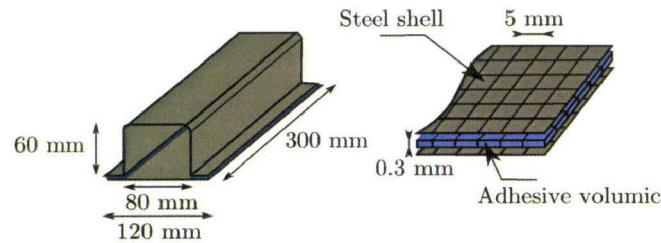


Figure 4.1: typical crashbox configuration.

To avoid this problem some special purpose elements have been designed on the basis of the spring element (Figure 4.2), which its time step is defined by

$$\Delta t = 2 \cdot \sqrt{\frac{m_1 \cdot m_2}{m_1 + m_2} \cdot \frac{1}{k}} \quad (4.2)$$

where m_1, m_2 are the masses at the spring boundaries, k its rigidity and $m_{1,2}, k$ are defined by:

$$m_{1,2} = m_{steel} + \frac{1}{2} \cdot m_{adhesive} \quad k = \frac{A \cdot E}{l} \quad (4.3)$$

where m_{steel} is the mass of the connected steel element, $m_{adhesive}$ the mass of the adhesive element, A its cross-section area and l its length.

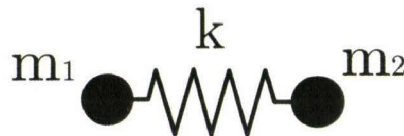


Figure 4.2: representation of spring element.

An application of the spring element time step is given in Table 4.1, this table shows the difference between the time step obtained with a classical volumic element and with the spring one. The advantage of the spring element time step is then clearly highlighted.

A	$1e^{-6}$ m		
E	$2.5e^9$ Pa		
l	0.3 mm		
		Time step (in μ s)	
		Spring element	Volumic element
		1.9	0.2

Table 4.1: adhesive element properties and related time steps.

In addition of classical spring element, this time step formulation is also used in interface elements [46] due to the small or non-existent thickness of the elements. In the interface elements [47], the stress tensor is reduced to (Figure 4.3):

$$\bar{\bar{\sigma}} = \begin{bmatrix} 0 & 0 & \tau_{t_2} \\ \cdot & \sigma_n & \tau_{t_1} \\ \cdot & \cdot & 0 \end{bmatrix} = \begin{bmatrix} \sigma_n \\ \tau_{t_1} \\ \tau_{t_2} \end{bmatrix} \quad (4.4)$$

where σ_n is the normal stress to the interface and τ_{t_1} , τ_{t_2} the tangential stress to the interface.

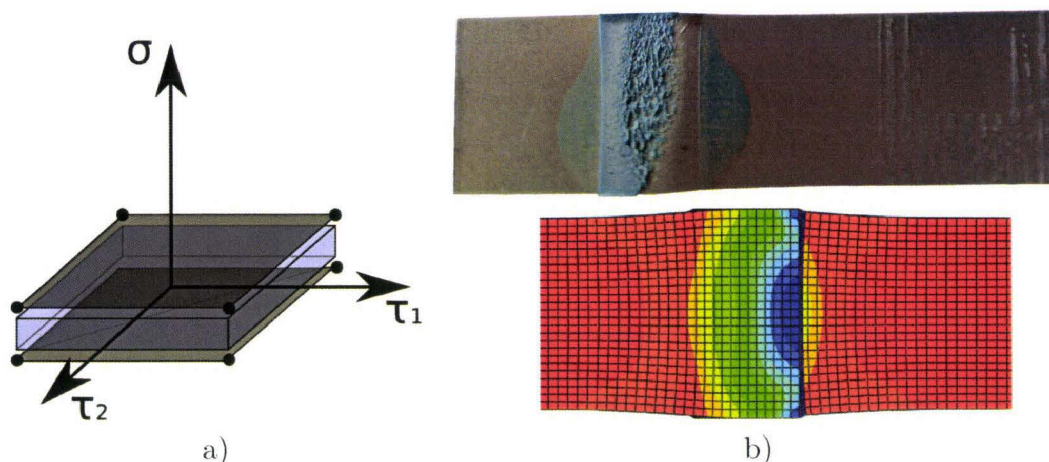


Figure 4.3: a) representation of stress tensor in an interface element and b) justification of interface elements.

Before to present the available interface elements in the literature, the modeling of bonded joints as interfaces has to be justified. Firstly, the thickness of bonded joints (typically 0.3 mm) can be totally neglected in face of a crashbox length (typically 300 mm) and of course in face of a car length (4-5 m). In addition to these geometrical considerations, in the case of a normative single lap joint test (Figure 4.3) the deformation which occurs in steel sheets does not take place on top and bottom of bonded joints. So the stresses and strains which occur in the bonded joint plane can be totally neglected because no deformation of adherents will occur and then there is no effect of the adhesive Poisson's ratio.

The interface elements used in literature to model the bonded joints are generally the cohesive zone models. These cohesive elements are divided into two families (Figure 4.4):

- the discrete cohesive zone models (DCZM),
- the continuum cohesive zone models (CCZM).

The difference of these two kinds of models is focused on their 'geometries', in one hand there is the DCZM [48, 49] which represents the bonded joints with springs and on the other hand the CCZM [50, 51] represents the bonded joints by a volume.

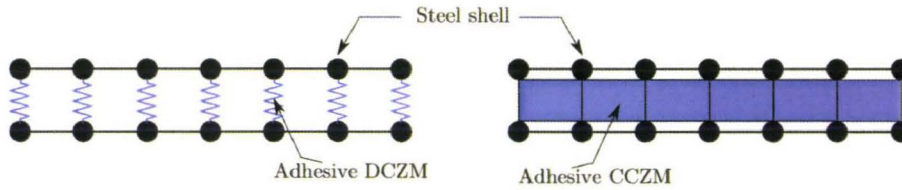


Figure 4.4: difference between discrete and continuum cohesive zone models.

The DCZM and CCZM also differs from their traction-separation laws. The traction-separation law of a DCZM or CCZM defines the behaviour and failure of the adhesive interface. A simple comparison with the attraction and repulsive between two atoms explains the principle of a traction-separation law (Figure 4.5). Until the maximum force F_m is not reached, the deformation process is reversible but after this maximum force, the phenomenon is irreversible but each atom still feel the attraction force of the other.

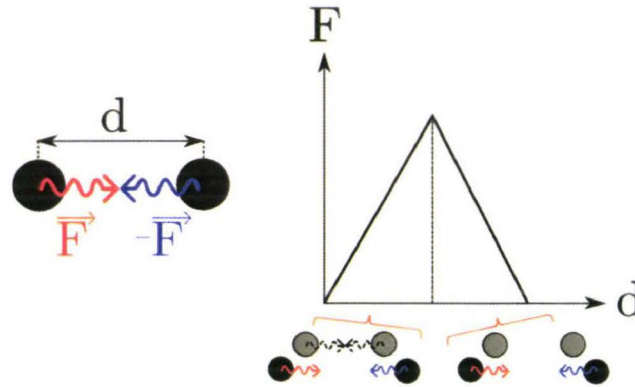


Figure 4.5: illustration of the principle of a traction-separation law.

Based on this principle, different traction-separation law are available in the literature for the DCZM and CCZM models. The traction-separation laws of CCZM are obtained by differentiation of a cohesive potential ϕ depending of the sliding and opening displacements δ_n, δ_t [52]. For the DCZM models the traction-separation laws are not obtained by the differentiation of a cohesive potential but are defined following classical mechanical properties. So depending on the material properties, different traction-separation laws

are available in the literature. For the brittle materials, a classical triangular law is defined (Figure 4.6a) in which the material is then considered as purely elastic [53]. For the ductile materials, a traction-separation law (Figure 4.6b) with a pseudo-plasticity has been designed by Tvergaard et al [54].

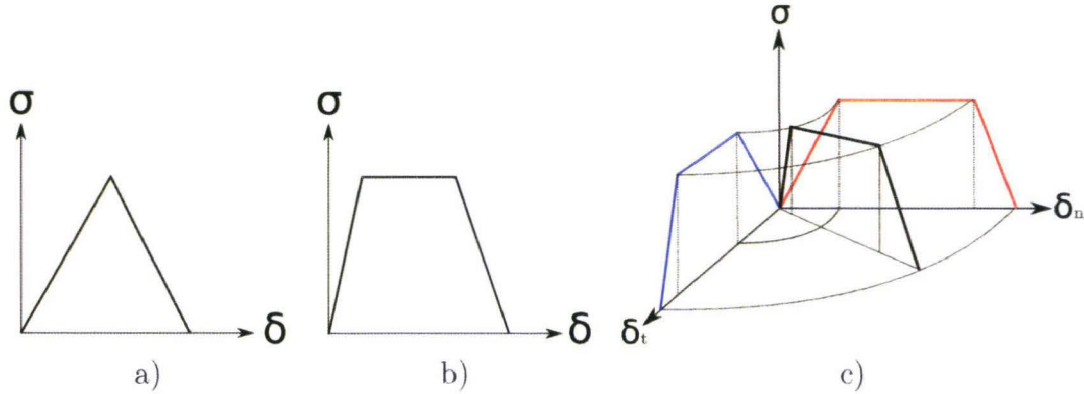


Figure 4.6: traction-separation laws for a) brittle, b) ductile materials and c) equivalent formulation.

Some DCZM and CCZM models are not defined on 3 independent springs like classical interface elements but use an equivalent formulation (Figure 4.6c). In these elements, the traction-separation law is then a function of an equivalent opening displacement λ defined by:

$$\lambda = \sqrt{\left(\frac{\delta_n}{\delta_{nc}}\right)^2 + \left(\frac{\delta_t}{\delta_{tc}}\right)^2 + \left(\frac{\delta_\tau}{\delta_{\tau c}}\right)^2} \quad (4.5)$$

where δ_{nc} , δ_{tc} and $\delta_{\tau c}$ are the critical opening and sliding displacements.

The classical properties of such elements like elastic modulus (E) and the peak stress ($\hat{\sigma}$) can be identify on classical butt joint tests (Figure 4.7) and the failure energies ($G_{I/II}$) are classically identify on pre-cracked specimens. Although this identification can be realize directly on experiments using the theory of linear elastic fracture mechanics for the brittle materials or with the non-linear fracture mechanics for the ductile ones or numerically using J-contour integrale techniques, they always lead to a complex identification technique with high level hypothesis.

In this work, a new cohesive element is then proposed based on the time step of the spring element and using 3 independant springs (Figure 4.8). On the basis of an interface element, the main mechanical properties of a toughened epoxy adhesive are taken into account:

- elastic moduli and yield difference in tension/compression,
- hardening visco-plasticity,
- damage evolution.

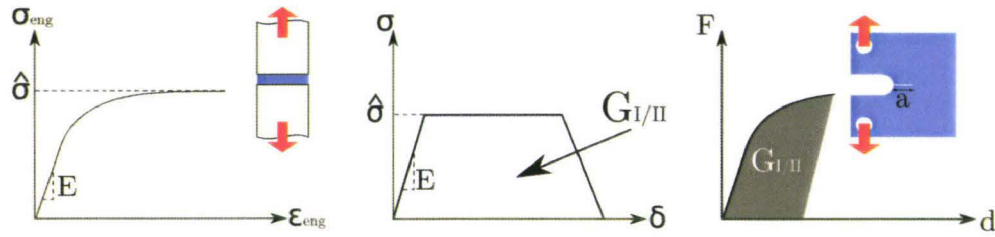


Figure 4.7: cohesive elements properties identification.

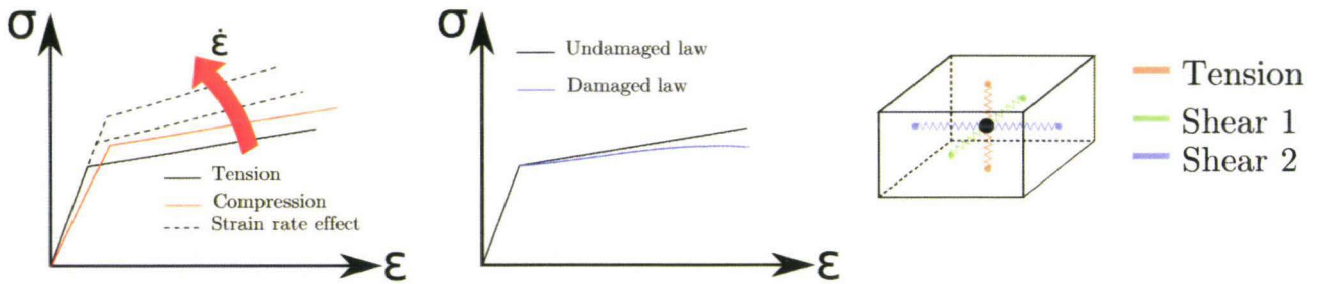


Figure 4.8: new cohesive element properties.

Moreover the element elimination is handled with a physical aspect (Figure 4.9), the peak stress is defined as the crack initiation and the decreasing stress is then translated as the crack propagates through the element.

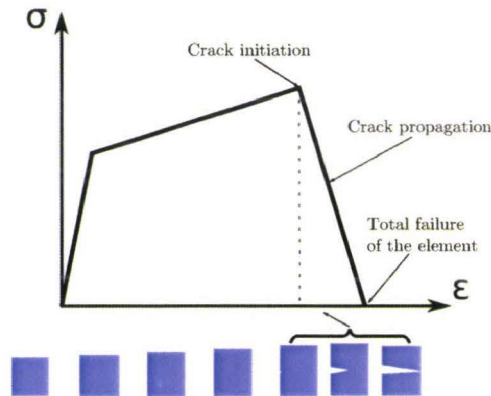


Figure 4.9: crack propagation through an element.

In terms of properties identification, the classical properties like elastic moduli, viscoplasticity and damage are identified on bulk adhesive specimens (Chapter 2) using a simplify analysis. The failure initiation and propagation are then identified on assemblies tests like double lap joints tests for shear properties and double U tests for tensile properties.

4.2 User-element implementation

4.2.1 General description of finite element implementation

The proposed cohesive element is implemented in ABAQUS explicit FE code. In ABAQUS explicit, the cohesive element is implemented into a Vectorized User Element (VUEL) subroutine, this subroutine gives an access to each step of the explicit finite element computation. In equation (4.6) the mass matrix M^{NJ} and nodal forces $F_{(i)}^J$ have to be provided by the user. For the equations (4.7) and (4.8), the critical time step has also to be provided by the user.

$$\ddot{u}_{(i)}^N = (M^{NJ})^{-1}(P_{(i)}^J - F_{(i)}^J) \quad (4.6)$$

$$\dot{u}_{(i+\frac{1}{2})}^N = \dot{u}_{(i-\frac{1}{2})}^N + \frac{\Delta t_{(i+1)} + \Delta t_{(i)}}{2} \ddot{u}_{(i)}^N \quad (4.7)$$

$$u_{(i+1)}^N = u_{(i)}^N + \Delta t_{(i+1)} \dot{u}_{(i+\frac{1}{2})}^N \quad (4.8)$$

Then each step of the VUEL is described in Figure 4.10.

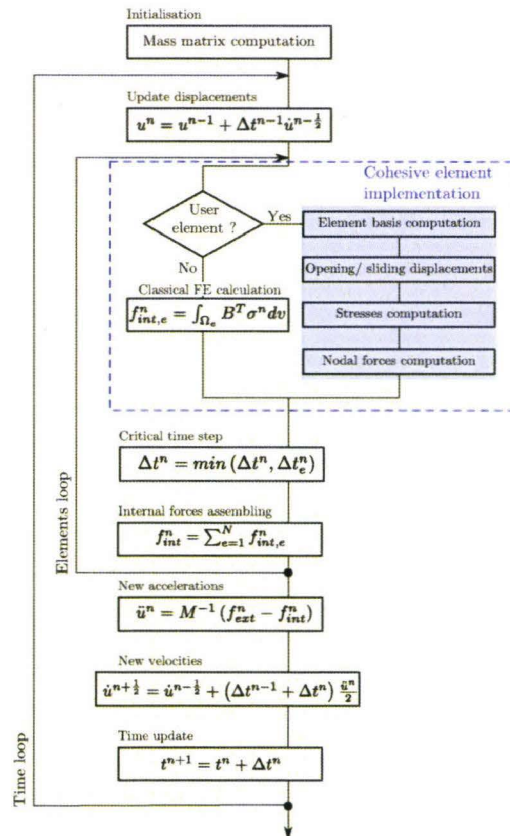


Figure 4.10: flowchart for the implementation of the cohesive element.

4.2.2 Mass matrix computation

In explicit software, the mass matrix has to be provide under a diagonalized form and its computation is only performed one time at the beginning of the simulation. The diagonalized form is needed so as to accelerate the computation. So as to circumscribe the time needed for the diagonalization of a classical mass matrix (equation 4.9), the lumped matrix technique is used [55].

$$M^{NJ} = \int_{\Omega} N^T \rho N d\Omega \quad (4.9)$$

where N is the matrix of the shape function of a classical 8 nodes element and ρ the density of the adhesive.

The lumped matrix technique defines a diagonalized matrix by the sum of each row as described in equation 4.10. The error made with this kind of calculation is important if during the simulation the mass matrix is updated [55].

$$M^{NJ} = \begin{pmatrix} \sum M(i,:) & & & 0 \\ & \sum M(i,:) & & \\ & & \dots & \\ 0 & & & \sum M(i,:) \end{pmatrix} \quad (4.10)$$

4.2.3 Local covariant basis computation

A local basis inside the cohesive element is needed to obtain the displacements feels by the element. For that a local covariant basis (Figure 4.11) is used.

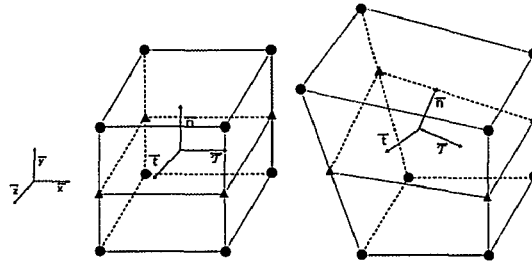


Figure 4.11: illustration of local basis.

In this basis, a shell is defined in the middle plane of the element. In this plane a position vector is defined as:

$$\vec{s}(\xi_1, \xi_2) = \sum_{n=1}^{N_b} N_n(\xi_1, \xi_2) \vec{s}^n \quad (4.11)$$

where ξ_1, ξ_2 are the normalized position in the plane ($0 \leq \xi \leq 1$), \vec{s}^n the position vector, N_b the matrix of the shape function of a classical 4 nodes element.

From the position vector $\vec{s}(\xi_1, \xi_2)$ the two in-plane vectors (\vec{a}_1, \vec{a}_2) of the shell are defined by derivation of $\vec{s}(\xi_1, \xi_2)$ following

$$\vec{a}_1 = \frac{\partial \vec{s}}{\partial \xi_1} = \sum_{n=1}^{N_b} \frac{\partial N_n}{\partial \xi_1} s^{\vec{n}} \quad \vec{a}_2 = \frac{\partial \vec{s}}{\partial \xi_2} = \sum_{n=1}^{N_b} \frac{\partial N_n}{\partial \xi_2} s^{\vec{n}}. \quad (4.12)$$

The local basis vectors which are normed, are computed from the surfacique element vectors following:

$$\vec{t} = \frac{\vec{a}_1}{\|\vec{a}_1\|} \quad \vec{n} = \frac{\vec{t} \wedge \vec{a}_2}{\|\vec{a}_2\|} \quad \vec{\tau} = \vec{n} \wedge \vec{t} \quad (4.13)$$

4.2.4 Opening and sliding displacements description

Like the local basis is defined, the opening and sliding displacements are then computed from the projection of the relative displacements in the global basis to the local one. The relative displacements are computed follows

$$U = \frac{U_1+U_2}{2} + \frac{U_3+U_4}{2} \quad V = \frac{V_1+V_2}{2} + \frac{V_3+V_4}{2} \quad W = \frac{W_1+W_2}{2} + \frac{W_3+W_4}{2} \quad (4.14)$$

where $U_{1 \rightarrow 4}$, $V_{1 \rightarrow 4}$, $W_{1 \rightarrow 4}$ are the relative displacements computed under each pairs of nodes as illustrated in Figure 4.12.

By realizing a such calculation, the relative displacements U , V and W are obtained in the center of the element like a classical computations of an element with one Gauss point.

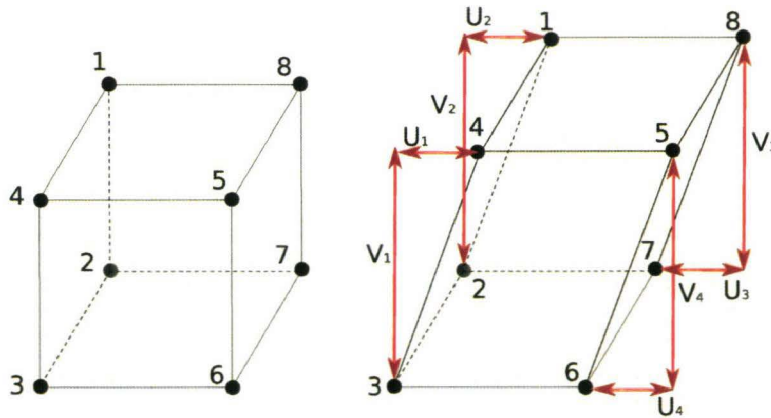


Figure 4.12: example of relative displacements computations for U and V .

Then the opening and sliding displacements (δ_n , δ_t and δ_τ) are obtained by the projection of the global relative displacements into the local basis

$$\delta_n = \begin{bmatrix} U \\ V \\ W \end{bmatrix}_{\bar{x},\bar{y},\bar{z}} \cdot \vec{n} \quad \delta_t = \begin{bmatrix} U \\ V \\ W \end{bmatrix}_{\bar{x},\bar{y},\bar{z}} \cdot \vec{t} \quad \delta_\tau = \begin{bmatrix} U \\ V \\ W \end{bmatrix}_{\bar{x},\bar{y},\bar{z}} \cdot \vec{\tau} \quad (4.15)$$

4.2.5 Strains and strain rates computations

The tangential and normal strains of the cohesive element are computed from the local opening and sliding displacements following

$$\varepsilon_n = \ln\left(1 + \frac{\delta_n}{L_{y,0}}\right) \quad \varepsilon_t = \ln\left(1 + \frac{\delta_t}{L_{x,0}}\right) \quad \varepsilon_\tau = \ln\left(1 + \frac{\delta_\tau}{L_{z,0}}\right) \quad (4.16)$$

where $L_{y,0}$, $L_{x,0}$ and $L_{z,0}$ are the initial dimensions of the element as shown in Figure 4.13.

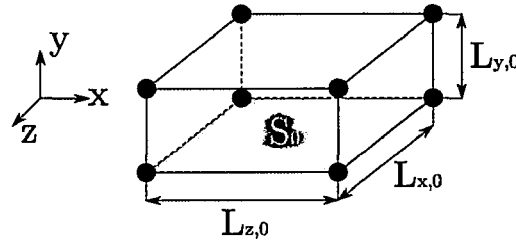


Figure 4.13: illustration of initial element dimensions.

This kind of strain computations is only valid if the bonded joint is modeled with its true thickness and not as an interface (thickness equal to 0).

The strain rate is computed by a backward finite difference

$$\dot{\bar{\varepsilon}} = \frac{\bar{\varepsilon}(t) - \bar{\varepsilon}(t-\Delta t)}{\Delta t} \quad (4.17)$$

where $\bar{\varepsilon}$ is computed from

$$\bar{\varepsilon} = \sqrt{\frac{2}{3} \bar{\varepsilon} : \bar{\varepsilon}} \quad (4.18)$$

with $\bar{\varepsilon}$ the strain tensor defined by

$$\bar{\varepsilon} = \begin{bmatrix} 0 & 0 & \varepsilon_t \\ \cdot & \varepsilon_n & \varepsilon_\tau \\ \cdot & \cdot & 0 \end{bmatrix} \quad (4.19)$$

4.2.6 Stresses computations

4.2.6.1 Description of elastic prediction

With the previous strains (equation 4.16), three elastic predictions are then realized for the three independent springs following:

$$\sigma_n = E_n \cdot \varepsilon_n \quad \sigma_t = E_t \cdot \varepsilon_t \quad \sigma_\tau = E_t \cdot \varepsilon_\tau \quad (4.20)$$

where E_n and E_t are the elastic moduli in tension/compression and shear respectively. Here different moduli are assigned for the tension and compression.

Following the elastic predictions, three yield criteria are then applied with:

$$f_n = \sigma_{yn} - \sigma_n \quad f_t = \sigma_{yt} - \sigma_t \quad f_\tau = \sigma_{yt} - \sigma_\tau \quad (4.21)$$

where σ_{yn} and σ_{yt} are the yield stresses in tension/compression and shear. Here again different yield limit are assigned for both tension and compression.

To take into account the dependency of the yield stress to the strain rate, the yield stresses are formulated following

$$\sigma_{yn_t} = A_t + B_t \cdot \dot{\varepsilon}^{n_t} \quad \sigma_{yn_c} = A_c + B_c \cdot \dot{\varepsilon}^{n_c} \quad (4.22)$$

From the experimental observations of Chapter 2, the yield stress in tension and shear are assumed to be equal.

4.2.6.2 Description of plasticity and yield return algorithm

Until the yield criterion is reached the yield return is realized by a direct method. Firstly the plastic strains for the 3 independent springs are computed following

$$\varepsilon_{pn} = \varepsilon_n - \frac{\sigma_{yn}}{E_n} \quad \varepsilon_{pt} = \varepsilon_t - \frac{\sigma_{yt}}{E_t} \quad \varepsilon_\tau = \varepsilon_\tau - \frac{\sigma_{yt}}{E_t}. \quad (4.23)$$

Then a correction is applied on the stresses following:

$$\sigma_n = \sigma_{yn} + (1 - d) \cdot E_{Tn} \cdot \varepsilon_{pn} \quad \sigma_t = \sigma_{yt} + (1 - d) \cdot E_{Tt} \cdot \varepsilon_{pt} \quad \sigma_\tau = \sigma_{yt} + (1 - d) \cdot E_{Tt} \cdot \varepsilon_{p\tau} \quad (4.24)$$

where E_{Tn} , E_{Tt} are the tangent moduli in tension, compression and shear and d the damage variable. The damage variable d is updated before the stress corrections with an exponential formulation:

$$d = d_0 + d_1 \cdot (1 - e^{-d_3 \cdot \varepsilon_{pn}}). \quad (4.25)$$

Here the damage is only dependent of the normal plastic strain due to the hypothesis that in pure shear there is no damage evolution.

The effect of strain rate on the structural hardening of the behaviour law is managed with viscous tangent moduli. These tangent moduli are expressed with polynomial approximations.

4.2.7 Nodal forces update

When the stresses corrections are completed, the VUEL subroutine requires an update of the internal forces of the element. The internal forces are updated by a projection of the local stresses on each nodes (Figure 4.14).

To prevent the large rotations of the element, an incremental update of the internal forces is realized as follows

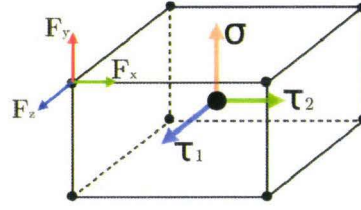


Figure 4.14: illustration of nodal forces update.

$$F_x(t) = F_x(t - \Delta t) + \begin{bmatrix} \Delta\sigma_n \\ \Delta\sigma_t \\ \Delta\sigma_\tau \end{bmatrix}_{\vec{n}, \vec{t}, \vec{\tau}} \cdot \vec{x} \cdot S_0 \cdot (1 - d) \quad (4.26)$$

$$F_y(t) = F_y(t - \Delta t) + \begin{bmatrix} \Delta\sigma_n \\ \Delta\sigma_t \\ \Delta\sigma_\tau \end{bmatrix}_{\vec{n}, \vec{t}, \vec{\tau}} \cdot \vec{y} \cdot S_0 \cdot (1 - d) \quad (4.27)$$

$$F_z(t) = F_z(t - \Delta t) + \begin{bmatrix} \Delta\sigma_n \\ \Delta\sigma_t \\ \Delta\sigma_\tau \end{bmatrix}_{\vec{n}, \vec{t}, \vec{\tau}} \cdot \vec{z} \cdot S_0 \cdot (1 - d) \quad (4.28)$$

where S_0 is the initial resistant section of the element (Figure 4.13) and $\Delta\sigma_n$, $\Delta\sigma_t$ and $\Delta\sigma_\tau$ the stress increments in the local basis. It could be noticed that the damaged section is used to update the nodal forces.

4.2.8 Element elimination

4.2.8.1 Failure initiation model

The failure initiation is detected with a criterion based on the opening and sliding displacements. This criterion is divided into two subcriteria (equation 4.29 and 4.30) due to the assumption that no crack propagation occurs in compression. Then, the criterion for tension and shear loading is defined as

$$\lambda_{init} = \sqrt{\left(\frac{\delta_n}{\delta_{n_{crit}}}\right)^2 + \left(\frac{\delta_t}{\delta_{t_{crit}}}\right)^2 + \left(\frac{\delta_\tau}{\delta_{\tau_{crit}}}\right)^2} \geq 1 \quad (4.29)$$

where $\delta_{n_{crit}}$ and $\delta_{t_{crit}}$ are the critical opening and sliding displacements. In case of compressive loading the failure initiation criterion is then defined as

$$\lambda_{init} = \sqrt{\left(\frac{\delta_t}{\delta_{t_{crit}}}\right)^2 + \left(\frac{\delta_\tau}{\delta_{\tau_{crit}}}\right)^2} \geq 1. \quad (4.30)$$

A geometrical description of the failure is given in Figure 4.15.

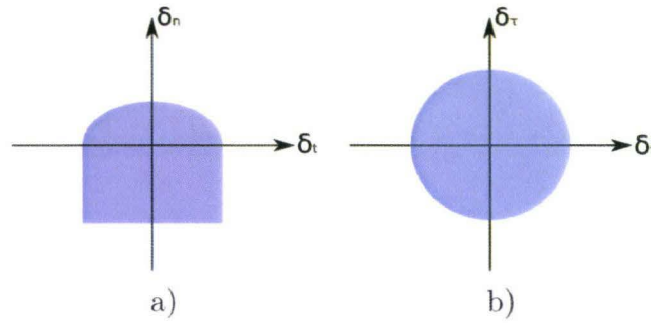


Figure 4.15: failure initiation criteria in the a) tension/shear and b) compression/shear.

4.2.8.2 Failure propagation model

Once the failure is initiated inside the element, a special algorithm is devoted to the crack propagation through the element. The crack propagation through the element is represented in Figure 4.16 by the decreasing of all stresses (here named σ_i) until they are equal to zero.

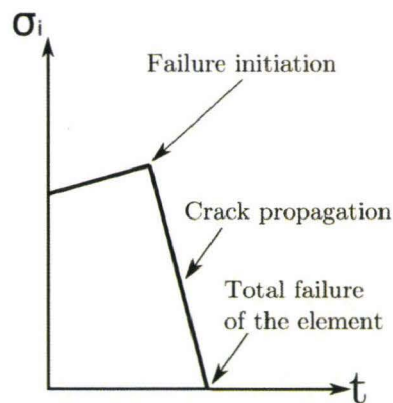


Figure 4.16: illustration of effect of crack propagation through an element.

The stresses of each springs are decreased using:

$$\sigma_i = \frac{-\sigma_{i_{init}}}{t_{rup}} \cdot (t - t_{init}) + \sigma_{i_{init}} \quad (4.31)$$

where $\sigma_{i_{init}}$ and t_{init} are the stress and time at failure initiation respectively. As the crack propagation through an element is depending of its size, a homogeneization parameter t_{rup} is used. This parameter represents the time needed by a crack to cross an element (Figure 4.17) and is defined by

$$t_{rup} = \frac{L_{x,0}}{V_p} \quad (4.32)$$

where $L_{x,0}$ is the size of the element (Figure 4.17) and V_p the crack propagation speed. As the crack propagation is dependent of the loading speed, V_p is defined by

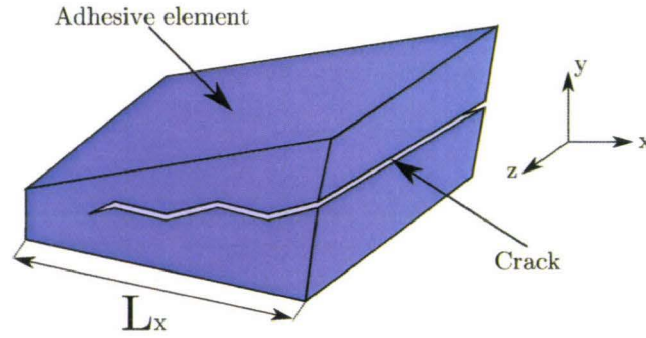


Figure 4.17: illustration of crack propagation through an element.

$$V_p = h.V_{eq} \quad (4.33)$$

where h is the ratio between equivalent loading speed and crack propagation speed. The equivalent loading (Figure 4.18) is defined by

$$V_{eq} = \|\vec{V}_{eq}\| = \sqrt{\dot{\delta}_n^2 + \dot{\delta}_t^2 + \dot{\delta}_\tau^2}. \quad (4.34)$$

where $\dot{\delta}_n$, $\dot{\delta}_t$ and $\dot{\delta}_\tau$ are defined by:

$$\dot{\delta}_n = \begin{bmatrix} \dot{U} \\ \dot{V} \\ \dot{W} \end{bmatrix}_{\bar{x}, \bar{y}, \bar{z}} \cdot \bar{n} \quad \dot{\delta}_t = \begin{bmatrix} \dot{U} \\ \dot{V} \\ \dot{W} \end{bmatrix}_{\bar{x}, \bar{y}, \bar{z}} \cdot \bar{t} \quad \dot{\delta}_\tau = \begin{bmatrix} \dot{U} \\ \dot{V} \\ \dot{W} \end{bmatrix}_{\bar{x}, \bar{y}, \bar{z}} \cdot \bar{\tau} \quad (4.35)$$

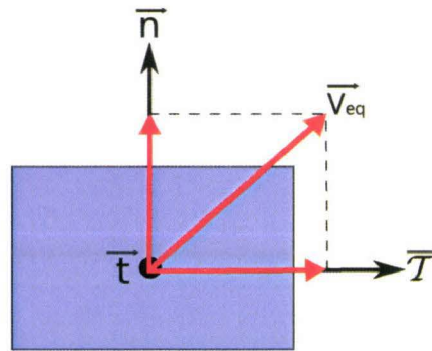


Figure 4.18: equivalent loading speed.

In explicit integration scheme, element elimination is always submitted to the question of stability. Although a physical aspect in element elimination is interesting, the numerical stability of the computation has to be guaranteed. For that a study on a simple numerical test is performed to investigate the effect of the element elimination on the force response of an assemblies. The assembly (Figure 4.19) is made of two U steel modeled with shell elements and linked by a macro element of adhesive. In terms of boundary conditions, all

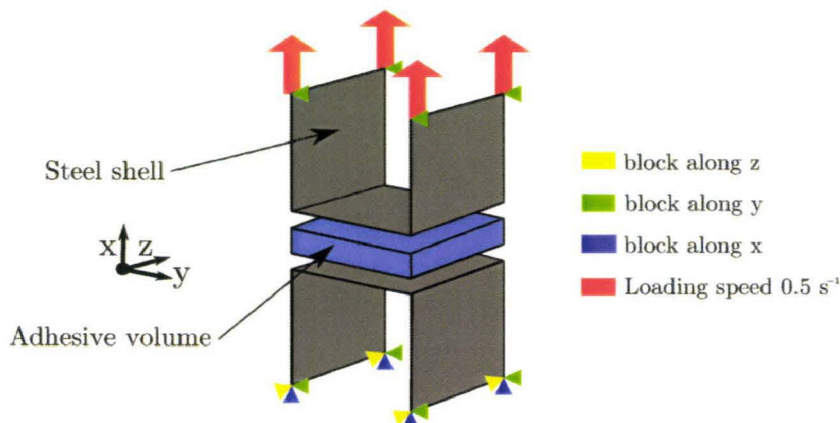


Figure 4.19: boundaries conditions and loading speed applied on tension numerical test.

displacements and rotations are blocked on the 4 nodes of the U bottom and a speed of 0.5 m.s^{-1} is applied on the 4 nodes of the U top.

Then the stability of the computation is studied by looking the reaction force along x axis (Figure 4.20 a and b).

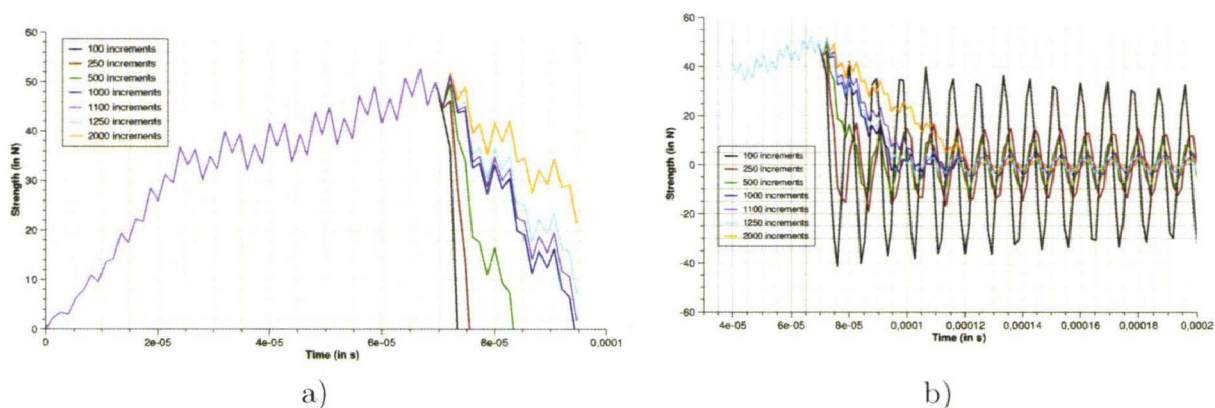


Figure 4.20: reaction force a) until crack propagation through the element and b) after the failure of the element.

It can be noticed that for a given time step, the stability of the computation after the failure of the element is highly depend on the increment numbers (Figure 4.20a and b). Using the time step of this computation, the ratio h between the crack propagation and the equivalent opening speeds can be easily computed from the number of increment and the width of the element. Assuming that on the simple study case, 250 increments is sufficient to remove the element and ensure a reasonable stability, the maximum ratio h is then found at approximately 28 (Figure 4.21). This criterion is used as a numerical security factor.

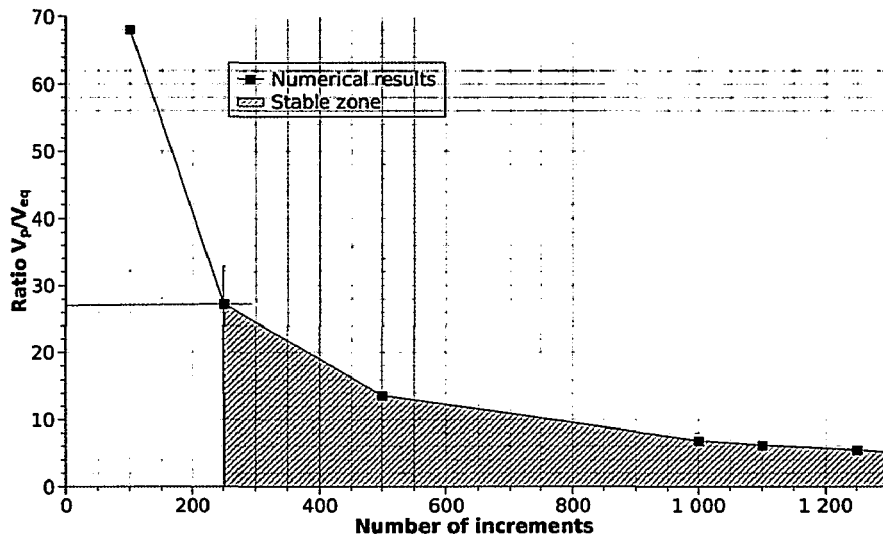


Figure 4.21: numerical study of the ratio h .

4.3 Crack propagation through a mesh

In addition to the propagation of a crack through a mesh, an experimental technique is defined in the element to propagate a crack through a mesh. This technique is based on two criteria:

- presence of a crack at the boundary of the element (Figure 4.22 a and b),
- reaching a mechanical criterion (equation 4.36).

$$\lambda_{prop} = \sqrt{\left(\frac{\delta_n}{\delta_{n_{crit}}}\right)^2 + \left(\frac{\delta_t}{\delta_{t_{crit}}}\right)^2 + \left(\frac{\delta_\tau}{\delta_{\tau_{crit}}}\right)^2} \geq \alpha \quad (4.36)$$

with $\alpha \leq 1$ for a crack propagation using Non Linear Fracture Mechanics.

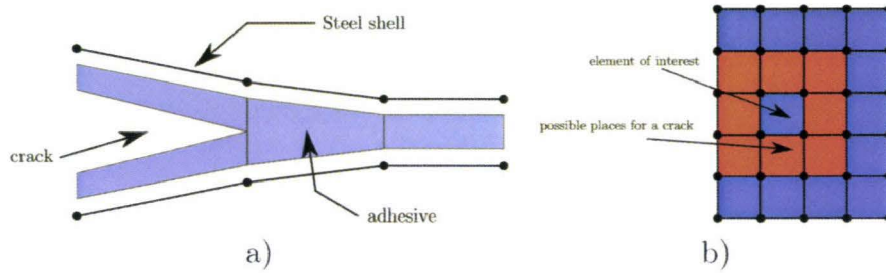


Figure 4.22: schematic representation of boundaries tests a) in face and b) in normal plane of the bonded joint.

By choosing α equal to zero the crack propagation is realized like in Linear Elastic Fracture Mechanics as Figure 4.23 shows in the special case DCB like test.

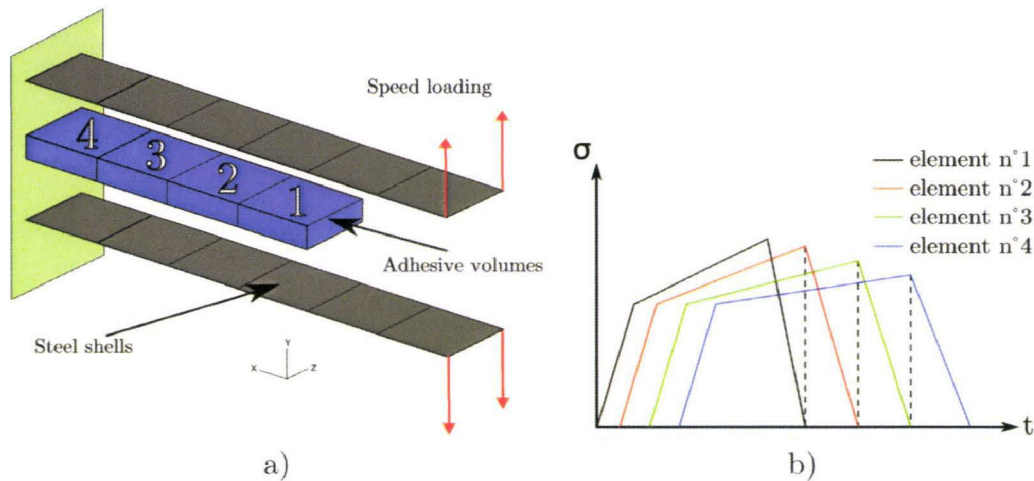


Figure 4.23: example of LEFM crack propagation a) DCB like simulation and b) evolution of stresses.

Although this technique is very interesting wide limitations are always present

- the perfect knowledge of the mesh numbering is mandatory,
- in ABAQUS explicit the numerical test are limited to a patch of 136 elements due to the block matrix computations.

Due to these limits, the use of this technique of crack propagation through a mesh is only suitable for laboratory tests and not for real industrial cases.

4.4 Properties identification

4.4.1 Work guidelines

The properties of the macroscopic approach are identified on two different kinds of tests (Figure 4.24)

- on bulk adhesive specimens (Chapter 2) for the behaviour parameters,
- on assemblies tests for the failure initiation and propagation parameters.

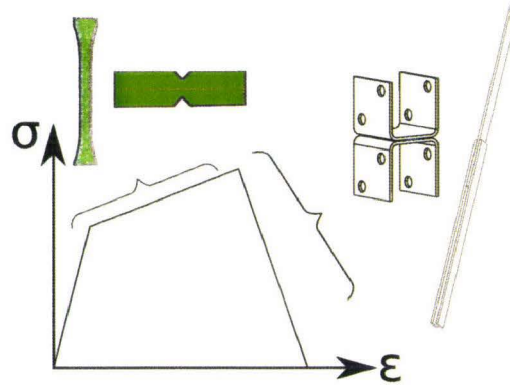


Figure 4.24: macroscopic approach properties identification guidelines.

4.4.2 Behaviour properties

4.4.2.1 Elasticity properties

The elastic properties are extracted from Figure 2.32 only for high strain rates and are summarized in the following table

	Tension	Compression
Elastic modulus (in GPa)	3	2

Table 4.2: summarize of the elastic properties of the macroscopic approach.

4.4.2.2 Plasticity properties

The plasticity properties comes from Figure 2.36 and 2.41 but are analysed with a simplified approach. The yield stress and its evolution with the strain rate is directly linked to the tangent modulus identification (Figure 4.25). The yield stress used in the macroscopic approach is determined by the intersection of the tangent modulus and the stress axis and an error is done on its evaluation.

Then following the previous principle, the yield stress in tension (Figure 4.26a) and compression (Figure 4.26b) are identified and mathematical models (equation 4.22) are identified.

The corresponding tangent modulus are shown in Figure 4.27 and the same tangent moduli in tension and compression are used. As the shear properties are not identified for different strain rates an extrapolation is carried out from the compression data.

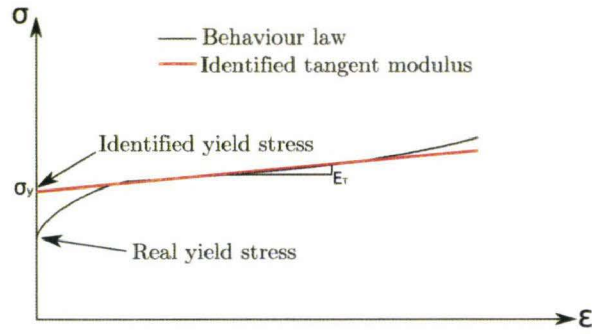


Figure 4.25: identification of yield stress in macroscopic approach.

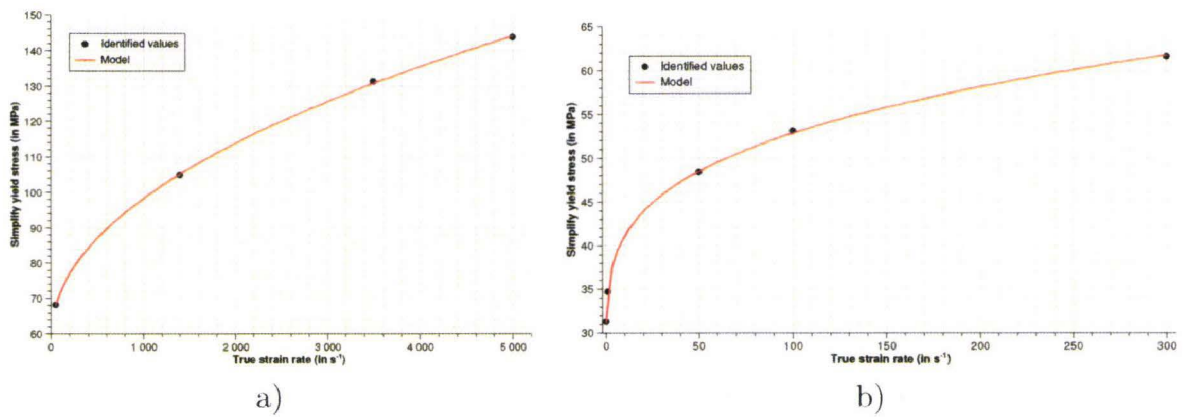


Figure 4.26: identified yield stresses and models for a) tension and b) compression.

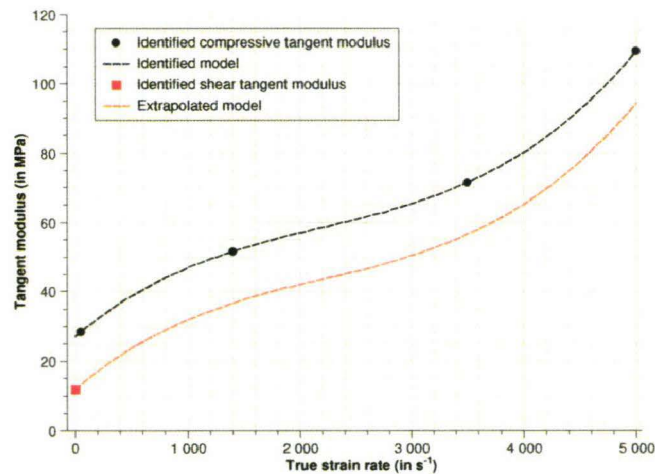


Figure 4.27: identification of tangent moduli in macroscopic approach.

4.4.3 Failure properties

4.4.3.1 Specimens geometries and loading devices

The failure properties ($\delta_{n_{crit}}, \delta_{t_{crit},h}$) are identified on assemblies tests, the tensile properties on double U specimens and the shear properties on double lap joint specimens. The geometries of the double U and double lap joints specimens are given in Figure 4.28 and Figure 4.29a and b respectively. For the double lap joints tests, two geometries are used so as to be adapted to the loading device.

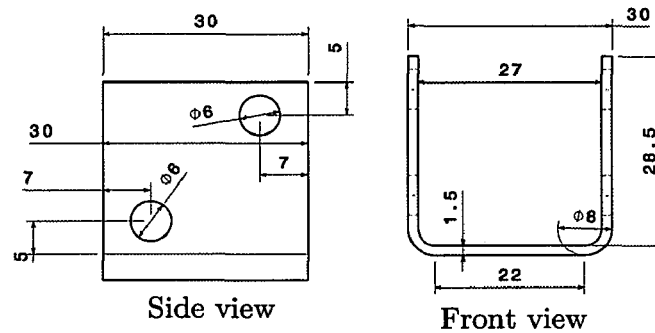


Figure 4.28: geometry of the double U specimens.

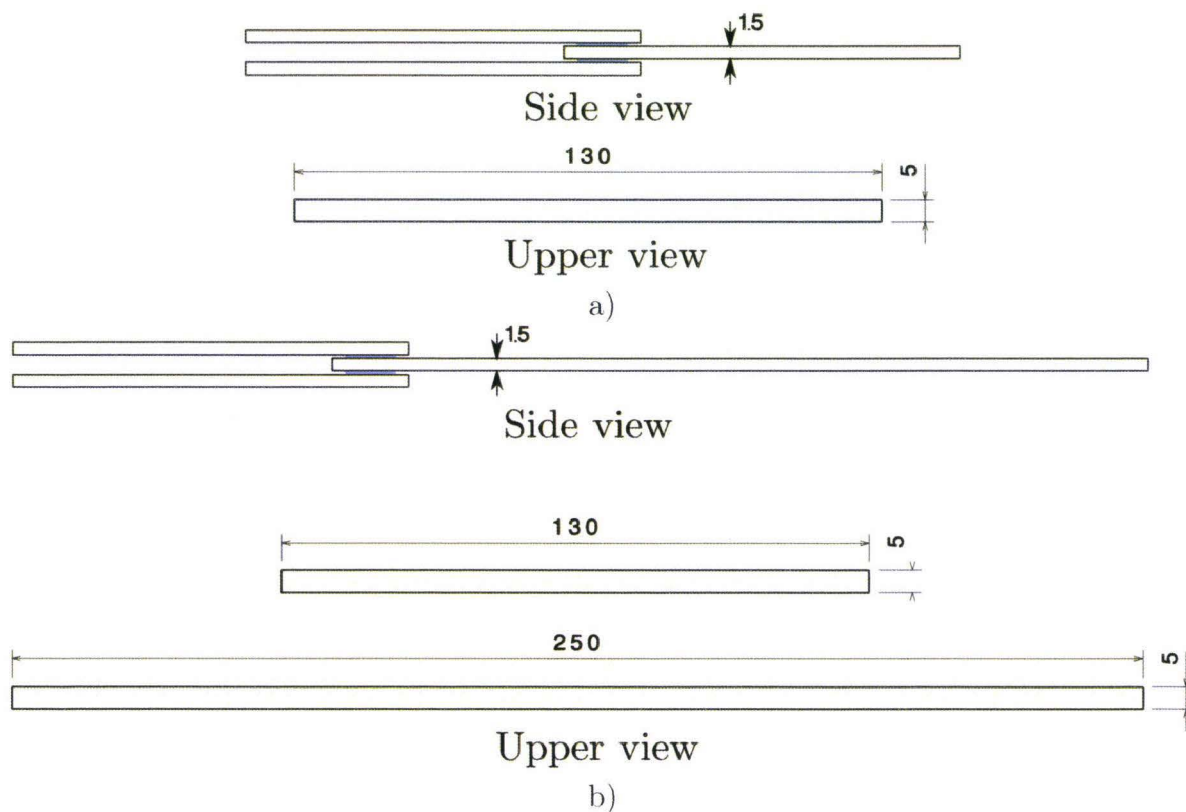


Figure 4.29: geometry of the double lap joints specimens a) in static and b) in dynamic.

In opposition of the double shear lap joint which are directly clamped in the grip of the static/dynamic machine, the double U specimens need a special equipment. This special equipment is composed of steel blocks on which the specimens are screwed and two steel plates (in multiphase 800) from which the loading is carried out (Figure 4.30). As shown in Figure 4.30, the link between the steel block and the steel plates is realized with only one rotational axis. The advantage of this rotational axis is to limit the moment brings to the specimen by the loading. To investigate the effect of strain rate on the failure in assemblies two different loading rates are applied on the previous specimens. The corresponding mean strain rate in the bonded joints are computed with equation 4.37 and are summarized in Table 4.3.

$$\dot{\epsilon}_{mean} = \frac{v}{L} \quad (4.37)$$

where v is the nominal loading speed and L the length of the bonded joint in the loading direction as shown in Figure 4.31.

Even if the strain rates in static are different for the tensile and shear loadings, this difference is considered as negligible due to the low sensitivity of the adhesive on this strain rate range.

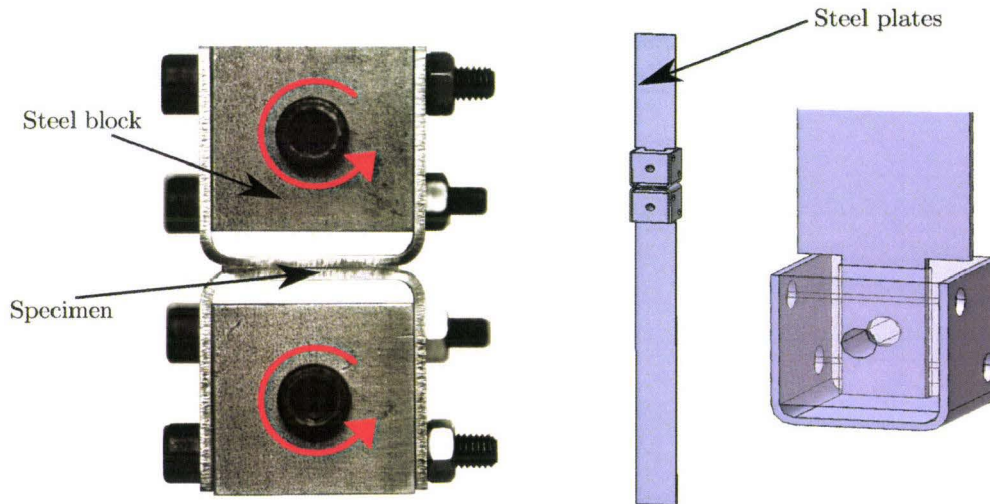


Figure 4.30: presentation of the special equipment needed for the tensile tests.

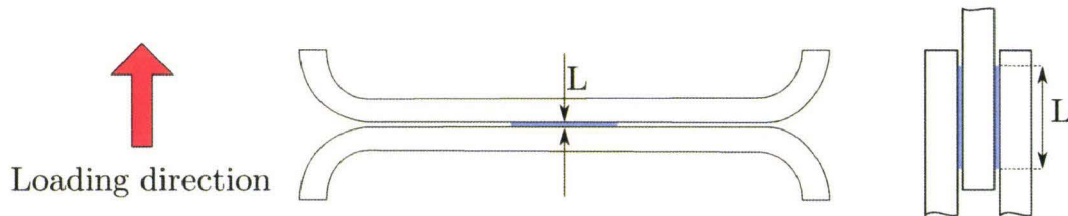


Figure 4.31: illustration of the length used for the strain rate calculation.

	Nominal loading speed	Mean strain rate (in s^{-1})
Double U	$1 \text{ mm} \cdot \text{min}^{-1}$	$5e^{-2}$
Double U	$48 \text{ mm} \cdot \text{s}^{-1}$	160
Double lap joint	$1 \text{ mm} \cdot \text{min}^{-1}$	$2e^{-3}$
Double lap joint	$1.6 \text{ m} \cdot \text{s}^{-1}$	160

Table 4.3: Loading rate and corresponding strain rate.

4.4.3.2 Failure initiation identification and results

Before to present the results in terms of failure initiation criterion, the identification protocol has to be described. The opening and sliding displacements at failure initiation needed in the macroscopic model are identified using 2D Digital Image Correlation. An illustration of measurement protocol is given in Figure 4.32a for the tensile tests and in Figure 4.32b for the shear tests.

Even if the tensile and shear are supposed as pure tests, the counterpart of the opposite displacements (i.e sliding in tension and opening in shear) are taken into account in the measurements thanks to the D.I.C. technique.

As the detection of crack initiation is difficult in this configuration (i.e. small thickness

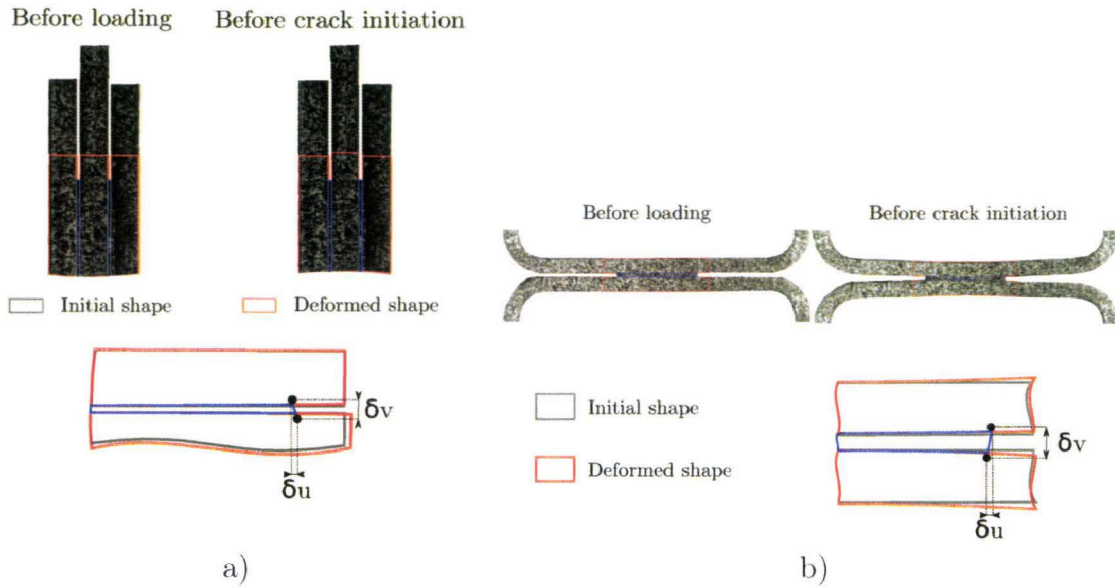


Figure 4.32: illustration of measurement protocol for a) tensile tests and b) shear tests.

of joints and low pixel resolution) the opening and sliding displacements are computed on 4 pictures in which the crack initiates. As Figure 4.33 shows a mean strain and its standard deviation is then computed with the different data.

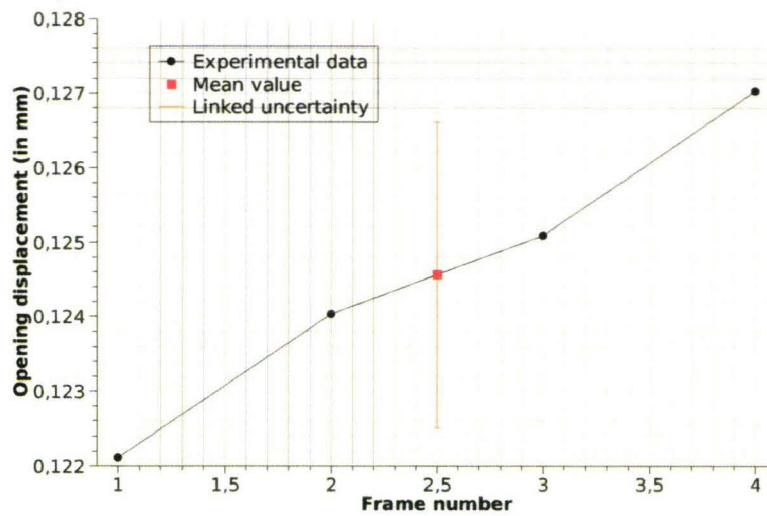


Figure 4.33: illustration of initiation displacements computation.

The results in terms of opening and sliding displacements for both tensile and shear tests are presented in Figure 4.34.

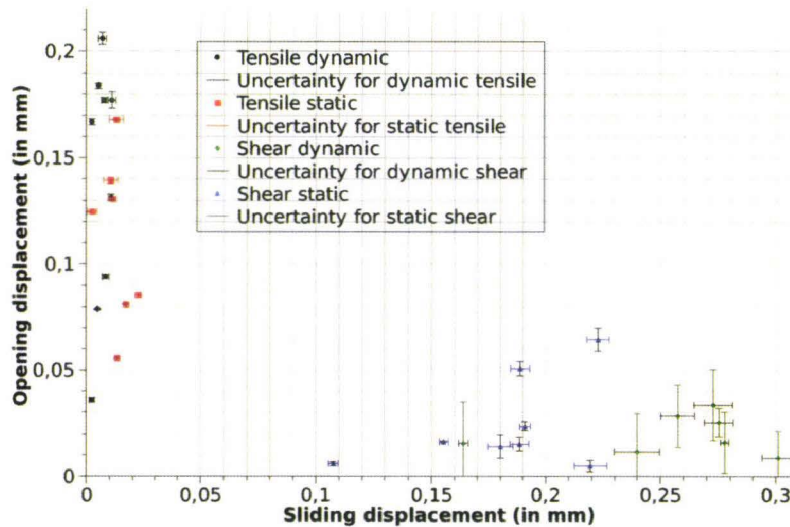


Figure 4.34: results in terms of opening and sliding displacements for the different strain rates.

In opposition of the tests on bulk specimens, the strain rate sensitivity on the tensile results is clearly visible. This un-expected finding can be explained by the triaxiality stress ratio presents in the bonded joints. The Figure 4.35 shows the results of a Finite Element simulation of the double U test. As shows in Figure 4.35a, the triaxiality stress ratio is very heterogenous inside the bonded joint. The particular case of the edge of the bonded joint which is plotted in Figure 4.35b, the triaxiality stress ratio is always greater than 0.5. The experiments on bulk specimens have shown that the strain rate sensitivity decreases with higher triaxiality stress ratio, this proves that results in tension for assemblies are not strain rate sensitive due to the geometrical effect on the edge of the bonded joint.

As for the tensile tests, the results in terms of opening and sliding displacements for the shear tests are very surprising due to the opposite tendancy observed in Figure 4.34. The opening and sliding displacements seem to increase with the strain rate but whitout informations on the behaviour and failure of the adhesive under dynamic shear loading it's not possible to conclude on this aspect. Even if this results are not yet explained, a description of the heterogeneity of the triaxiality stress ratio in double lap joint tests is given in Figure 4.36.

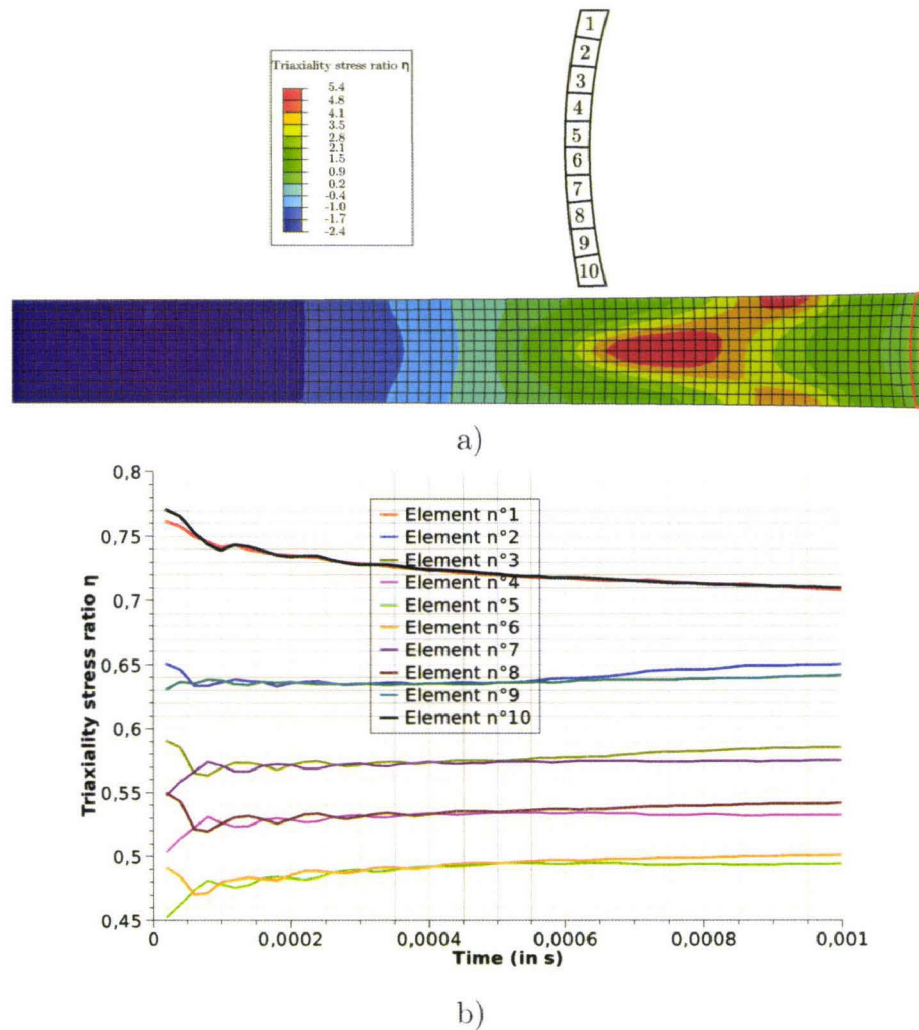


Figure 4.35: a) cutted view through the thickness of the bonded joint in tension and b) evolution of the triaxiality stress ratio in function of the time.

As for the double U specimens, the triaxiality stress ratio is very heterogenous inside the bonded joint (Figure 4.36a) and its evolution in function of time shown in Figure 4.36b proves that its magnitude is never to 0. So as the triaxiality stress ratio is mainly greater than 0.4 the geometrical effects should be dominant.

As the geometrical effects are suspected to be predominant, the final failure initiation model is then identified on the static experimental data as shown in Figure 4.37. The identification of the initiation criterion returns δ_n equal to $103 \mu_m$ and δ_t equal to $226 \mu_m$.

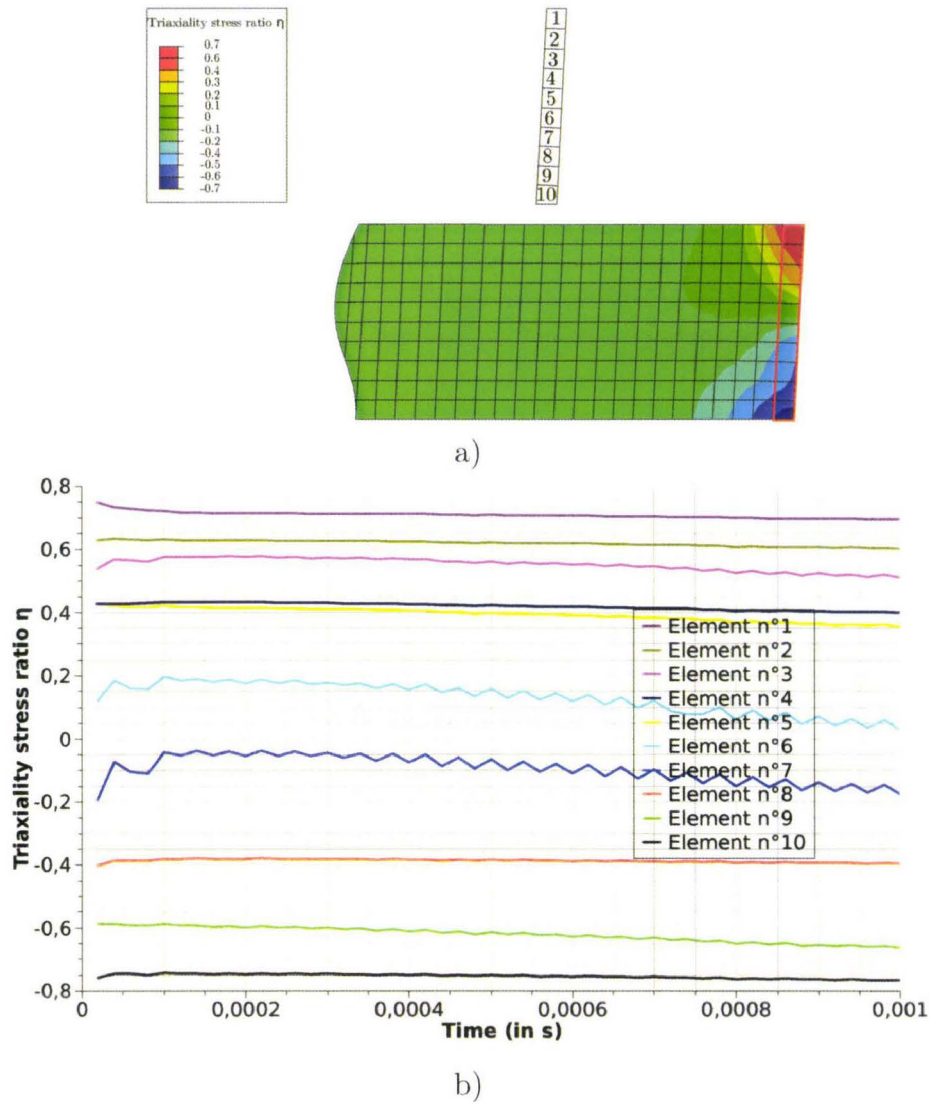


Figure 4.36: a) cutted view through the thickness of the bonded joint in shear and b) evolution of the triaxiality stress ratio in function of the time.

4.4.3.3 Crack propagation identification and results

The crack propagation is identified directly on the image sequence captured by the CCD/CMOS captor. In these sequences, the visible crack tip is followed on the different images as shown in Figure 4.38. Although the crack tip displacement is not straight in the middle of the bonded joints only the projection of this displacement on the x axis (the width of the bonded joint) is taken into account (Figure 4.39).

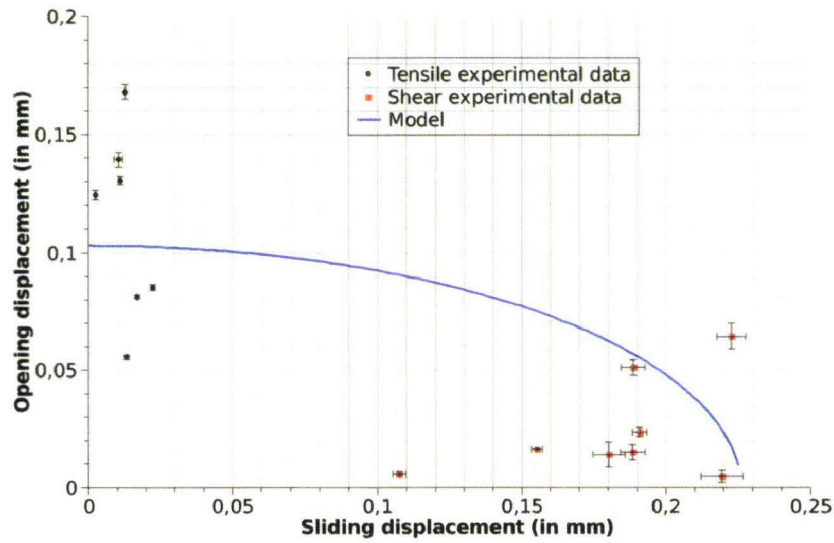


Figure 4.37: identification of the failure initiation criterion.

Specimen with cracks

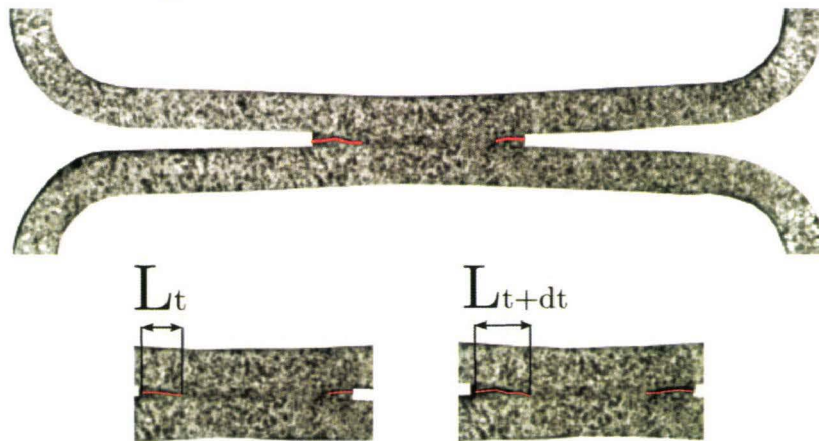


Figure 4.38: crack tip displacement identification.

Of course all these measurements are only valid if the crack tip is considered as straight as shown in Figure 4.40.

Due to the complexity of the identification of the crack tip displacement, these measurements are only limited to the double U tests. As a consequence of this choice the crack speed computed may be overestimate for the mode II/III crack propagation.

The crack tip displacements identified on a selection of specimens are shown in Figure 4.41. These curves show high dispersive responses in terms of slope which translate different crack propagation speed but also different crack propagation progress. For example on the 1st crack of the specimen n^o7, the crack displacement is quasi constant and could be associated to elastic fracture mechanics. In opposite the major part of the studied

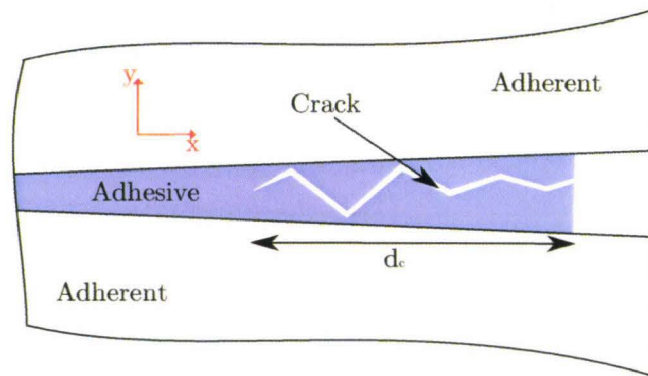


Figure 4.39: illustration of the crack tip displacement measurement.

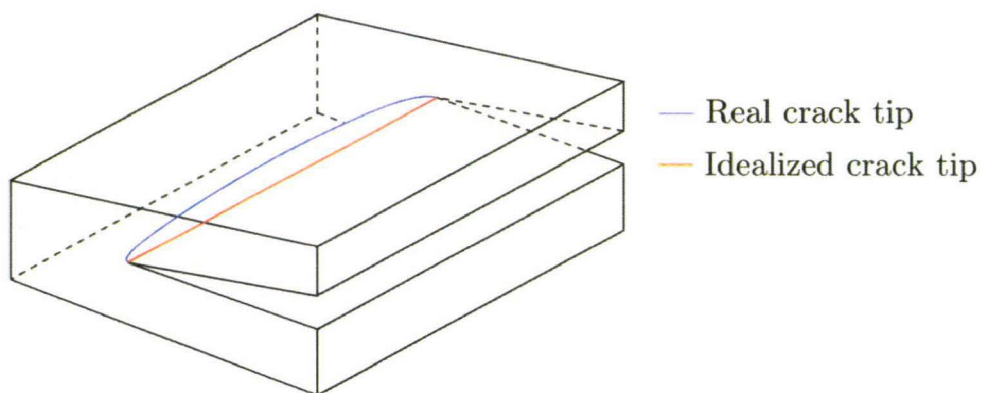


Figure 4.40: idealization of the crack tip.

specimens show a discontinuous crack propagation which is related to inelastic fracture mechanics phenomena.

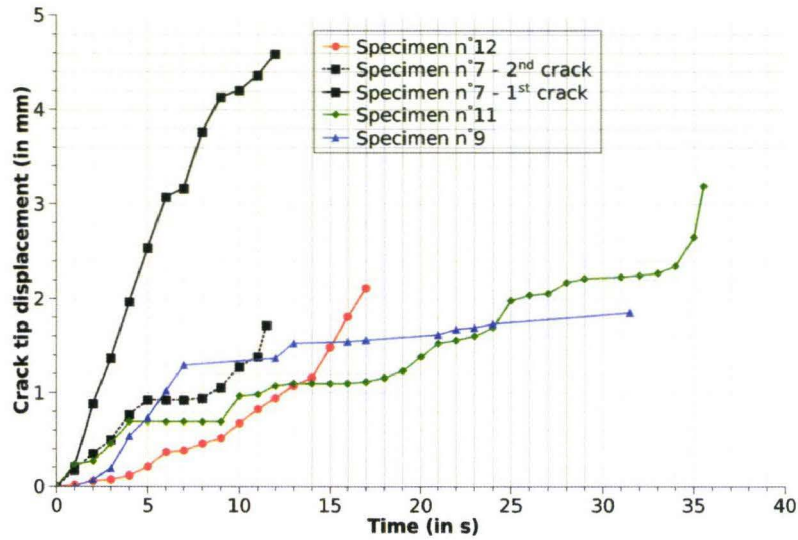


Figure 4.41: results in term of crack tip displacements.

From the curves presented in Figure 4.41 the crack propagation speeds are extracted by realizing linear interpolation as shown in Figure 4.42. On each tests 3 crack propagation speeds are identified following the previous principle.

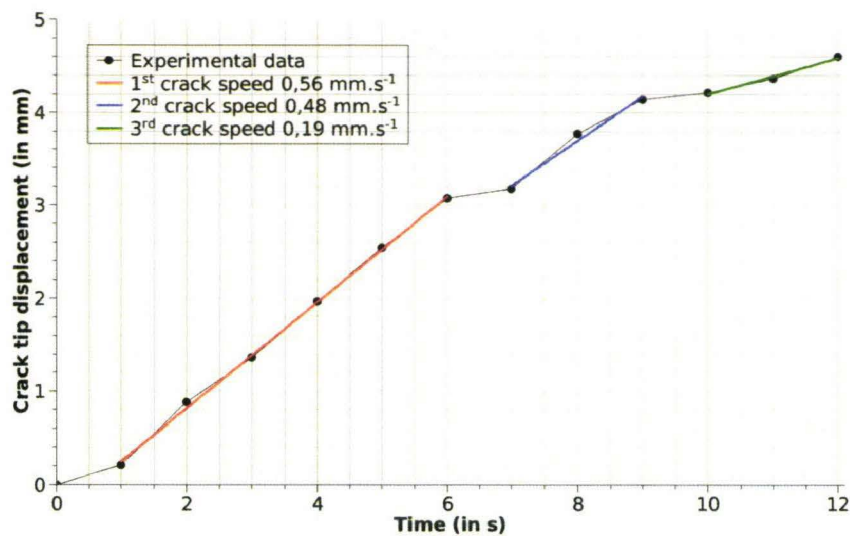


Figure 4.42: crack propagation speed identification.

Due to the fact that the crack propagation speed is dependent of the loading speed of the bonded joints (i.e. more faster is the test more faster is the crack propagation) the crack propagation speed has to be identified in the function of the equivalent opening speed (equations 4.34,4.36). Unfortunately this equivalent opening speed is also function of the width of the bonded joints and the double U do not have the same width so a normative variable has to be chosen. Finally, the normative variable chosen is the ratio between

the equivalent opening speed and the width of the bonded joint. With this variable the evolution of the crack propagation speed is then plotted in Figure 4.43.

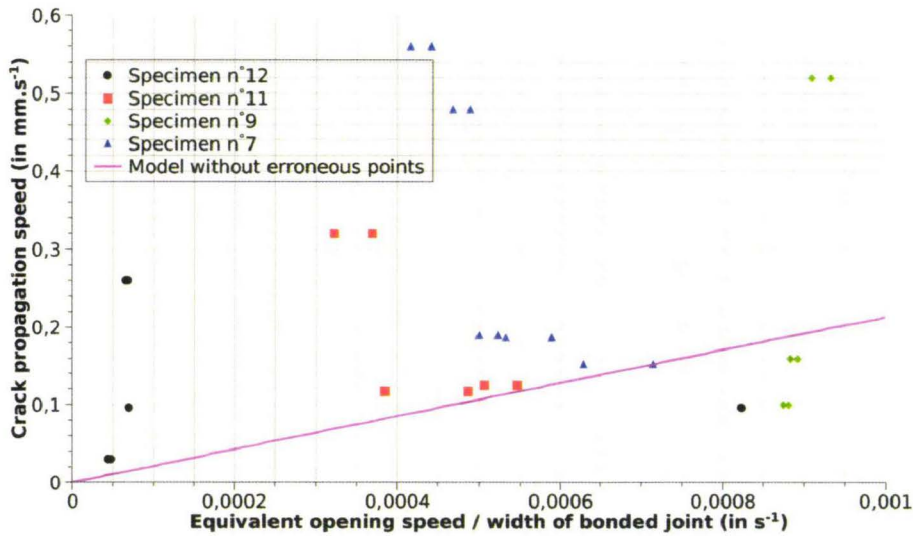


Figure 4.43: crack propagation speed in function of the normative variable.

By discarding the computed crack propagation speed which seem to be erroneous (greater than 0.2 mm.s^{-1}), the ratio h (equation 4.33) is then equal to 213 for a bonded joints of 1 mm.

4.5 Conclusions

This chapter brings the complete description of the macroscopic approach used in this thesis. This model is based on the time step formulation of a classical cohesive element. In addition of the existing cohesive element of the litterature, this model brings the possibility to represent the different behaviour in tension and compression in terms of elasticity as well as the plasticity. It also provides a simplified visco-plasticity enhanced by a damage model. The failure initiation is tackled by a criterion based on the opening and sliding displacements which initiate a crack on an edge of the bonded joint. The element elimination is tackled using an innovative technique which represent the elimination as a crack propagation through the element. An experimental technique to propagate a crack is also present but is very limited for the moment due to some problems linked to the current finite element software. The behaviour properties of this model are identified on the previous bulk specimens (Chapter 2) but with a simplified analysis. Finally the failure initiation and crack propagation properties are identified on assemblies using 2D Digital Image Correlation technique.

4.6 Models parameters summary

Elasticity	Tension	E (in MPa)	3000		
	Compression		2000		
Yield stress	Model	$\sigma_y = A + B \cdot \dot{\epsilon}^n$			
	Parameters	A (in MPa)	B (in MPa)	n	
	Tension	28	6.7	0.5	
	Compression	58	1.5	0.3	
Tangent moduli	Model	$E_T = a_{t_0} + a_{t_1} \bar{\epsilon}_p + a_{t_2} \bar{\epsilon}_p^2 + a_{t_3} \bar{\epsilon}_p^3$			
	Parameters	a_{t_0} (in MPa)	a_{t_1} (in MPa)	a_{t_2} (in MPa)	a_{t_3} (in MPa)
	Tension/ Compression	27	0.03	-9e-6	1.3e-9
	Shear	0.86*Tension/compression			
Damage	Model	$d_0 + d_1 \cdot (1 - e^{-d_2 \cdot \epsilon_p n})$			
	Parameters	d_0	d_1	d_2	
		-0.3	0.8	20	
Failure	Model	$\lambda_{init} = \sqrt{\left(\frac{\delta_n}{\delta_{n_{crit}}}\right)^2 + \left(\frac{\delta_t}{\delta_{t_{crit}}}\right)^2 + \left(\frac{\delta_\tau}{\delta_{\tau_{crit}}}\right)^2} \geq 1$			
	Parameters	$\delta_{n_{crit}}$ (in μm)		$\delta_{t_{crit}}$ (in μm)	
		103		226	

Figure 4.44: summary of macroscopic model parameters.

Modeling of bonded structures

Contents

5.1	Presentation of the different structures	104
5.2	Prerequisite to the finite element modeling of bonded structures	105
5.3	High strain rate double U test	108
5.4	Dynamic flexure test	111
5.5	Dynamic axial crushing test	117
5.6	Proposition of modeling strategy	125

Resume

The aim of this chapter is to present numerical validations of the mesoscopic and macroscopic finite element models. These validations are carried out on three different experimental tests. These experimental tests are based on gradually complex loadings in order to check the accuracy of the proposed models on different levels of difficulty. From these results, an adapted modeling strategy is then proposed.



5.1 Presentation of the different structures

To provide a pertinent evaluation of the mesoscopic and macroscopic models the correlation between experimental and numerical responses are realized for different loadings. The accuracy of both models is checked with a high strain rate double U test which brings a mode I load on the bonded joint (Figure 5.1a). An innovative test called dynamic flexure test is designed to bring a mode I/II load on the specimen at high strain rates (Figure 5.1b). The combination of mode I/II and mode III is given by a dynamic axial crushing of crashboxes (Figure 5.1c). These crashboxes are realized with different assembly techniques as mentioned in Chapter 1. To keep a continuity between the identification of the macroscopic failure criterion, the same grade and thickness of steel is chosen, so a DP 600 with a thickness of 1.5 mm.

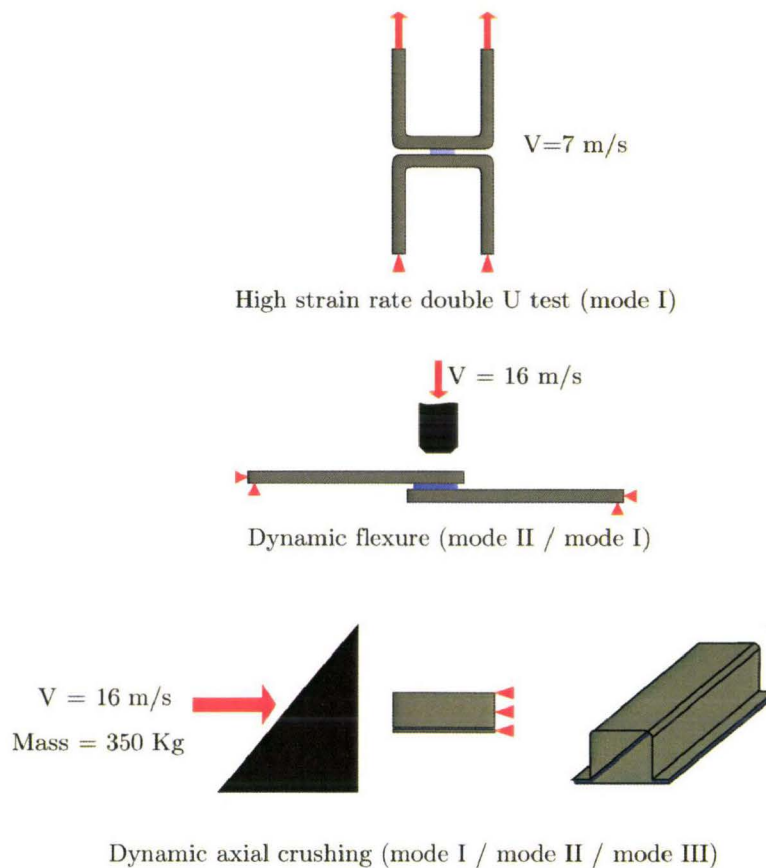


Figure 5.1: description of experiments and load complexity.

An analysis of the ratio between the quality of the results and the computation times is also given for each load complexity and a modeling strategy of bonded structures is finally given.

5.2 Prerequisite to the finite element modeling of bonded structures

5.2.1 Mesh size and link between steel and adhesive

As explained in Chapter 3, the steel adherents are modeled with shell elements. These shell elements are chosen as reduced integration and the default option with ABAQUS explicit is used for the thickness integration (5 points and the Simpson rule). The mesh size of the steel adherents is adapted to the experiments and size of the elements are summarized in table 5.1.

Experiment	Element size (mm)
Double U	0.5
Dynamic flexure	0.5
Dynamic crushing	5

Table 5.1: summarize of the shell element sizes.

In addition on the steel mesh size, some informations have to be given on the mesh size of the adhesive. As for the steel shells, the size of the volumic or macroscopic elements are adapted to the experiments (Table 5.2). As the opposite of the shell elements which are chosen as square, the volumic or macroscopic elements are not purely cubic. This choice is realized only to limit the number of elements in the F-E simulations.

Experiment	1 st side (mm)	2 nd side (mm)	thickness (in mm)
Double U	0.5	0.5	0.3
Dynamic flexure (1 element)	0.5	0.5	0.3
Dynamic flexure (3 elements)	0.5	0.5	0.1
Dynamic crushing (1 element)	5	5	0.3
Dynamic crushing (3 elements)	5	5	0.1

Table 5.2: summarize of the adhesive element sizes.

As mentioned in Chapter 3, the steel adherents are modeled with the neutral axis of the shell elements so an offset between this axis and top surface of the adhesive element is made. This offset is made for the mesoscopic model with a tie constraint available in ABAQUS explicit which keep a constant distance between the shell and the volumic element (Figure 5.2). For the macroscopic model, the use of user element in ABAQUS does not allow the tie constraint so another technique is required. To numerically 'bond' the macroscopic element to a shell element, an artificial link between coincident nodes is realized by coupling the translationnal degrees of freedom of the shell nodes to the volumic nodes (Figure 5.2).

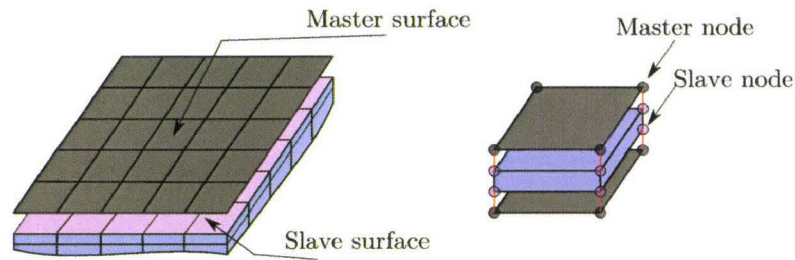


Figure 5.2: numerical link between steel and adhesive.

5.2.2 Steel material properties

For all the computations, the steel material (DP 600) is considered as visco-plastic with true stress / true plastic strain curves given on a tabulated way (Figure 5.3). Its plasticity is computed following the classical von Mises plasticity (J_2 plasticity) theory.

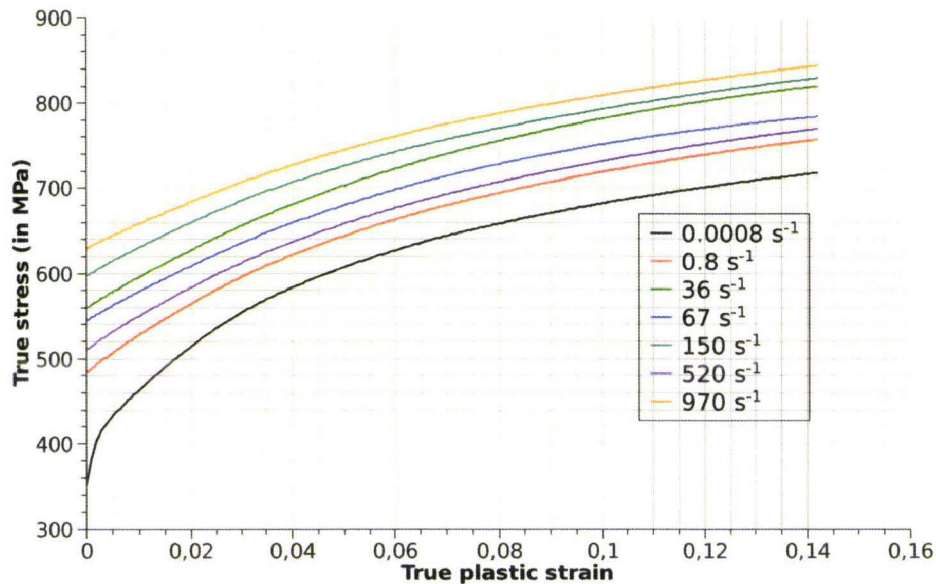


Figure 5.3: true behaviour laws for the DP 600 steel.

5.2.3 Failure criterion of adhesive in mesoscopic model

As for the mesoscopic model, a mesh sensitivity through the thickness of the bonded joint is done. An evaluation of the failure model parameters on the failure criterion have to be made. Indeed, it is a well-known fact that the failure strain is dependent on the length of the element in F-E simulations. By using D.I.C. techniques to identify the failure strains, this problem is also present. The step size (distance between two correlation zones) of D.I.C. is then equivalent to the finite element length. An illustration of the problem linked to the step size is given in (Figure 5.4).

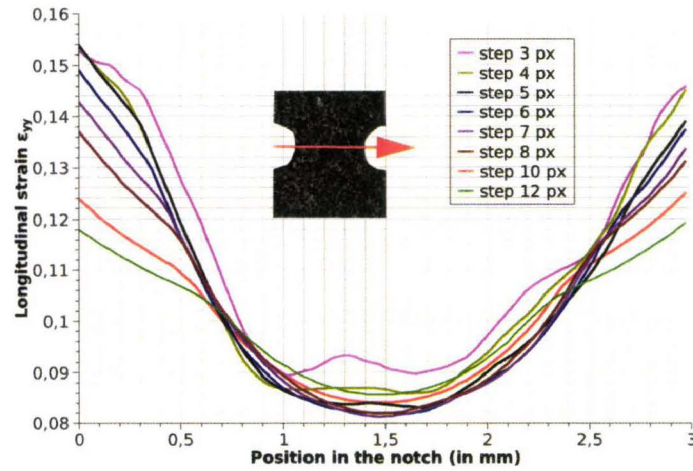


Figure 5.4: effect of step size on the failure strain computation in D.I.C.

As the failure criterion identified in Chapter 2 is based on 0.3 mm step size, a ratio has to be applied on it so as to be valid with smaller elements. This ratio is determined by identifying the effect of the step size on an experimental strain distribution and is applied on the a_f function of the failure criterion (2.31) (Figure 5.5). The strain rate dependency described by the b_f function is by definition not affected by the step size. Finally different parameters are found and have to be used in adequation of the mesh size.

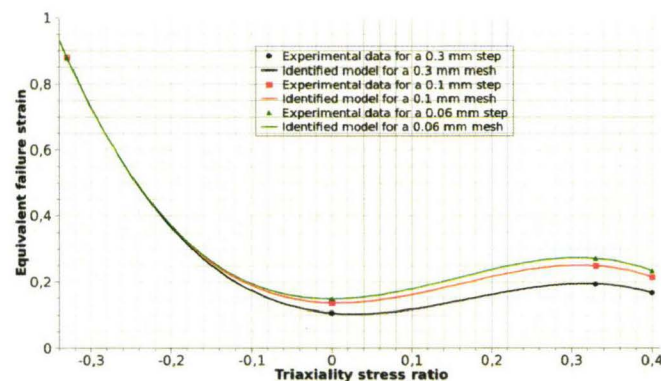


Figure 5.5: evolution of the a_f function in function of the mesh size.

5.3 High strain rate double U test

5.3.1 Description of experiments

The mode I test is achieved on the same double U geometries than in Chapter 4. The main difference is focused on the loading speed, which is closed to 7 m.s^{-1} . To obtain this loading speed a set of direct tension Hopkinson bars is used (Figure 5.6). These Hopkinson bars are constituted of two steels bars loaded on the end of the input bar by an tubular impactor made in aluminum. The force and displacements measurements are achieved through the strain gages bridges placed on both input and output bars.

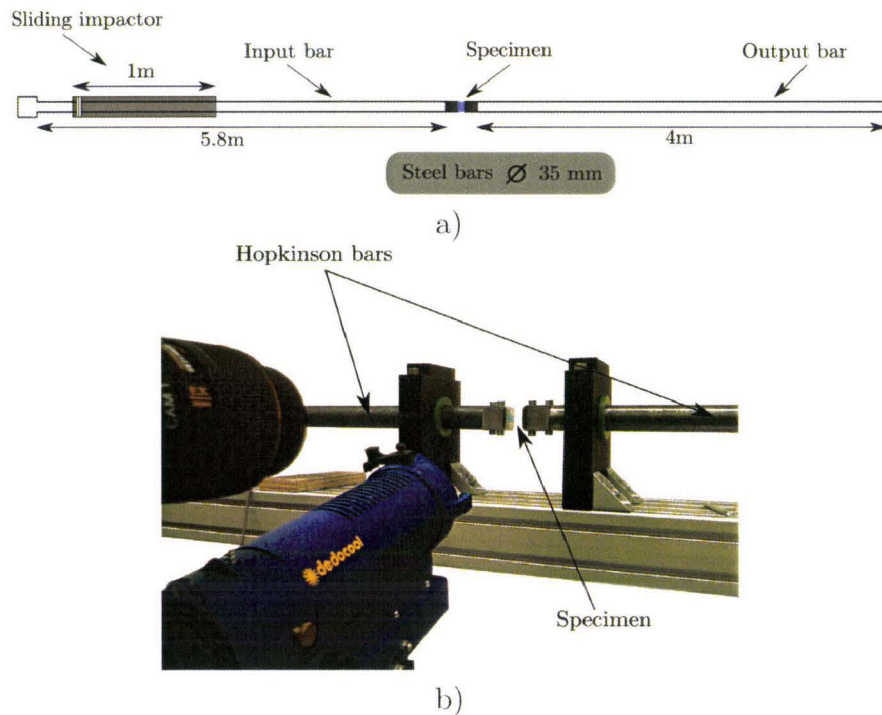


Figure 5.6: presentation of the Hopkinson bars.

5.3.2 Description of numerical simulations

Due to the symmetries of the system, only a quarter of the specimen is modeled (Figure 5.7). On this model, the lower part is considered as fully fixed i.e. all degrees of freedom are equal to zero. The upper part of the model is loaded by a speed ramp (Figure 5.8). This ramp is identified on the difference between input and output bars speed.

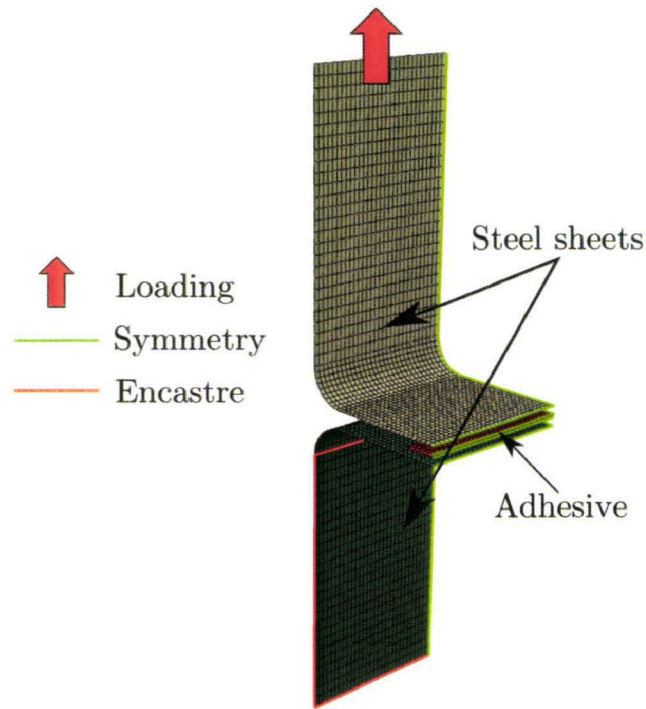


Figure 5.7: FE model of the double U test.

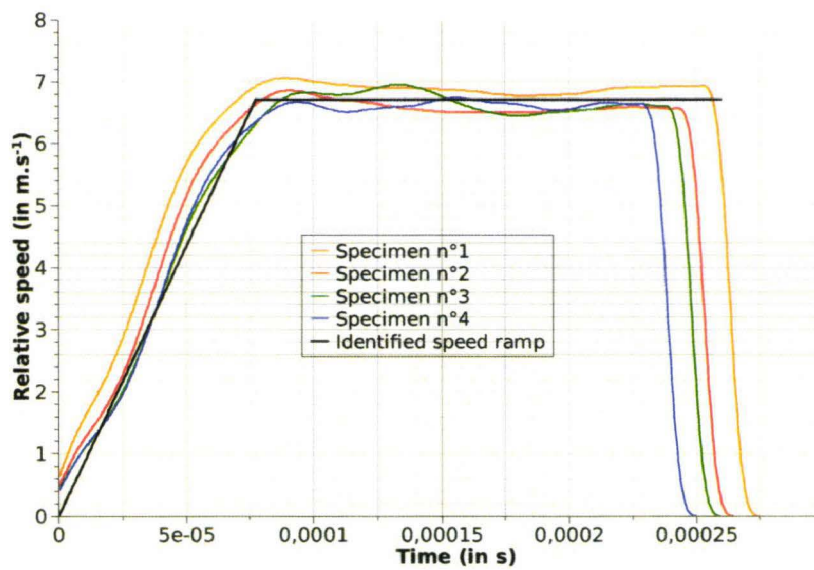


Figure 5.8: identification of the speed ramp.

5.3.3 Correlation between numerical and experimental results

To correlate the numerical results to the experimental ones, only the force displacement curves are used due to the complex specimens geometries. A major difference is observed between the experimental and numerical curves (Figure 5.9). This difference is not a

numerical error but comes from the experiments. Indeed, a geometrical discontinuity is present between the specimen and the input and output bars (Figure 5.10). These geometrical discontinuities imply a lower force rise in the specimen.

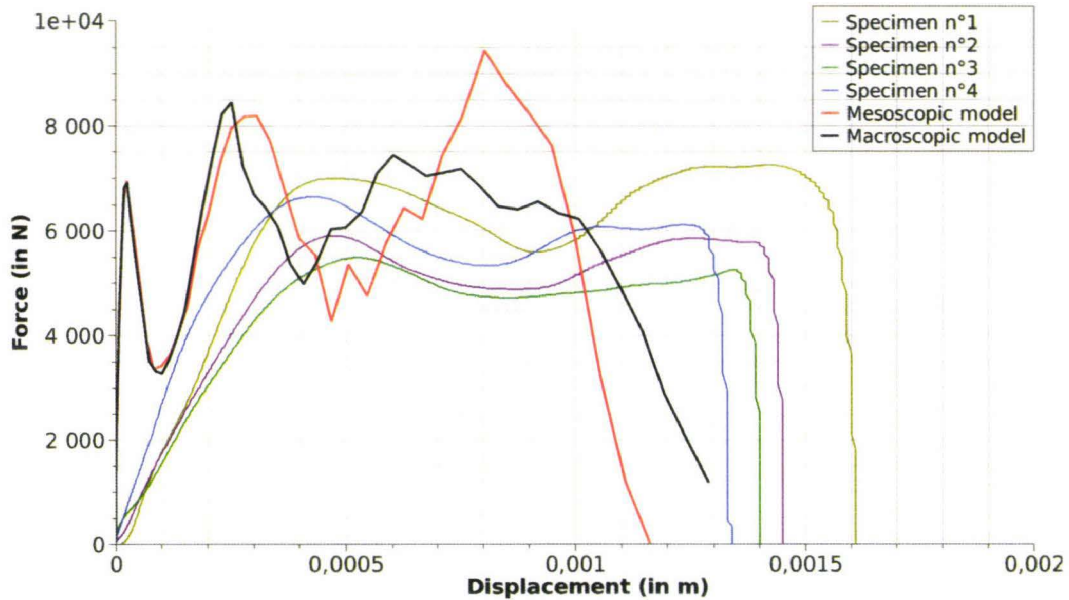


Figure 5.9: experimental and numerical force displacement curves.

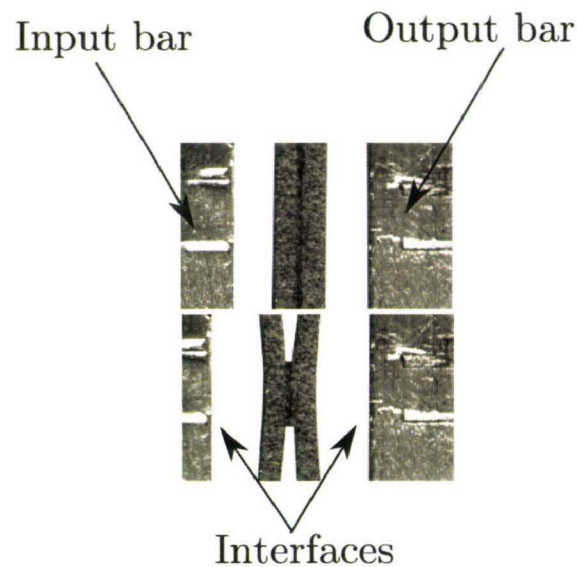


Figure 5.10: discontinuities problem between specimen and Hopkinson bars.

By skipping this force rise problem, the numerical and experimental curves show a good correlation (Figure 5.11). For both macro and mesoscopic models, the average force during the test is well described. In addition, the failure of the specimen appears to be well predicted on the global displacement value.

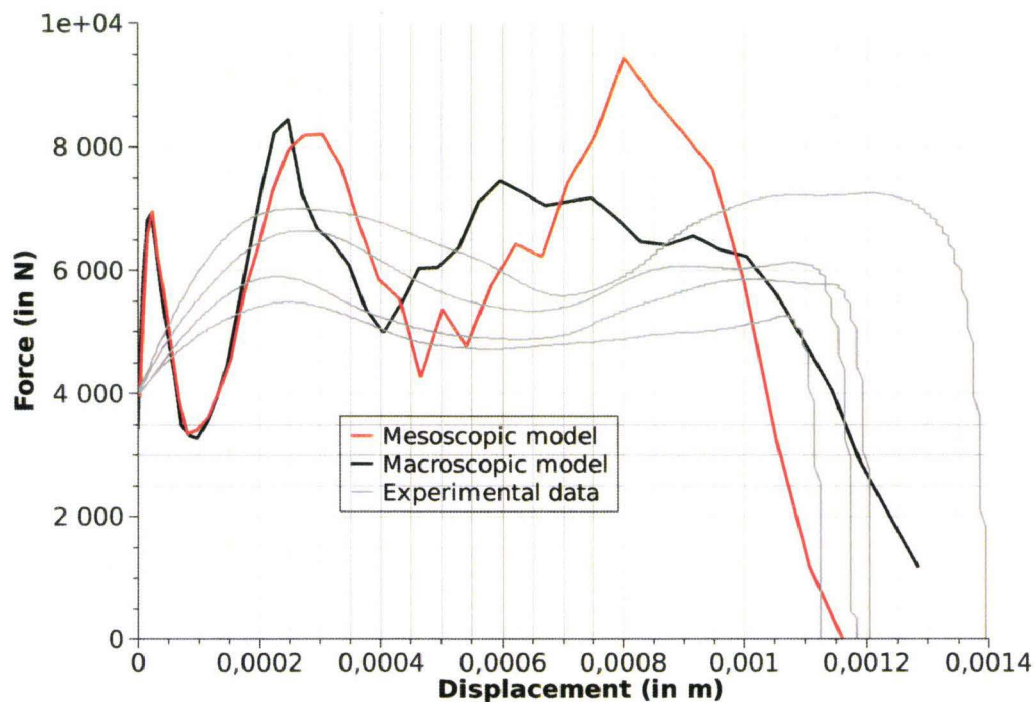


Figure 5.11: experimental and numerical curves for force displacement.

5.4 Dynamic flexure test

5.4.1 Description of experiments

The innovative dynamic flexure test is realized on a ballistic tube (Figure 5.12). The innovation realized here is to use a perforation device for a dynamic flexure test. This flexure test is realized on a normative single-lap joint specimen originally designed to evaluate the shear properties of bonded joints. Specimens which are presented in Figure 5.13, are screwed directly on the steel tube (Figure 5.12). Then the measurement of the force is realized using the elastic wave propagation in the tube. This measurement is achieved using full strain gage bridges, here two bridges are used so as to obtain a double measurement (Figure 5.12). The flexure loading is obtained by an impactor launched through a guide by a compressed air device. The displacement of this impactor is measured by an electro-optical extensometer (Figure 5.12).

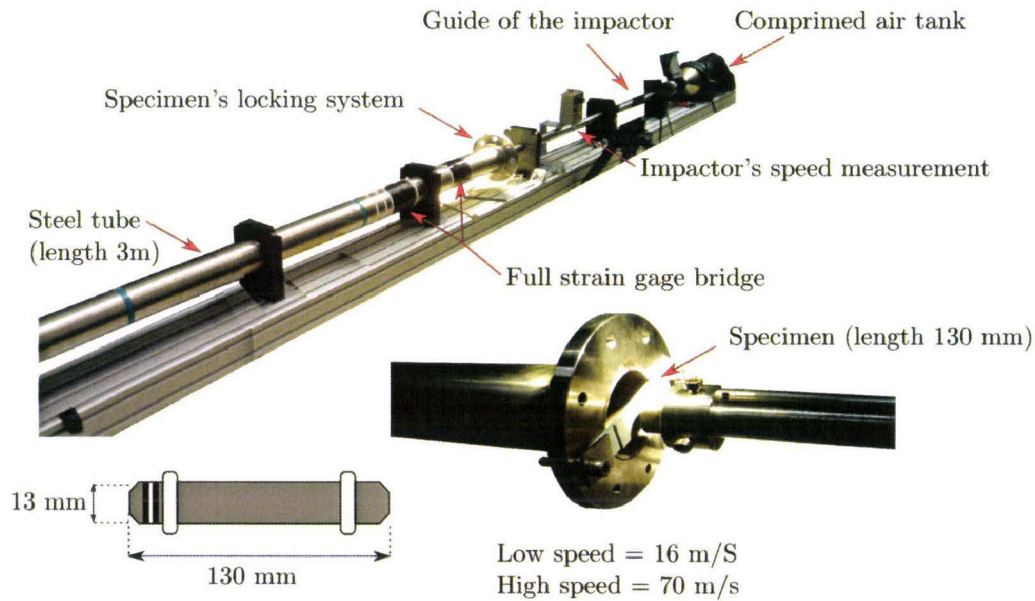


Figure 5.12: presentation of the ballistic device.

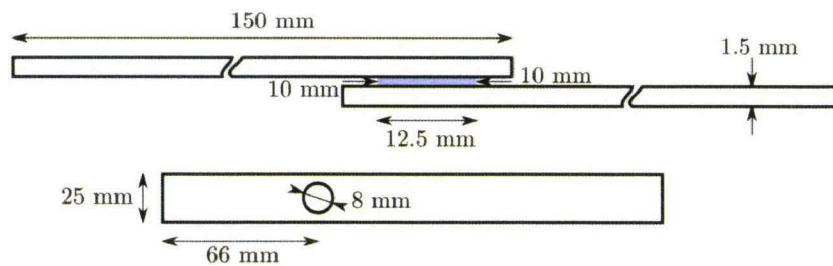


Figure 5.13: geometries of the specimen.

5.4.2 Description of numerical simulations

The proposed model for the dynamic flexure test is described in Figure 5.14. The boundary conditions of the specimen are simplified to a clamped configuration on the internal radius of the tube (red lines). Here again, a symmetry is used to reduce the time of computation (green lines). The impactor is represented by an analytical surface considered as rigid. This impactor is moved by an imposed displacement (measured experimentally) and a mass of 72.65 g is added to represent its real weight. Here again the tangential friction coefficient is set to 0.3 by a penalty method.

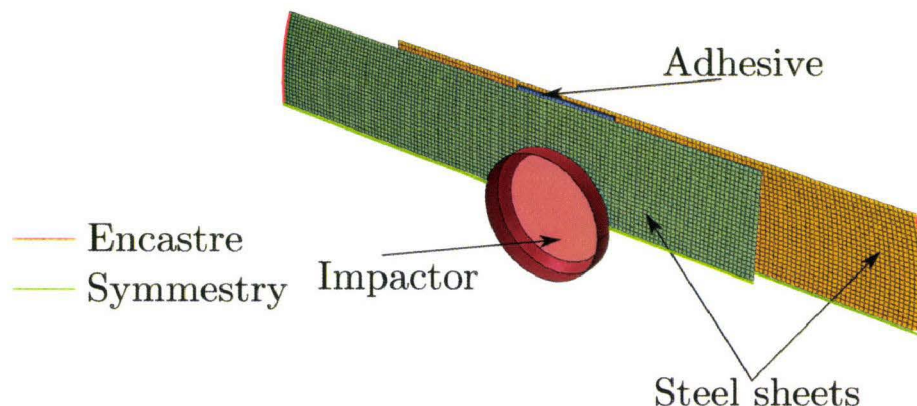


Figure 5.14: dynamic flexure simulation setup.

5.4.3 Correlation between numerical and experimental results

As results on these tests, only the force displacement can be used to correlate the numerical and experimental responses. The numerical forces are computed on the clamped lines of the specimen and a factor 2 is applied to represent the total load of the real specimen. The experimental results in terms of force are very noisy (Figure 5.15) so the correlation is realized on the chosen typical sample. This noisy response is directly related to the geometry of the measurement tube. Indeed, the specimen is clamped to the tube through an holed steel plate which is welded to. All this geometries discontinuities create wave reflexion and then noise on the signal measured by the strain gages.

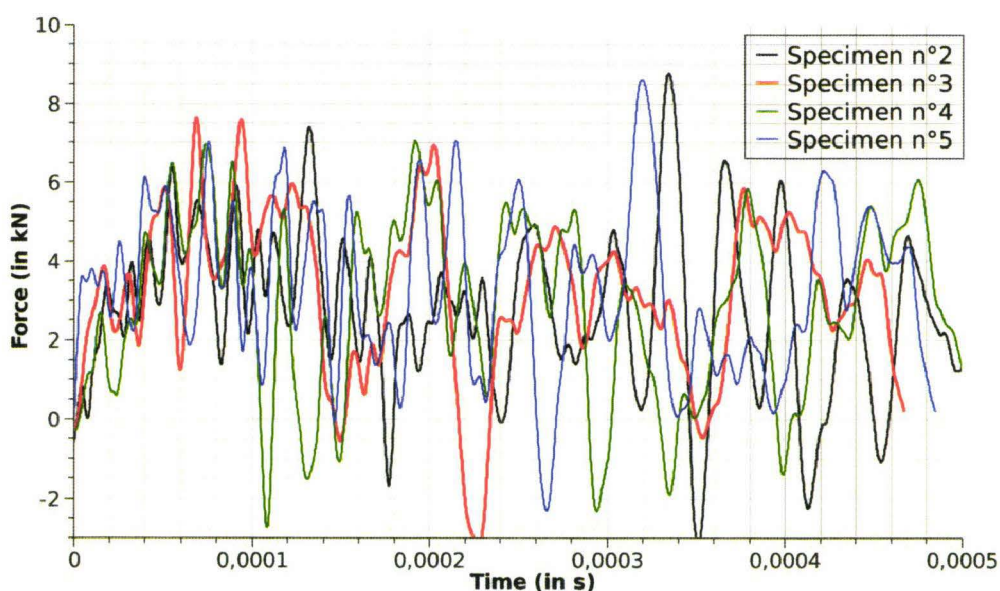


Figure 5.15: experimental forces measured on the tube.

So as to match to the chosen typical sample, its displacement is imposed to the impactor. In order to avoid the numerical problems linked to the explicit schema, a polynomial

approximation is realized on this displacement (Figure 5.16).

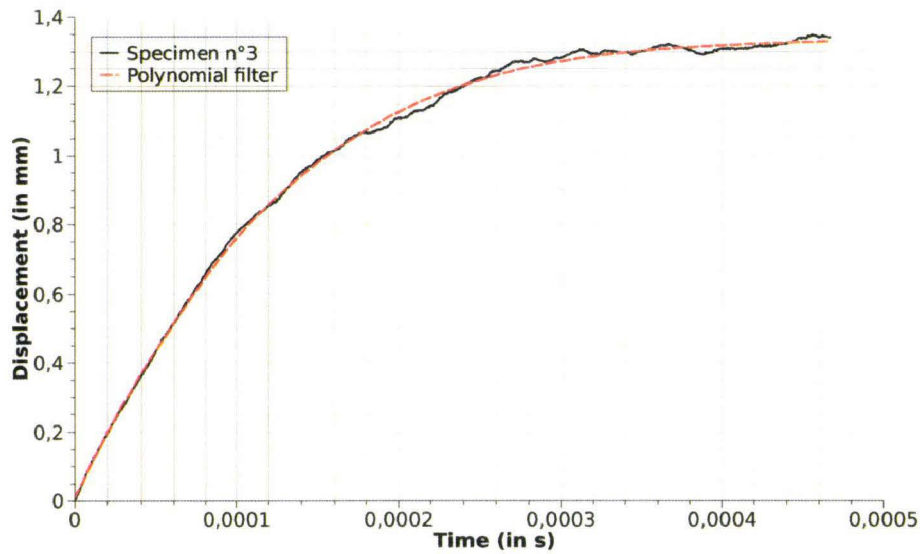


Figure 5.16: filtering of the displacement of the impactor.

For both macro and mesoscopic models, a good correlation is found at the begin of the test (up to $60 \mu\text{s}$) (Figure 5.17). After that only the mesoscopic model is able to predict the good strength of the specimen. The effect of the mesh refinement is detailed in Figure 5.18 in which the difference between an one element through thickness and a 3 elements through thickness is given. From these curves, the effect of the mesh refinement allows a better description of the global response but with an increase of the computation time as it will be discussed later in this paragraph.

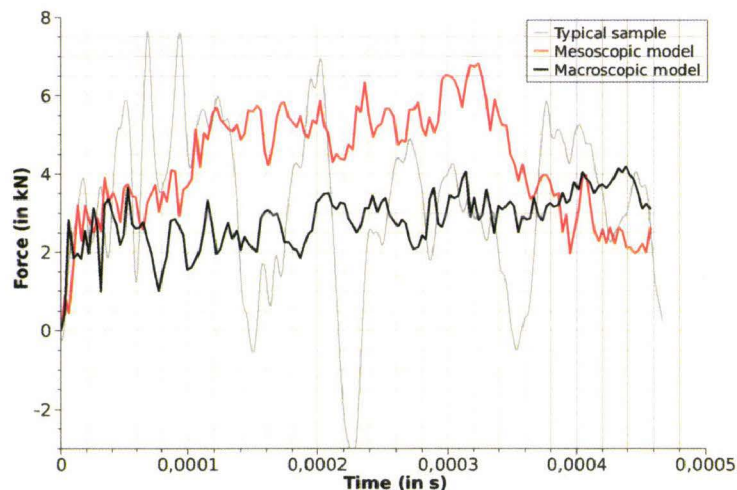


Figure 5.17: comparison between macro and mesoscopic models on the force-time curve of the typical sample.

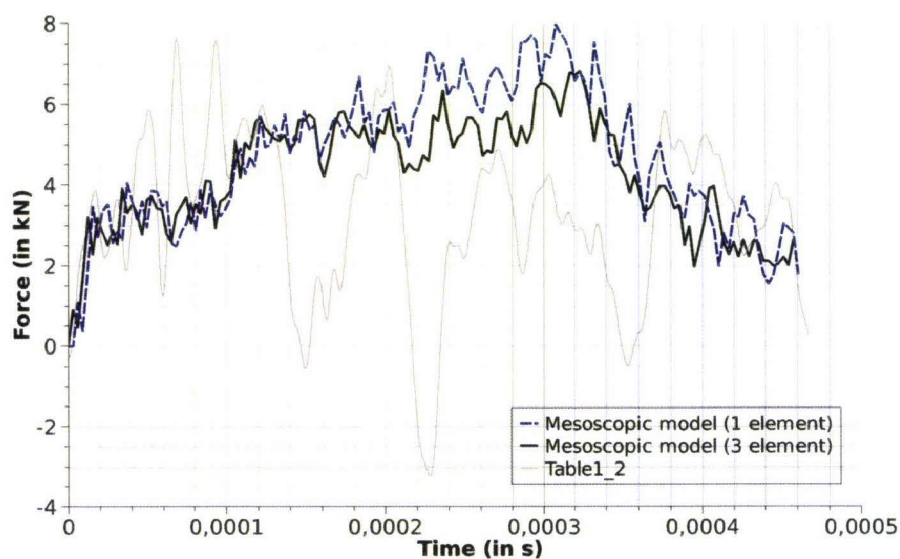


Figure 5.18: effect of the mesh refinement through thickness.

A qualitative study on the failure is also realized on the refined mesh. It appears that the numerical crack initiation is well predicted in terms of geographical position in the bonded joint but also into the thickness (Figure 5.19 , 5.20). The failure initiation into the thickness is correlated with the experimental failure faces which are cohesive superficials.

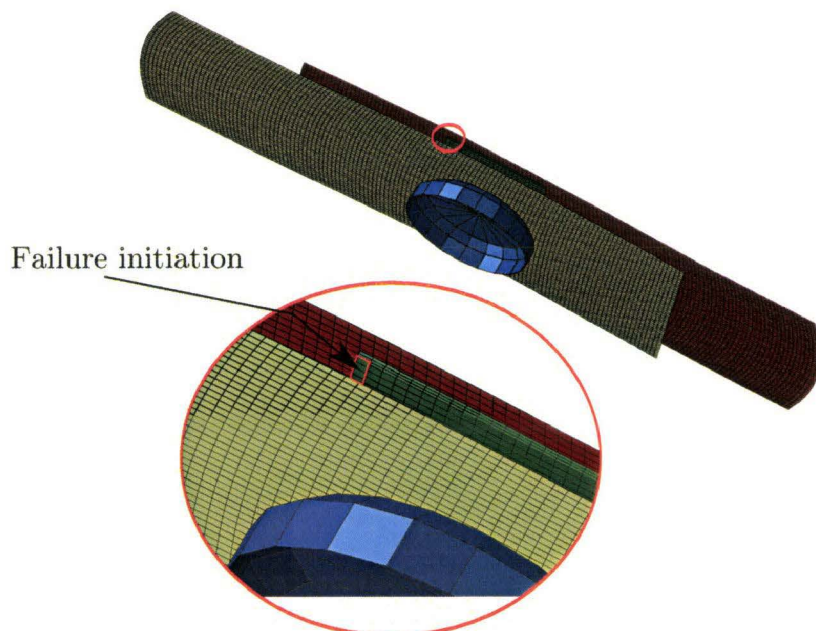


Figure 5.19: numerical crack initiation on the dynamic flexure test.

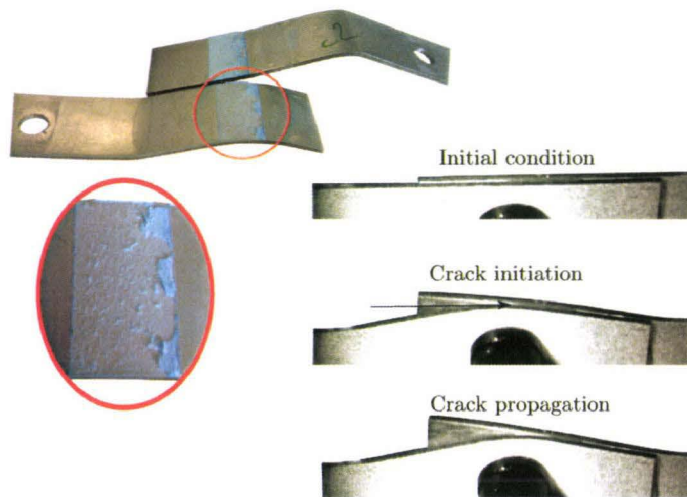


Figure 5.20: experimental crack initiation on the dynamic flexure test.

In addition to the differences highlighted on the previous figures (Figures ??), it is also interesting to compare the computation time between these calculations. Of course, the use of a refined mesh into the thickness brings a better correlation but an increase of 300 % of the computation time is needed compared to 1 element mesh or the macroscopic model (Figure 5.21). The gain in terms of time when using the macroscopic model is very small (a few seconds) in face of the loss of quality in the response.

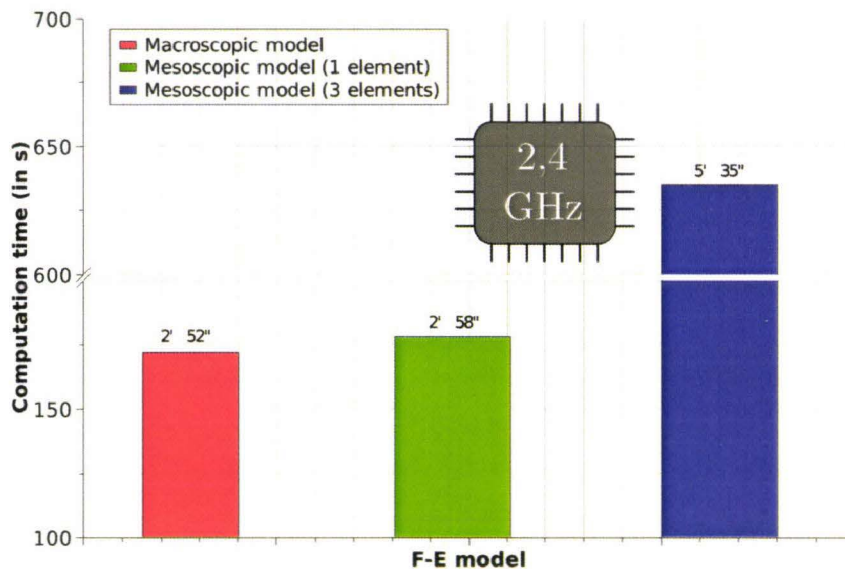


Figure 5.21: summary of the computation times for the different models.

5.5 Dynamic axial crushing test

5.5.1 Description of experiments

The dynamic axial crushing tests are realized at ARCELORMITTAL Maizières les Metz on a middle capacity catapult (Figure 5.22). To obtain a dynamic axial crushing loading, a mass impactor is launched on a rail at $16 \text{ m}\cdot\text{s}^{-1}$ on a crashbox (Figure 5.22). This crashbox is fixed on a rigid wall through the force acquisition system. This system is composed of 4 piezo-electric cells placed in parrallel for a total capacity of 1200 kN. The displacement of the impactor is measured with a laser captor placed on the rigid wall.



Comprimed air tank

Impactor (mass 350 Kg)
speed 16 m/s

Crashbox's locking system

Figure 5.22: presentation of the dynamic axial crushing test.

Three kinds of crashboxes are realized in ARCELORMITTAL Montataire with different combinations of assemblies:

- 10 spotwelds
- 10 spotwelds + bonding
- 5 spotwelds + bonding
- bonding.

Except for the only bonded structures which are realized with a continuum bond line, the spotwelded and bonded crashboxes are realized with a discontinuous bond line (Figure 5.23). This discontinuous bond line is chosen so as to avoid expulsion of matter during the formation of the spotweld. The spotweld of the different crashbox configuration are realized on a Langepin spotweld machine at defined places as shown in Figure 5.24.

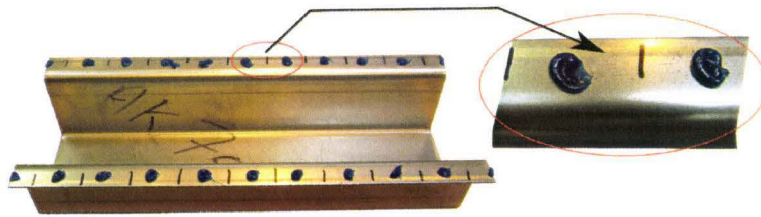


Figure 5.23: discontinuous bond line.

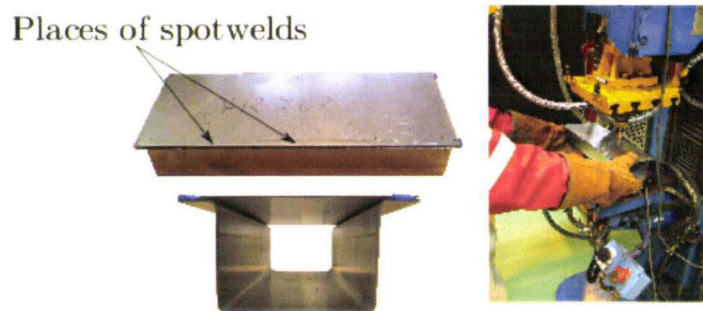


Figure 5.24: spotweld machine and places for spotweld.

5.5.2 Description of numerical simulations

The dynamic axial crushing tests are simulated as shown in Figure 5.25. Only an half of the crashbox is simulated using a symmetry (green line), in terms of clamping a 15 mm length region is clamped (red lines) so as to represent the real conditions. The mass impactor is represented by an analytical surface considered as rigid. This impactor is launched with an initial velocity of 16 m.s^{-1} and a mass of 175 kg is added to represent its real weight. Here again the tangential friction coefficient is set to 0.3 by a penalty method. As no failure is observed for the different spotweld,s a simple tie between the upper and lower shell steel nodes is realized (Figure 5.26). The simulations of the spotwelded and bonded specimens are realized with only one element through the thickness except for the only bonded specimens on which a sensibility of the mesh refinement is performed.

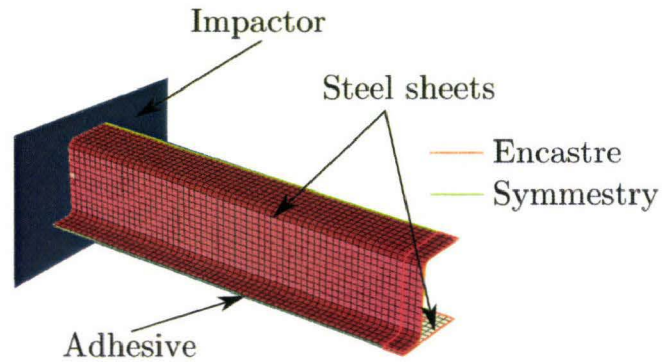


Figure 5.25: dynamic axial crushing simulation setup.

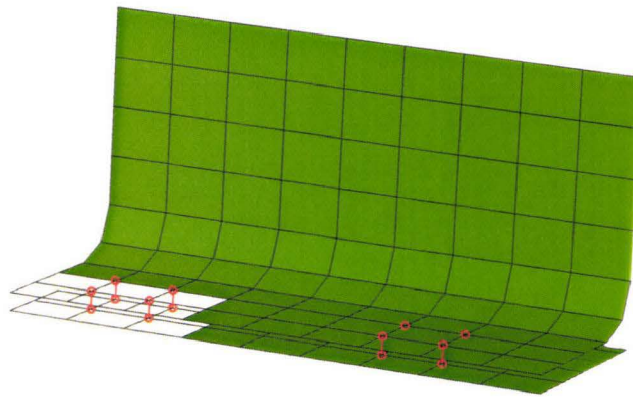


Figure 5.26: spotweld representation.

5.5.3 Correlation between numerical and experimental results

In terms of results, the dissipated energy is chosen observable. The difference between experimental and numerical responses are shown in Figure 5.27 for the only bonded specimens.

The main observation is that for both macro and mesoscopic models, the dissipated energy is overestimated at the beginning of the test. Regarding to the mesoscopic model which delivers a higher dissipated energy as the macroscopic one, the final value of this energy is higher and better placed in the experimental responses. In terms of deformed shapes, a good correlation is found between the two models and the experiments (Figure 5.28). In addition to this remark, the mesoscopic model predicts a better shape than the macroscopic one.

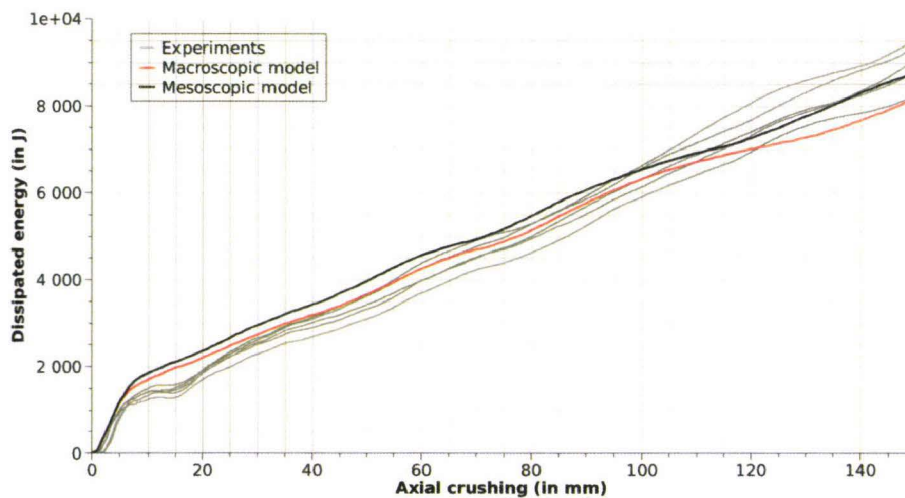


Figure 5.27: dissipated energy for both numerical models and experiments.

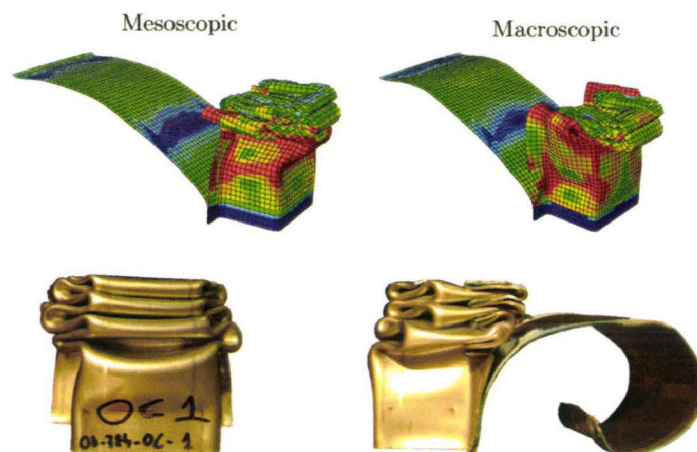


Figure 5.28: deformed shapes for both numerical models and experiments.

A study of the influence on the mesh refinement in the thickness is realized (Figure 5.29) for the typical one element through thickness and a 3 elements mesh. This influence is very limited and the quality of the response is slightly modified compare to the time computation which will be discussed later in this paragraph.

In addition, a study on the failure is also realized between the 1 and 3 elements through the thickness meshes. Although the failure facies on the only bonded crashboxes are dispersives (mixed between cohesive, superficial cohesive and adhesive), the mesoscopic model is able to reproduce this dispersion but the representation is limited to the use of classical finite elements methods.

A study is also achieved on the crack propagation between the 1 and 3 elements through the thickness meshes. The study of the crack propagation is limited to the formation of the first local bulking of the specimen. As shown in Figure 5.32, the difference in crack

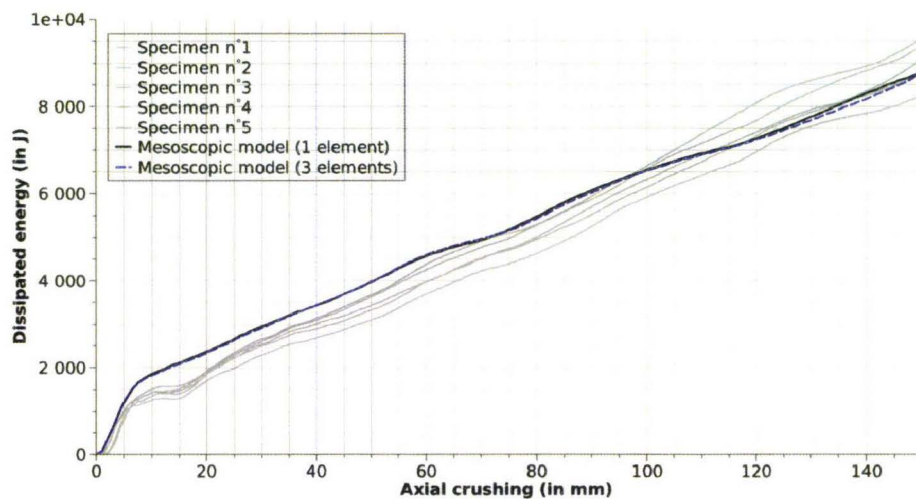


Figure 5.29: deformed shapes for both numerical models and experiments.

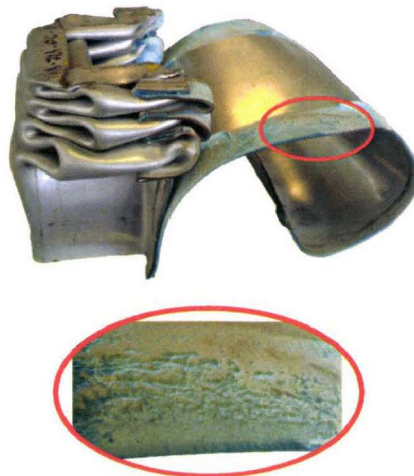


Figure 5.30: experimental failure facies of only bonded crashboxes.

propagation between the two meshes is limited by the size of the mesh. With a finer mesh, the crack is propagate on a larger surface than a coarser one.

As for the only bonded specimens, the numerical responses of the 5 spotwelds and bonding specimens show a good correlation with the experimental results (Figure 5.33). Here again the dissipated energy is overestimated at the beginning of the test but the difference between the meso and the macroscopic models is negligible for this case.

For the deformed shapes shown in Figure 5.34, another good correlation is observed between numerical and experimental shapes. It can be highlighted that the macroscopic model shows more instability in face of the mesoscopic one.

As for the previous geometries, a good correlation between the experimental and numerical dissipated energies is found for the 10 spotwelds and bonding specimens (Figure 5.35).

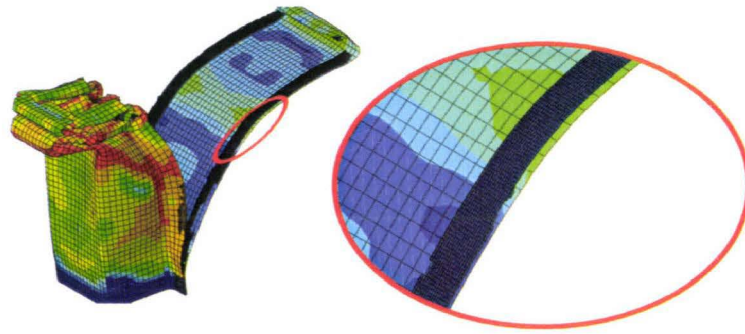


Figure 5.31: numerical failure faces of only bonded crashboxes.

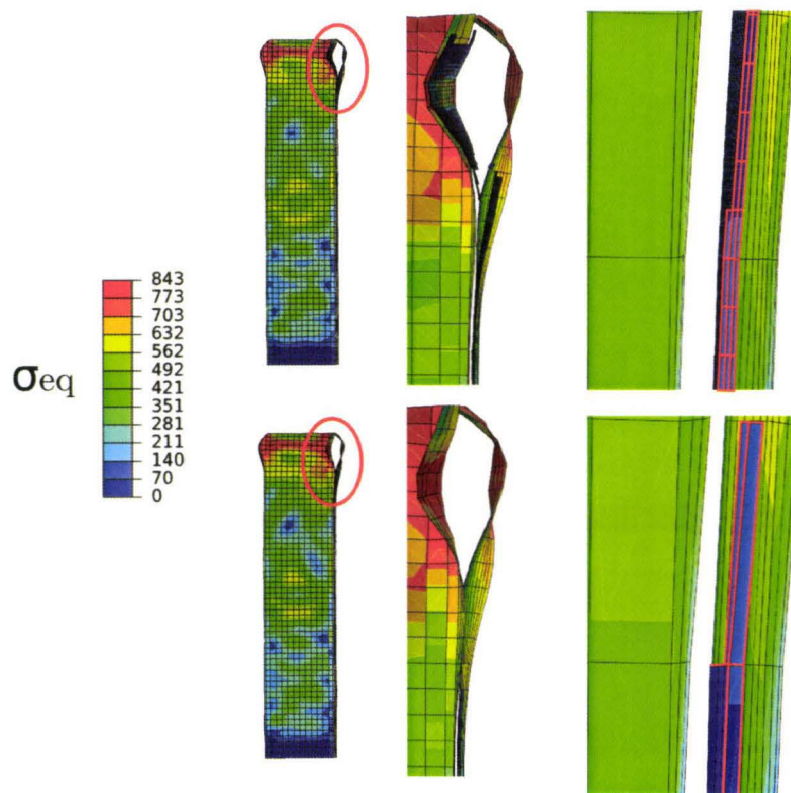


Figure 5.32: numerical crack propagation.

This energy is always overestimated at the beginning of the test but in a lower way for this time. Moreover the mesopic model provides a very good correlation until 100 mm of crushing than the macroscopic one is well fitted until 60 mm of crushing. For the deformed shapes a good correlation is always found (Figure 5.36) but the mesoscopic gives the best shape.

To conclude on these experiments and related simulations, a comparison between the numerical and the mean experimental dissipated energies is proposed in Figure 5.37. For all the crashbox configurations, the responses of the macro and the mesoscopic models

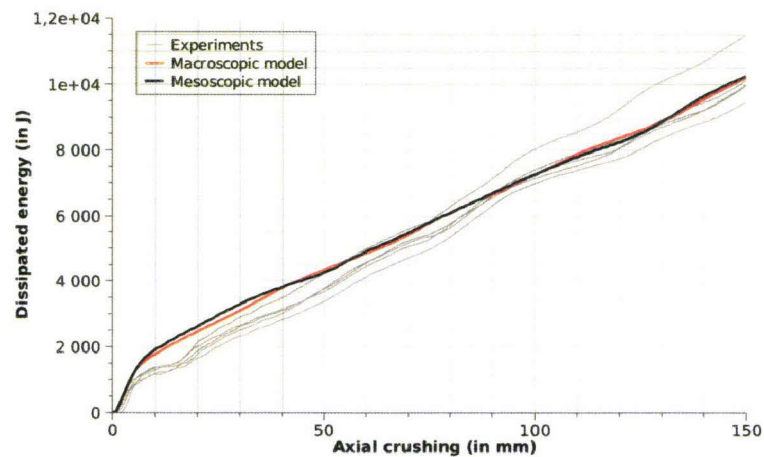


Figure 5.33: dissipated energy for both numerical models and experiments.

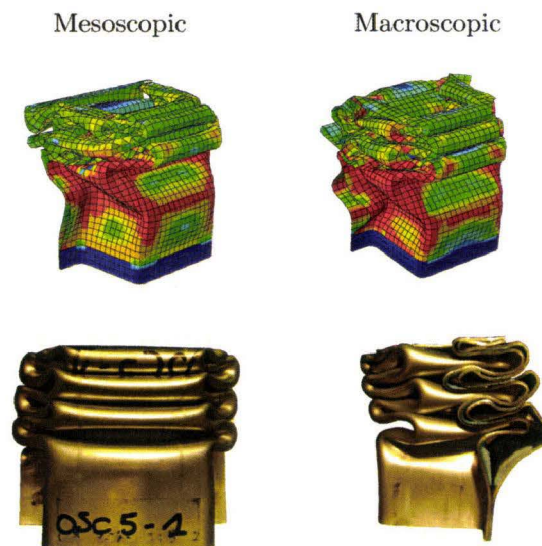


Figure 5.34: deformed shapes for both numerical models and experiments.

are always in the dispersion of the experiments. In addition, the mesoscopic response is always the nearest response of the mean experimental energy.

A summary of the computation times for the different crashbox configurations and finite element models used is proposed in Figure 5.38. It can be highlighted that the light difference between the macro and the mesoscopic models responses is directly paid by a high increase of the computation time (always greater than 1000 %). The impact of the mesh refinement on the computation is also described in Figure 5.39. The use of 3 elements inside the thickness of the bonded joints lead to a high increase of the computation (≈ 76 hours) for no visible effects on the response of the crashbox. It has to be noticed that the study with 5 elements into the thickness is not incorporated in the results due to the very high computation time (estimated to 60 days on 24 processors). All the previous

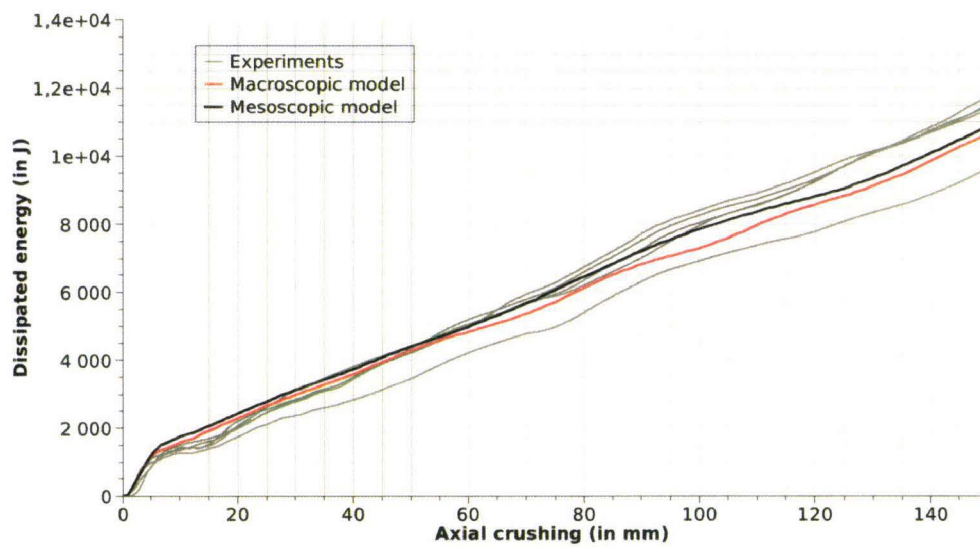


Figure 5.35: dissipated energy for both numerical models and experiments.

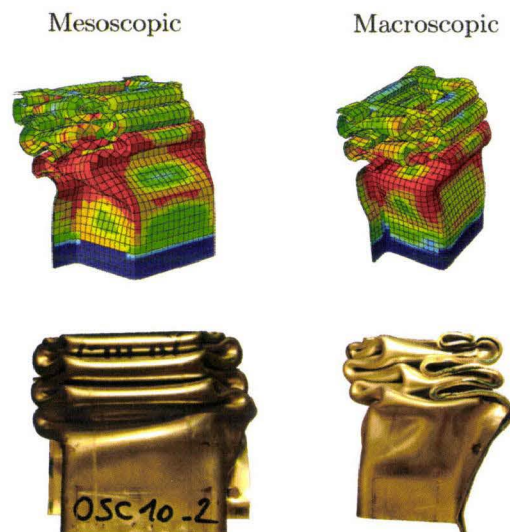


Figure 5.36: deformed shapes for both numerical models and experiments.

quantities have to be placed in face of the computation time of only spotwelded crashbox which is around 4 minutes. This last point proves that the macroscopic model lightly impacts the computation time and that adhesive can be taken into account in larger structures.

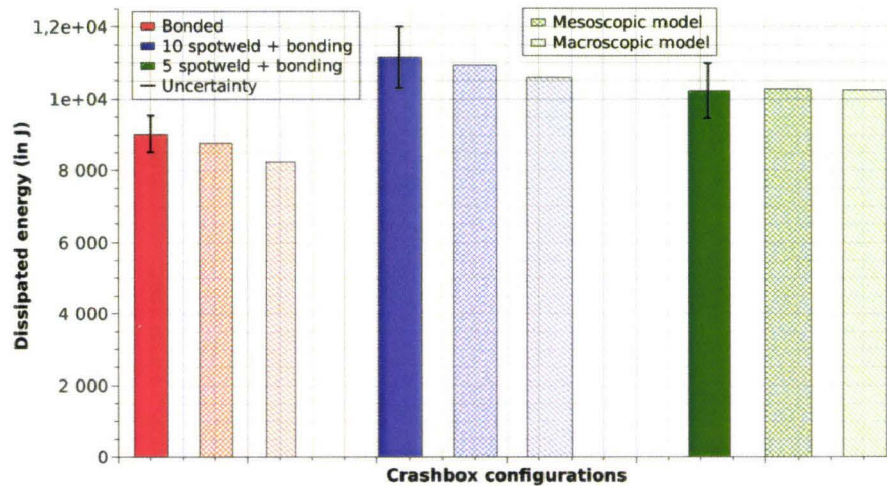


Figure 5.37: summary of the experimental and numerical dissipated energies for all the configurations.

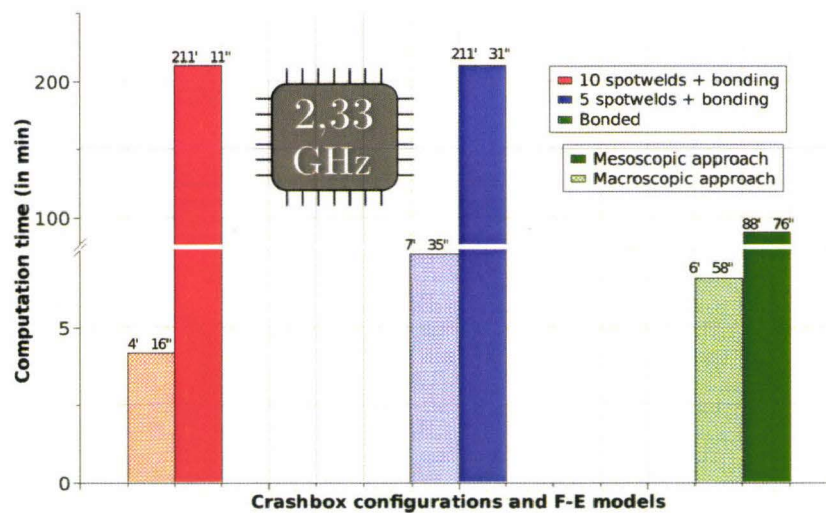


Figure 5.38: summary of the computation times.

5.6 Proposition of modeling strategy

With the previous correlations between the experimental and numerical responses but also their respective computation times, a detailed modeling strategy is proposed. From the previous paragraph three observations can be made:

- the accuracy is limited for the macroscopic model when the deformation is mainly control by the adhesive and not the adherent,
- no large differences are observed on global responses for large F-E models by using meso or macroscopic models,

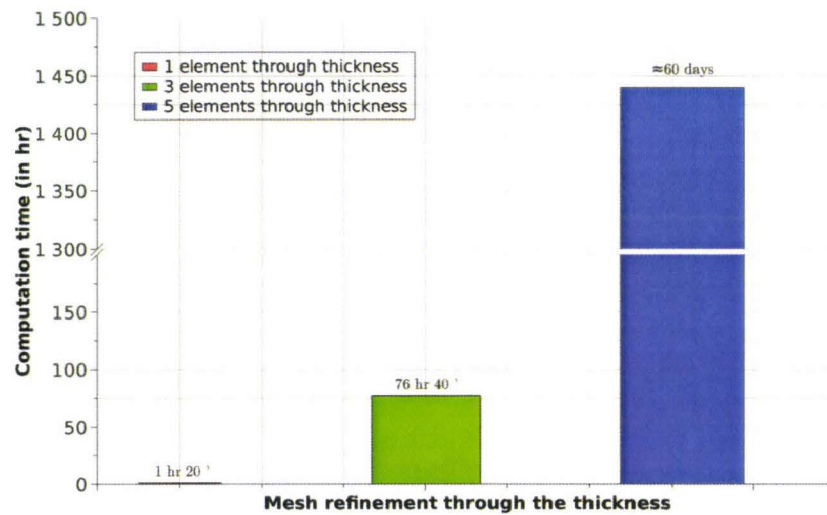


Figure 5.39: influence of mesh refinement on the computation times.

- the computation time is highly impacted in the case of mesoscopic model for large structures but stay as the same level as the macroscopic one for small structures.

Since no effect of adhesive modeling is shown with the macroscopic model on large F-E models computation times, it is now possible to take into account the bonded joints into a full car model.



Figure 5.40: frontal impact of a front car block.

Then in a complex model, the bonded joints can be modeled with the macroscopic model because the response in terms of global deceleration will be mainly led by the steel. In addition of these calculations, a detailed model can be used with the mesoscopic approach so as to study the local behaviour until failure of a reduced region. An sample of strategy is given for design of front car block (Figure 5.40) for a frontal impact at 56 km/h. For instance, the link between the cup shock and the crashbox (Figure 5.33) which is

traditionnally realized with a weld line and/or spotwelds could be a place for structural bonding.

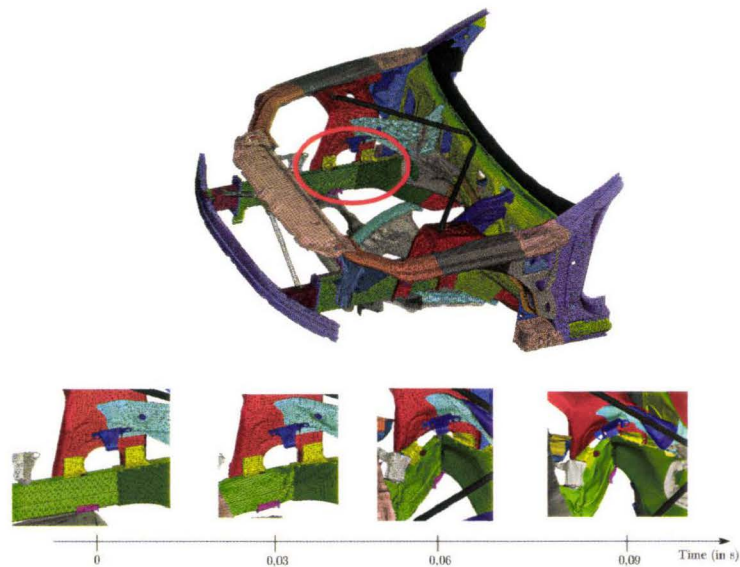


Figure 5.41: detailed view of the cup shock - crashbox link.

This local study can be easily performed with the mesoscopic model due to its light impact on the computation time of small F-E models. A first approach with only one element through the thickness of the bonded joints could be attractive but a better response could be obtained using 3 elements in the thickness.

Finally, this modeling strategy allows to model the bonded joints at different scales so as to limit the computation times for large structures and to use all the benefits of a fine prediction on small ones.

Conclusions & perspectives

Nowadays structural bonding is widely used in transportation industry. In the particular context of automotive industry, structural bonding is of high interest to reach the safe and lightweight goals of constructor. Even if the use of structural bonding is still increasing between new and old car models its use is always limited to luxurious ones. This limitations are mainly due to the misknowledge of the constitutive material of the joint and also the difficulty to modeled this joint whithout a huge increase of the computation time.

Concerning crashworthiness applications, these adhesives also named crash-stable adhesives, are based on a classical epoxy matrix toughened by addition of polymer nodules and theirs properties are then highly modified. These properties composed by a visco-elastic phase following by a visco-plasticity and damage behaviour are very similar to the behaviour of polymer materials. As for the polymers, a difference between the tensile and compressive behaviour is present and classical behaviour models can not be used to predict the local behaviour of adhesives. In terms of failure models, the crash-stable adhesives suffers of a lack detailed models in the literature and are generally described by simple criteria.

The second main limitation is linked to the computations time. Indeed the crashworthiness modelings are generally realized with an explicit integration scheme which requires very small time step for small elements. As the thicknesses of bonded joints are generally equal to 0.3 mm in automotive structures and the typical length of other elements is around 5 mm, the time step used for the algorithm is then highly reduced. Moreover the stress heterogeneities through the thickness can only be predict with a minimum of 3 elements and then the time step is therfore more reduced.

These thesis works are focused on the finite element modeling of bonded structures for crashworthiness. As a fine prediction of the behaviour and failure of bonded joints and non-time consuming model are not compatible, the final goal of these works is to provide a modeling strategy of bonded structures.

As a first stage, the behaviour and failure of the chosen crash-stable adhesive (BETA-MATE 1496VTM) is studied through experiments on bulk specimens. These kinds of tests are chosen to avoid classical problems of stress heterogeneties which are generally linked to assemblies tests. These tests are perfomed under a wide range of strain rates from 0.01 s^{-1} to 5000 s^{-1} and for different kinds of loadings. These loadings are composed by tensile, notched tensile, compression and shear tests. By realizing classical tensile tests and notched tensile tests, the effect of the triaxiality stress ratio on the damage evolution and also the failure is studied. With the compression tests, it is highlighted that the difference between compressive and tensile behaviour is not only limited to the yield stress but also extended to the behaviour law. The shear tests are used to check the isotropic behaviour of the considered adhesive and to quantify the failure phenomenon.

These experiments are analysed using different techniques including both contact and non-contact methods. The elasticity measurements are assumed by classical strain gages for both tensile and shear specimens and with an electro-optical extensometer for the compression tests. Both 2D and 3D digital image correlation techniques are used to investigate the plasticity and failure of the adhesive. For the determination of the tensile behaviour laws at constant strain rate, the $SE\dot{E}$ method is used. From all these measurements, mathematical models are identified to represent the physical properties of the adhesive.

The second step presented in these works is focused on the definition of the mesoscopic model. This model is implemented into the finite element software ABAQUS explicit through a VUMAT (Vectorized User MATerial) subroutine. A fine description of the adhesive properties is realized using the mesoscopic approach but a high impact on the time step is made. This model is able to reproduce all the behaviour and failure models identified in the previous part of the thesis. The non-isochoric behaviour of the adhesive is taken into account with a non-associative plastic flow. This non-associative plastic flow is limited to the tensile contribution of the behaviour due to the fact that no damage phenomena can occur in both compression and shear. A damage model also previously identified is used, this model is able to predict the dependency of the damage evolution on the triaxiality stress ratio. The failure model is based on an equivalent failure strain which evolves with the strain rate and the triaxiality stress ratio.

These previous works are followed by the macroscopic model development. The macroscopic approach allows to take into account the bonded joints without effect on the time step but the behaviour and failure of the adhesive are simplified. The macroscopic model is based on the spring element time step used for the classical interface and cohesive elements. Behaviour and failure computations are based on 3 independent springs representing the tension/compression and the 2 in plane-shear components. This approach is implemented in ABAQUS explicit through a VUEL (Vectorized User ELe ment) subroutine. This part of the thesis explains all the requirements which are involved to develop a macroscopic element. These steps are described from the mass matrix computation to the nodal forces update through the local basis, opening and sliding displacements, strains and stresses computations. The identification of the macroscopic behaviour are realized on the same experimental database than the mesoscopic model but with a simplified analysis. The failure properties are then extracted from special purpose tests. These tests based on tensile and shear loadings are achieved with double U and double shear lap joints specimens respectively. The analysis of the opening and sliding displacement which lead to failure, is realized with digital image correlation technique. Finally, the modeling strategy is proposed based on the analysis of different validation tests. Two different load complexity tests are chosen to correlate the numerical responses. For the dynamic flexure tests, it is highlighted that only the mesoscopic model delivers a good description of the force response during all the test. It also appears that the computation time between the macro and the mesoscopic models differs from a few seconds only. The influence of the mesh sensitivity through the thickness is also realized with this load case. The quality of the response is then improved with the thickness mesh refinement as expected. The simulations of dynamic axial crushing tests have shown a good correlation with the experiments for the both approaches. This fact is due to the

global response of the crashbox which is mainly dominated by the steel sheets. Even if the quality of the response is lightly affected by the model used for the adhesive the computation is well impacted. As an example the 10 spotwelds crashbox shows a time computation of 4 minutes for the only spotwelded configuration, 4 minutes and 16 seconds for spotwelded/bonding configuration with the macroscopic approach and more than 1 hour for the mesoscopic approach. From the quality of these numerical/experimental correlations and their computation times, a modeling strategy is then proposed and an example is given on the frontal impact of a front car block. This strategy postulates that the bonded joints can be included inside a huge model without influencing the computation time but local study of connector behaviour and failure can be realized with a fine mesoscopic approach.

Although the proposed models of this thesis show a good correlation with experimental data, many improvements can be brought to these models. These improvements are focused on the discarded points of these works. In terms of experimental characterization of the bulk adhesive, the elastic tensile properties as well as the plastic and failure ones should be investigated at higher strain rates with a different setup of Hopkinson bars. In addition, the shear properties have to be investigated under a wide range of strain rates, for that the Iosipescu test used in this thesis is not suitable and other tests are required. A new specimen is designed for polymeric materials (Figure 6.1), this specimen allows the characterization of the shear behaviour failure from quasi-static to intermediate strain rates (around 100 s^{-1}).

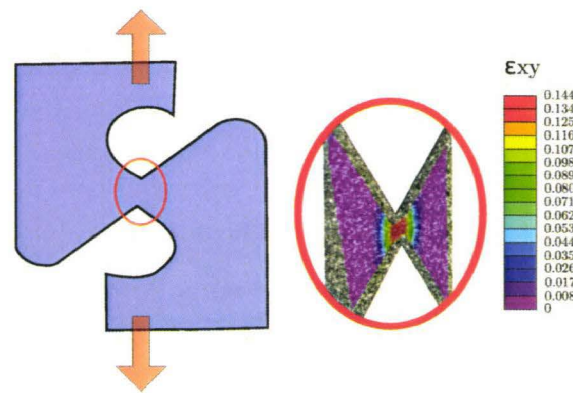


Figure 6.1: illustration of new shear specimens for polymeric materials.

The damage model used in this thesis needs to be improved by adding a void evolution law. This law is experimentally identified by achieving in-situ tensile in a micro-tomograph. With this device X-ray picture of the instantaneous resistant plane of a reduced specimen can be obtained and the voids are directly located.

Another way could lead to the study of thermal effects on the behaviour and failure of adhesive. Indeed during high strain rate loading and especially in crashworthiness events, the temperature can rapidly increase. So the study of the self heating of the adhesive and its behaviour and failure under high temperatures have to be investigated to take a step forward. In terms of failure criterion, the experimental database of this thesis

should be extended in terms triaxiality stress ratios so as to allow the development of a better mathematical model. This extension could be realized by achieving tests on Arcan specimens but also tensile specimens with different notch radius and some biaxial tensile specimens (Figure 6.2).

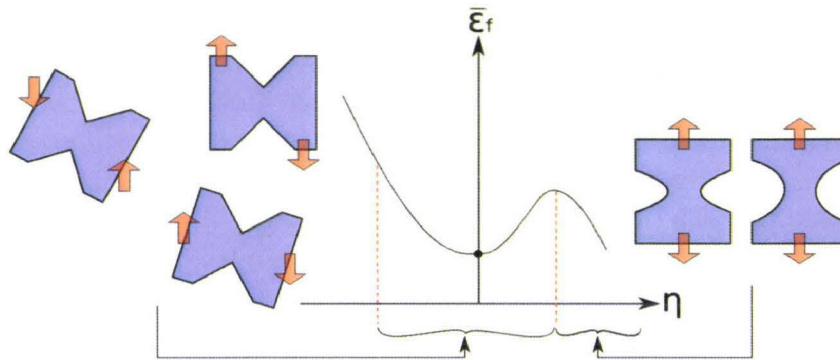


Figure 6.2: illustration of possible extensions of failure criterion.

Many improvements can also be made on the macroscopic finite element. Instead of three independent springs an equivalent formulation could be interesting. This equivalent formulation will allow to use a real yield surface in which a hydrostatic pressure dependency can be described. The plasticity computation of this element can also be improved by an iterative formulation with a non-associative approach. Here again the damage model could also be improved using the same or a simplified version of the mesoscopic damage model. The failure properties identification of this element is also a point of improvement. Although the strain rate sensitivity seems to be negligible in bonded assemblies due to the triaxiality stress ratio, high strain rate testing on Hopkinson bars could give interesting informations. For that new specimens and Hopkinson bars are designed (Figure 6.3) so as to achieve tensile, shear and mixed loadings on bonded joints.

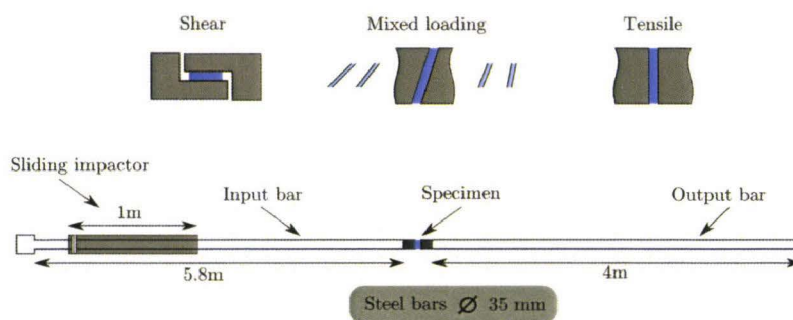


Figure 6.3: new specimens and Hopkinson bars device for the high strain rate testing of bonded joints.

To conclude these perspectives, a last model could be develop so as to realize a fine prediction of the behaviour and failure of the adhesive with a small impact on the time computation. This model could be based on a macro element in which a sub calculation with a fine mesh and the mesoscopic model (Figure 6.4) will be used.

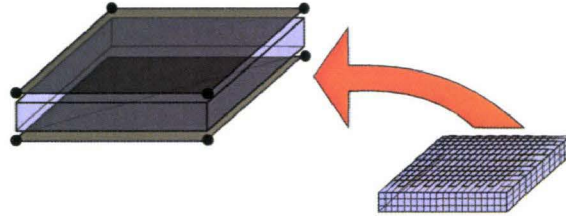


Figure 6.4: new macro element.

Bibliography

- [1] N.G. Berry et al. The influence of circular centered defects on the performance of carbon-epoxy single lap joints. *Polymer testing*, 21:373–379, 2002. 5, 10
 - [2] A. Deb et al. An experimental and analytical study of the mechanical behaviour of adhesively bonded joints for variable extension rates and temperatures. *International journal of adhesion and adhesives*, 23:1–15, 2007. 5, 10
 - [3] M. You et al. A numerical and experimental study of gap length on adhesively bonded aluminum double-lap joint. *International journal of adhesion and adhesives*, 27:696–702, 2007. 5, 10, 52
 - [4] G. Dean et al. Prediction of deformation and failure of rubber-toughened adhesive joints. *International journal of adhesion and adhesives*, 24:295–306, 2004. 5, 10
 - [5] G. N. Finogenov. Creep assessment procedure for adhesive joints. *Polymer science*, 49(1):106–107, 2007. 5, 10
 - [6] G. Dean et al. Prediction of deformation and failure of rubber-toughened adhesive joints. *International Journal of Adhesion and Adhesives*, 24:295–306, 2004. 5, 12, 53, 54, 55
 - [7] A.B. de Morais. Strength of epoxy adhesive-bonded stainless-steel joints. *International journal of adhesion and adhesives*, 27:679–686, 2007. 10, 52
 - [8] A. Derewonko and others. Strength assessment of adhesive-bonded joints. *Computational materials science*, 43:157–164, 2008. 10
 - [9] J. COGNARD et al. Influence of water on the cleavage of adhesive joints. *International journal of adhesion and adhesives*, 8:93–99, 1988. 10
 - [10] Fan-Rong Kong et al. Three-dimensional stress analysis of adhesive-bonded joints under cleavage loading. *International journal of adhesion and adhesives*, 27:298–305, 2007. 10
 - [11] M. Horgnies et al. Relationship between the fracture energy and the mechanical behaviour of pressure-sensitive adhesives. *International journal of adhesion and adhesives*, 27:661–668, 2007. 10
 - [12] H. Hadavinia et al. A numerical analysis of the elastic-plastic peel test. *Engineering Fracture Mechanics*, 73:2324–2335, 2006. 10
 - [13] L. Goglio et al. Impact rupture of structural adhesive joints under different stress combinations. *International Journal of Impact Engineering*, 35:635–643, 2008. 10
 - [14] G. Challita. *Development of a shear test on bonded assemblies at high and medium rates*. PhD thesis, Ecole Centrale de Nantes, 2009. 10
-

- [15] J.Y. Cognard et al. A study of the non-linear behaviour of adhesively-bonded composite assemblies. *Composite Structures*, 76:34–46, 2006. 11
- [16] J.Y. Cognard et al. Development of an improved adhesive test method for composite assembly design. *Composite Science and Technology*, 65:359–368, 2005. 11
- [17] M. Arcan et al. A method to produce uniform plane-stress states with applications to fiber-reinforced materials. *Experimental Mechanics*, 35:141–146, 1978. 11
- [18] L. Goglio et al. High strain-rate compressive and tension behaviour of an epoxy bi-component adhesive. *International journal of adhesion and adhesives*, 28:329–339, 2008. 11
- [19] F. Hild. Correli^{LMT}: A software for displacement field measurements by digital image correlation. *LMT Cachan internal report No 254*, 2002 2002. 11
- [20] J.-N. Périé et al. Analysis of a multiaxial test on a c/c composite by using digital image correlation and a damage model. *Experimental Mechanics*, 42, 2002. 11
- [21] A.S. Khan et al. Thermo-mechanical large deformation response and constitutive modeling of viscoelastic polymers over a wide range of strain rates and temperatures. *International Journal of Plasticity*, 22:581–601, 2006. 11
- [22] D. Lai. A non-linear viscoelastic model developed for semi-crystalline polymer deformed at small strains with loading and unloading paths. *Materials Science and Engineering A*, 405:266–271, 2005. 11
- [23] S. Denga. Temperature-dependent elastic moduli of epoxies measured by dma and their correlations to mechanical testing data. *Polymer testing*, 26:803–813, 2007. 11
- [24] F. Lapique. Curing effects on viscosity and mechanical properties of a commercial epoxy resin adhesive. *International Journal of Adhesion and Adhesives*, 22:337–346, 2002. 11
- [25] J. Richeton et al. A unified model for stiffness modulus of amorphous polymers across transition temperatures and strain rates. *Polymer*, 46:8194–8201, 2005. 11, 13, 39
- [26] I. Malvade et al. Numerical prediction of load-displacement behaviors of adhesively bonded joints at different extension rates and temperatures. *Computational Materials Science*, 44:1208–1217, 2009. 11, 52
- [27] C. G'Sell et al. Effect of stress triaxiality on neck propagation during the tensile stretching of solid polymers. *Journal of Materials Science*, 18:1731–1742, 1983. 11
- [28] C. G'Sell et al. Effect of stress triaxiality on neck propagation during the tensile stretching of solid polymers. *Journal of Materials Science*, 18:1731–1742, 1983. 11
- [29] Y. Tillier. *Identification par analyse inverse du comportement mécanique des polymères solides ; application aux sollicitations multiaxiales et rapides*. PhD thesis, Ecole nationale supérieure des mines de Paris, 1998. 12

- [30] A. F. Epee. *Caractérisation et modélisation du comportement d'un polymère semi-cristallin au crash*. PhD thesis, Université de Valenciennes et du Hainaut-Cambrésis, 2009. 12, 13
- [31] F. Lauro. *Méthodologie pour la prise en compte de l'endommagement microstructural sous chargement dynamique*. PhD thesis, Université de Valenciennes et du Hainaut-Cambrésis, 1996. 12
- [32] G. R. Johnson et al. Fracture characteristics of three metals subjected to various strains, strain rates, temperatures and pressures. *Engineering fracture mechanics*, 21:31–48, 1985. 12, 13
- [33] T. Wierzbicki et al. On the effect of the third invariant of the stress deviator on ductile fracture. *Impact and Crashworthiness Lab Report*, 136, 2005. 12, 13
- [34] L. da Silva et al. Manufacture of adhesive joints and bulk specimens with high-temperature adhesives. *International journal of adhesion and adhesives*, 24:69–83, 2004. 13, 14
- [35] R. Mengel et al. Mechanical properties of hub/shaft joints adhesively bonded and cured under hydrostatic pressure. *International journal of adhesion and adhesives*, 27:568–573, 2007. 13
- [36] J. Chen et al. Temperature-dependent phase behavior in poly(ϵ -caprolactone)-epoxy blends. *Polymer*, 42:2193–2199, 2001. 13
- [37] F. Lauro et al. The $se\dot{E}$ method for determination of behaviour laws for strain rate dependent material: Application to polymer material. *International journal of impact engineering*, 37:715–722, 2010. 21
- [38] G. R. Johnson et al. A constitutive model and data for metals subjected to large strains, high strain rates and high temperatures. In *7th Symposium Ballistic*, pages 541–547, 1983. 41
- [39] G.R. Cowper et al. Strain hardening and strain rate effect in the impact loading of cantilever beams. *Brown University Division of Applied Mathematics report*, 28, 1957. 41
- [40] Abaqus documentation. 6.9. 53, 54
- [41] P.A. Du Bois et al. The influence of permanent volumetric deformation on the reduction of the load bearing capability of plastic components. In *10th International LS-DYNA Users Conference*, Material modeling, 2008. 54
- [42] E. A. de Souza Neto et al. *Computational methods for plasticity, theory and applications*. WILEY, 2008. 56, 63, 64
- [43] Pamcrash documentation. 2009. 58
- [44] J.C.Simo et al. *Computational inelasticity*. SPRINGER, 1998. 64

-
- [45] C.W. Hirt. Heuristic stability theory for finite-difference equations. *Journal of computational physics*, 2:339–355, 1968. 72
- [46] T. Carlberger et al. An explicit fe-model of impact fracture in an adhesive joint. *Engineering Fracture Mechanics*, 74:2247–2262, 2007. 73
- [47] V. Tvergaard et al. Effect of anisotropic plasticity on mixed mode interface crack growth. *Engineering Fracture Mechanics*, 74:2603–2614, 2007. 73
- [48] D. Xie et al. Discrete cohesive zone model for mixed-mode fracture using finite element analysis. *Engineering Fracture Mechanics*, 73:1783–1796, 2006. 74
- [49] D. Xie et al. Discrete cohesive zone model to simulate static fracture in 2d triaxially braided carbon fiber composites. *Journal of Composite Materials*, 40:2025–2046, 2006. 74
- [50] S. Li et al. Use of a cohesive-zone model to analyze the fracture of a fiber-reinforced polymer-matrix composite. *Composites science and technology*, 65:537–549, 2005. 74
- [51] M. Kafkalidis et al. The effects of geometry and material properties on the fracture of single lap-shear joints. *International Journal of Solids and Structures*, 39:4367–4383, 2002. 74
- [52] Y. F. Gao et al. A simple technique for avoiding convergence problems in finite element simulations of crack nucleation and growth on cohesive interfaces. *Modeling and Simulation in materials science and engineering*, 12:453–463, 2004. 74
- [53] G. Camacho et al. Computational modelling of impact damage in brittle materials. *International Journal of Solids and Structures*, 33:2899–2938, 1999. 75
- [54] V. Tvergaard et al. The relation between crack growth resistance and fracture process parameters in elasticplastic solids. *Journal of the Mechanics and Physics of Solids*, 40:1377–1397, 1992. 75
- [55] O.C. Zienkiewicz et al. *The Finite Element Method, volume 1 the basis*. Butterworth-Heinemann, 2000. 78

List of Figures

1.1	evolution of structural bonding use in some car models	1
1.2	crashbox configurations a) 10 spotwelds, b) 10 spotweld + bonding and c) 5 spotwelds + bonding and thicknesses for the corresponding steel grade.	2
1.3	evolution of dissipated energy in function of the crashbox configuration.	3
1.4	possible places of structural bonding in transportation structures (yellow lines).	4
1.5	formulation of DGEBA epoxyde used in crash-stable adhesives.	4
1.6	a) polymer nodules and b) mineral compounds.	4
1.7	illustration of element sizes.	5
1.8	representation of the proposed modeling strategy.	7
2.1	Classical bonded joints geometries.	10
2.2	description of a) aluminum mould and b) heating press.	13
2.3	difference on strain fields between a) a pore and b) a pore-free specimen.	14
2.4	distribution of true longitudinal strain at failure on a pore and pore-free specimen.	14
2.5	a) localization of pores by lighting technique on a plate and b) μ CT scan of adhesive plate.	15
2.6	high speed hydraulic a) tensile and b) compressive configurations.	16
2.7	a) pre-stressed tensile and b) visco-elastic compressive Hopkinson bars.	16
2.8	Iosipescu shear test device.	16
2.9	normalized geometry of specimen for low strain rate range (thickness 4mm).	17
2.10	modified samples based on normalized geometry used for highspeed hydraulic machine (thickness 4mm).	17
2.11	a) specimen geometry for the Hopkinson tensile testing (thickness 4mm) and b) F.E. results in terms of equivalent plastic strain.	17
2.12	notched specimen used for low strain rate range (thickness 4mm).	18
2.13	notched specimen used for highspeed hydraulic machine (thickness 4mm).	18
2.14	normalized geometry of the compressive specimen.	18
2.15	normalized geometry of the Iosipescu shear specimen.	19
2.16	strain gages on Iosipescu specimen.	19
2.17	configuration of a) electro-optical extensometer and b) 3D DIC.	20
2.18	difference between noisy and smoothed data.	21
2.19	description of a) heterogeneous strain fields and b) behaviour surface.	22
2.20	description of a) Numerical cut of surface and b) true behaviour law at constant strain rate.	22
2.21	failure detection technique for compressive tests.	23
2.22	failure detection technique used for tensile, notched tensile and shear tests.	24
2.23	computed uncertainty for the various frame acquisition rate.	24
2.24	a) true longitudinal strain field with a $8\mu\text{m}$ strain length calculation and b) true longitudinal strain field with a $300\mu\text{m}$ strain length calculation.	25

2.25	shear strain contour plot for a Iosipescu shear specimen.	26
2.26	evolution of the tensile elastic modulus in function of the strain rate. . . .	26
2.27	repartition of longitudinal strain along the height of the strain gage specimen and the free one.	27
2.28	influence of strain gage on the true longitudinal strain in center of specimens.	27
2.29	evolution of compressive elasticity modulus in function of strain rate and curing pressure.	28
2.30	computed elasticity shear chord modulus.	28
2.31	influence of strain gage on the true shear strain.	29
2.32	synthesis on the elastic moduli measurements.	29
2.33	transversal strain on the cross section of the tensile specimen.	30
2.34	true stress / true plastic strain curves obtained with $SE\dot{E}$ method.	30
2.35	true stress versus true plastic strain for 4 MPa curing pressure specimen. .	31
2.36	true stress versus true plastic strain for 1 MPa curing pressure specimen. .	31
2.37	influence of curing pressure on the stress level of toughened epoxy (53 s^{-1}).	32
2.38	a) initial shape and b) deformed shape with a true strain of 0.5.	32
2.39	principal directions of diagonalized strain tensor.	33
2.40	evolution of local principal strains during an shear test.	34
2.41	shear behaviour law and confidence interval.	34
2.42	evolution of plastic Poisson's ratio.	35
2.43	comparison between tensile, compressive and shear yield stresses.	36
2.44	comparison between tensile and compressive plasticity behaviour.	36
2.45	evolution of equivalent failure strain of tensile specimens in function of the equivalent strain rate.	37
2.46	evolution of equivalent failure strain of notched tensile specimens in function of the equivalent strain rate.	38
2.47	true equivalent failure strain on Iosipescu shear tests.	38
2.48	evolution of equivalent failure strain of compressive specimens in function of the equivalent strain rate.	39
2.49	evolution of elasticity modulus in function of true strain rate.	40
2.50	identification of tensile behaviour law.	41
2.51	identification of shear behaviour law.	42
2.52	identification of compressive behaviour law.	42
2.53	evolution of damage for two different triaxiality stress ratio.	43
2.54	identification of d_0 damage evolution law parameter.	43
2.55	identification of K_d damage evolution law parameter.	44
2.56	identification of w_d damage evolution law parameter.	44
2.57	identification strategy for the failure criterion.	45
2.58	identification of the a_f function formulation.	46
2.59	identification of the b_f function formulation.	46
2.60	3D representation of the new failure criterion.	47
2.61	study of the failure criterion at constant strain rate on a wide range of triaxiality stress ratios.	47
2.62	study of the failure criterion at constant triaxiality stress ratio on a wide range of strain rates.	48

2.63	failure criterion saturation in term of triaxiality stress ratio.	48
2.64	failure criterion saturation in term of strain rates.	49
2.65	summary of mesoscopic model parameters.	50
3.1	example of necking in a steel single lap joint test.	52
3.2	example of necking in a steel single lap joint test.	52
3.3	different failure modes in a bonded joint.	53
3.4	evaluation of classical yield criterion.	54
3.5	difference between exponent Drucker Prager and SAMP model.	55
3.6	illustration of tabulated visco-plastic behaviour law.	55
3.7	a) general overview of the algorithm and b) description of elasticity algorithm	57
3.8	yield criterion algorithm.	59
3.9	illustration of the double Drucker Prager yield criterion.	60
3.10	illustration of the difference between a non-associative and associative plas-	
	ticity in the von Mises case.	61
3.11	3D representation of the plastic potential.	62
3.12	schematic representation of the apex derivation problem.	62
3.13	a) selection of the appropriate return vector and b) resulting return vectors.	63
3.14	return vectors for the tensile, shear and compressive cases.	64
3.15	illustration of closed point method.	64
3.16	Newton Raphson algorithm schema.	65
3.17	illustration of numerical derivation of tensile plastic behaviour law.	66
3.18	illustration of damage update technique.	67
3.19	algorithm of the implemented behaviour model.	68
4.1	typical crashbox configuration.	72
4.2	representation of spring element.	72
4.3	a) representation of stress tensor in an interface element and b) justification	
	of interface elements.	73
4.4	difference between discrete and continuum cohesive zone models.	74
4.5	illustration of the principle of a traction-separation law.	74
4.6	traction-separation laws for a) brittle, b) ductile materials and c) equivalent	
	formulation.	75
4.7	cohesive elements properties identification.	76
4.8	new cohesive element properties.	76
4.9	crack propagation through an element.	76
4.10	flowchart for the implementation of the cohesive element.	77
4.11	illustration of local basis.	78
4.12	example of relative displacements computations for U and V	79
4.13	illustration of initial element dimensions.	80
4.14	illustration of nodal forces update.	82
4.15	failure initiation criteria in the a) tension/shear and b) compression/shear.	83
4.16	illustration of effect of crack propagation through an element.	83
4.17	illustration of crack propagation through an element.	84
4.18	equivalent loading speed.	84

4.19	boundaries conditions and loading speed applied on tension numerical test.	85
4.20	reaction force a) until crack propagation through the element and b) after the failure of the element.	85
4.21	numerical study of the ratio h	86
4.22	schematic representation of boundaries tests a) in face and b) in normal plane of the bonded joint.	87
4.23	example of LEFM crack propagation a) DCB like simulation and b) evolution of stresses.	87
4.24	macroscopic approach properties identification guidelines.	88
4.25	identification of yield stress in macroscopic approach.	89
4.26	identified yield stresses and models for a) tension and b) compression.	89
4.27	identification of tangent moduli in macroscopic approach.	89
4.28	geometry of the double U specimens.	90
4.29	geometry of the double lap joints specimens a) in static and b) in dynamic.	91
4.30	presentation of the special equipment needed for the tensile tests.	92
4.31	illustration of the length used for the strain rate calculation.	92
4.32	illustration of measurement protocol for a) tensile tests and b) shear tests.	93
4.33	illustration of initiation displacements computation.	93
4.34	results in terms of opening and sliding displacements for the different strain rates.	94
4.35	a) cutted view through the thickness of the bonded joint in tension and b) evolution of the triaxiality stress ratio in function of the time.	95
4.36	a) cutted view through the thickness of the bonded joint in shear and b) evolution of the triaxiality stress ratio in function of the time.	96
4.37	identification of the failure initiation criterion.	97
4.38	crack tip displacement identification.	97
4.39	illustration of the crack tip displacement measurement.	98
4.40	idealization of the crack tip.	98
4.41	results in term of crack tip displacements.	99
4.42	crack propagation speed identification.	99
4.43	crack propagation speed in function of the normative variable.	100
4.44	summary of macroscopic model parameters.	101
5.1	description of experiments and load complexity.	104
5.2	numerical link between steel and adhesive.	106
5.3	true behaviour laws for the DP 600 steel.	106
5.4	effect of step size on the failure strain computation in D.I.C.	107
5.5	evolution of the a_f function in function of the mesh size.	107
5.6	presentation of the Hopkinson bars.	108
5.7	FE model of the double U test.	109
5.8	identification of the speed ramp.	109
5.9	experimental and numerical force displacement curves.	110
5.10	discontinuities problem between specimen and Hopkinson bars.	110
5.11	experimental and numerical curves for force displacement.	111
5.12	presentation of the ballistic device.	112

5.13	geometries of the specimen.	112
5.14	dynamic flexure simulation setup.	113
5.15	experimental forces measured on the tube.	113
5.16	filtering of the displacement of the impactor.	114
5.17	comparison between macro and mesoscopic models on the force-time curve of the typical sample.	114
5.18	effect of the mesh refinement through thickness.	115
5.19	numerical crack initiation on the dynamic flexure test.	115
5.20	experimental crack initiation on the dynamic flexure test.	116
5.21	summary of the computation times for the different models.	116
5.22	presentation of the dynamic axial crushing test.	117
5.23	discontinuous bond line.	118
5.24	spotweld machine and places for spotweld.	118
5.25	dynamic axial crushing simulation setup.	119
5.26	spotweld representation.	119
5.27	dissipated energy for both numerical models and experiments.	120
5.28	deformed shapes for both numerical models and experiments.	120
5.29	deformed shapes for both numerical models and experiments.	121
5.30	experimental failure facies of only bonded crashboxes.	121
5.31	numerical failure facies of only bonded crashboxes.	122
5.32	numerical crack propagation.	122
5.33	dissipated energy for both numerical models and experiments.	123
5.34	deformed shapes for both numerical models and experiments.	123
5.35	dissipated energy for both numerical models and experiments.	124
5.36	deformed shapes for both numerical models and experiments.	124
5.37	summary of the experimental and numerical dissipated energies for all the configurations.	125
5.38	summary of the computation times.	125
5.39	influence of mesh refinement on the computation times.	126
5.40	frontal impact of a front car block.	126
5.41	detailed view of the cup shock - crashbox link.	127
6.1	illustration of new shear specimens for polymeric materials.	131
6.2	illustration of possible extensions of failure criterion.	132
6.3	new specimens and Hopkinson bars device for the high strain rate testing of bonded joints.	132
6.4	new macro element.	133

List of Tables

1.1	increase of acoustic between the old and new Audi A6	2
1.2	illustration of time step problem between steel shell and adhesive volume.	6
1.3	summarize of the different models.	6
4.1	adhesive element properties and related time steps.	73
4.2	summarize of the elastic properties of the macroscopic approach.	88
4.3	Loading rate and corresponding strain rate.	92
5.1	summarize of the shell element sizes.	105
5.2	summarize of the adhesive element sizes.	105



**Experiments and models until failure of bonded joints for
crashworthiness**

Abstract:

Keywords: Crashworthiness, adhesive, finite element, cohesive element, digital image correlation, high strain rate.

Bibliothèque Universitaire de Valenciennes



00900746